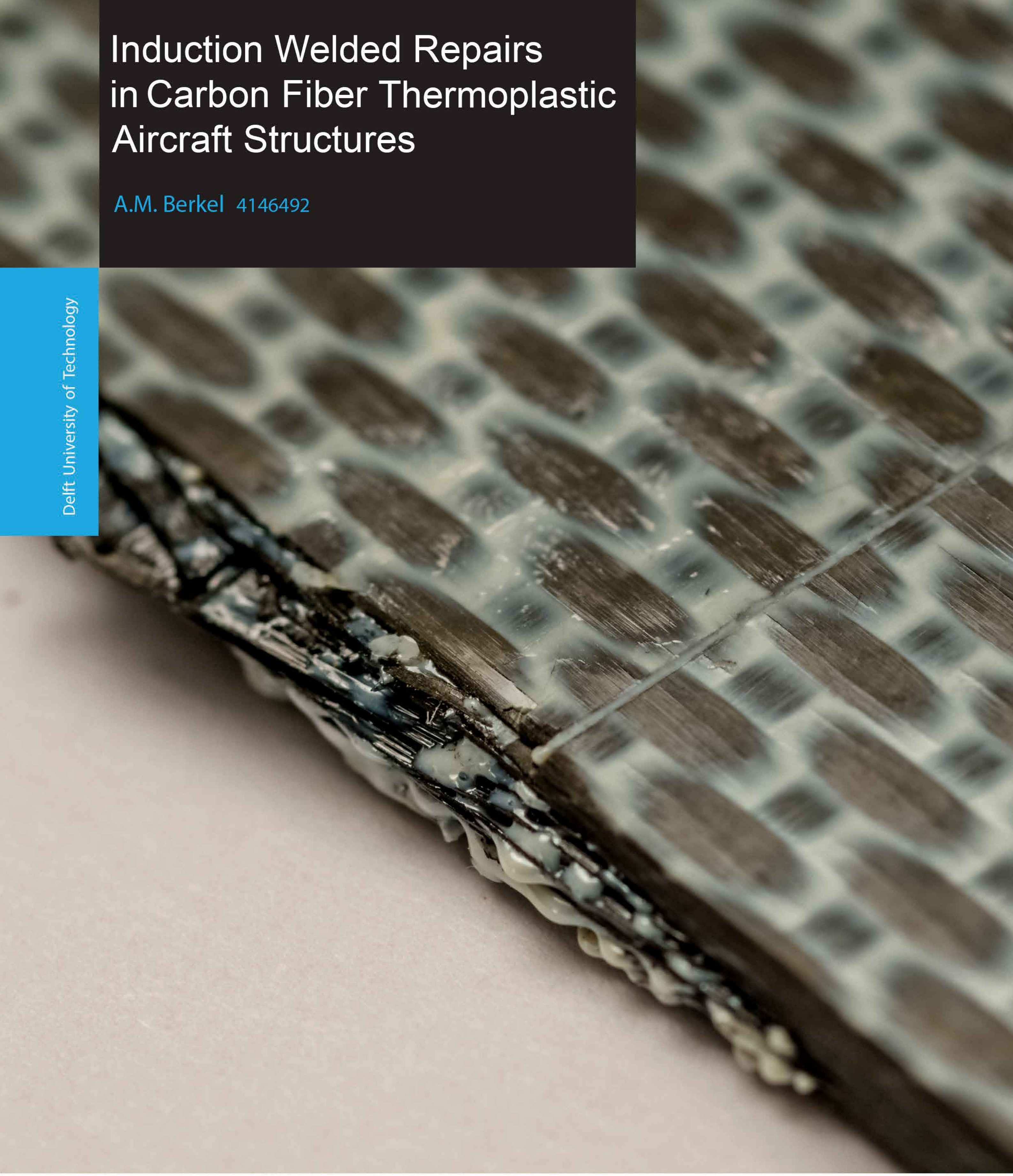

# Induction Welded Repairs in Carbon Fiber Thermoplastic Aircraft Structures

A.M. Berkel 4146492

Delft University of Technology

Challenge the future

# Induction Welded Repairs in Carbon Fiber Thermoplastic Aircraft Structures

by

## A.M. Berkel

to obtain the degree of Master of Science
at the Delft University of Technology,
to be defended publicly on Monday 23rd April at 09:45.

| | | |
|---|---|---|
| Student number: | 4146492 | |
| Project duration: | March 29, 2017 – April 23, 2018 | |
| Exam committee: | Dr. ir. R.C. Alderliesten, | TU Delft, chair |
| | Dr. I. Fernandez-Villegas, | TU Delft, supervisor |
| | Dr. C. Kassapoglou, | TU Delft, supervisor |
| | Ir. M. Labordus, | KVE Composites, supervisor |
| | Dr. J.C. Bijleveld | TU Delft |

*This thesis is confidential and cannot be made public until April 23, 2023*

# Preface

This master's thesis is the conclusion of the graduate program Aerospace Structures and Materials at the Delft University of Technology. This project is performed both at Delft University of Technology and KVE Composites in The Hague.

I would like to thank my supervisors at the TU Delft, Dr. Christos Kassapoglou and Dr. Irene Fernandez-Villegas, and my supervisor at KVE Composites, Ir. Maarten Labordus, for guiding me during the thesis. I would also like to extend my gratitude to Tom Jansen and Bas Kuenen, who were always up for a discussion about my project or asking critical questions, and my other colleagues at KVE Composites who made my time at KVE enjoyable.

I also appreciate the effort and time Barend van der Meulen put into the making of the cover photo and my girlfriend and mother put into improving the readability of this thesis.

Last but not least I would like to thank my parents and sister for not only supporting me throughout my studies, but also motivating me to follow my passion, even though this could not always be combined with my study.

*A.M. Berkel*
*Delft, April 2018*

# Contents

# List of Figures

# List of Tables

# List of Symbols

| | | |
|---|---|---|
| $d$ | Distance from surface | $[m]$ |
| $E$ | Laminate stiffness | $[GPa]$ |
| $E_0$ | 0° Ply stiffness | $[GPa]$ |
| $E_{45}$ | 45° Ply stiffness | $[GPa]$ |
| $E_{90}$ | 90° Ply stiffness | $[GPa]$ |
| $E_{norm\,zwick}$ | Normalized laminate stiffness from extensometer | $[GPa]$ |
| $E_{norm\,DIC}$ | Normalized laminate stiffness from DIC | $[GPa]$ |
| $E_{xt}$ | Tensile stiffness in $X$ direction | $[GPa]$ |
| $F_{max}$ | Maximum force | $[N]$ |
| $f$ | Frequency | $[Hz]$ |
| $G$ | Adhesive shear stiffness | $[GPa]$ |
| $I$ | Moment of inertia | $[m^4]$ |
| $I_{\#-\#mm}$ | Amperage during welding at a section | $[A]$ |
| $J_0$ | Current density at the surface | $[A/m^2]$ |
| $J_d$ | Current density at distance d | $[A/m^2]$ |
| $K_t$ | Stress concentration factor | $[-]$ |
| $L$ | Length | $[mm]$/$[m]$ |
| $L_{stepped}$ | Stepped scarf overlap length | $[mm]$ |
| $n_0$ | Number of 0° plies | $[-]$ |
| $n_{\pm 45}$ | Number of $\pm 45$° plies | $[-]$ |
| $n_{90}$ | Number of 90° plies | $[-]$ |
| $N_{PPS\,Elm}$ | Number of PPS elements | $[-]$ |
| $n_{total}$ | Total number of plies | $[-]$ |
| $P$ | Applied point load | $[N]$ |
| $q$ | Load per unit length | $[N/m]$ |
| $R$ | Radius | $[-]$ |
| $R_f$ | Number of failed PPS elements over total PPS elements | $[-]$ |
| $s$ | Standard deviation | $[-]$ |
| $S$ | Shear failure strength | $[MPa]$ |
| $t_\#$ | Thickness measured at different locations | $[mm]$ |
| $t/t_{ref}$ | Specimen thickness over reference thickness | $[-]$ |
| $t_{avg}$ | Average thickness | $[mm]$ |
| $T_{avg}$ | Average temperature of all $T_{max\,TC}$ along the weld-line | $[°C]$ |
| $T_g$ | Glass transition temperature | $[°C]$ |
| $t_lam$ | Laminate thickness | $[mm]$ |
| $T_m$ | Melting temperature | $[°C]$ |
| $T_{max\,TC}$ | Maximum temperature at a TC location | $[°C]$ |
| $T_{max}$ | Maximum temperature during a welding cycle | $[°C]$ |
| $t_{ply}$ | Ply thickness | $[mm]$ |
| $TC_\#$ | Maximum temperature measured at a thermocouple location | $[°C]$ |
| $w$ | Width | $[mm]$ |
| $w_0$ | Initial specimen width | $[mm]$ |
| $X_t$ | Tensile failure strength in $X$ direction | $[MPa]$ |
| $X_C$ | Compressive failure strength in $X$ direction | $[MPa]$ |
| $y$ | Location from centerline | $[m]$ |
| $Y_t$ | Tensile failure strength in $Y$ direction | $[MPa]$ |

|  |  |  |
|---|---|---|
| $\alpha_{brittle}$ | Scarf angle for brittle failure | $[°]$ |
| $\alpha_{ductile}$ | Scarf angle for ductile failure | $[°]$ |
| $\alpha_{plastic}$ | Scarf angle for plastic failure | $[°]$ |
| $\gamma_f$ | Adhesive shear strain failure | $[-]$ |
| $\delta$ | Penetration depth | $[m]$ |
| $\delta_c$ | Deflection due to applied force | $[m]$ |
| $\varepsilon_{F_{max}}$ | Strain at $F_{max}$ | $[-]$ |
| $\varepsilon_u$ | Ultimate laminate strain | $[-]$ |
| $\mu$ | Magnetic permeability | $[H/m]$ |
| $\rho_e$ | Electric resistivity | $[\Omega m]$ |
| $\rho_{lam}$ | Laminate density | $[kg/m^3]$ |
| $\sigma_{11}$ | Stress in $11$ direction | $[MPa]$ |
| $\sigma_{22}$ | Stress in $22$ direction | $[MPa]$ |
| $\sigma_{33}$ | Stress in $33$ direction | $[MPa]$ |
| $\sigma_{12}$ | Stress in $12$ direction | $[MPa]$ |
| $\sigma_{23}$ | Stress in $23$ direction | $[MPa]$ |
| $\sigma_{31}$ | Stress in $31$ direction | $[MPa]$ |
| $\sigma_m$ | Stress due to bending moment | $[MPa]$ |
| $\sigma_{max}$ | Normalized maximum stress | $[MPa]$ |
| $\sigma_u$ | Ultimate laminate stress | $[MPa]$ |
| $\sigma_x$ | Stress in $X$ direction | $[MPa]$ |
| $\sigma_{x\,ut}$ | Ultimate tensile $X$ strength | $[MPa]$ |
| $\sigma_{x\,uc}$ | Ultimate compressive $X$ strength | $[MPa]$ |
| $\sigma_y$ | Stress in $Y$ direction | $[MPa]$ |
| $\tau_f$ | Adhesive shear strength | $[MPa]$ |
| $\tau_{max\,norm}$ | Normalized shear strength failure of the specimen | $[MPa]$ |
| $\tau_{xy}$ | Shear stress in the laminate | $[MPa]$ |
| $\tau_{xy\,u\,PPS}$ | Adhesive shear strength | $[MPa]$ |

# List of Abbreviations

| | |
|---|---|
| **3D** | Three-dimensional |
| **5HS** | Five Harness Satin Weave |
| **AC** | Alternating Current |
| **BEM** | Boundary Element Method |
| **CF** | Carbon Fiber |
| **CFRTP** | Carbon Fiber Reinforced Thermoplastic |
| **CNC** | Computer Numeric Control |
| **COV** | Coefficient of Variation |
| **CT** | Continuous |
| **CTI-#** | Continuous Scarf Welding Part |
| **CTI-T#** | Continuous Scarf Tensile Test Specimen |
| **CV** | Conventional |
| **CVI-#** | Conventional Scarf Welding Part |
| **CVI-T#** | Conventional Scarf Tensile Test Specimen |
| **CZM** | Cohesive Zone Modeling |
| **DC** | Direct Current |
| **DZM** | Damage Zone Modeling |
| **FEM** | Finite Element Modeling |
| **FEP** | Fluorinated Ethylene Propylene |
| **GF** | Glass Fiber |
| **ILSS** | Inter Laminar Shear Strength |
| **IR** | Infrared |
| **IW** | Induction Welding |
| **KVE** | Kok & van Engelen |
| **LSS** | Lap Shear Strength |
| **N90-T#** | Normal thickness 90° tensile test specimen |
| **PPS** | Polyphenylene Sulfide |
| **PR-1** | Pristine part |
| **PR-T#** | Pristine Tensile Test Specimen |
| **RW** | Resistance Welding |
| **ST** | Stepped Lap |
| **STI-#** | Stepped Lap Welding Parts |
| **STI-T#** | Stepped Lap Tensile Test Specimen |
| **T90-T#** | Thin thickness 90° tensile test specimen |
| **TPC** | Thermoplastic Composite |
| **TSC** | Thermosetting Composite |
| **UD** | Uni-Directional |
| **UW** | Ultrasonic Welding |

# Abstract

This master thesis research investigates the possibility to repair carbon fiber thermoplastic aircraft structures using induction welding. Carbon fiber is conductive and heats up when placed inside an alternating magnetic field. A generator, coil, and pressure frame are needed to perform induction welding. The support plates needed to pressurize the carbon fiber parts need to be non-conductive, non-magnetic, temperature resistant, stiff at high temperatures, and thermally insulating.

The material used is five harness satin weave carbon fiber PPS supplied in pre-consolidated plates and unconsolidated semi-preg. Three different joint geometries are used in this investigation: a conventional scarf, a continuous scarf, and a stepped lap joint. The stepped lap joint and the conventional scarf are milled using a CNC machine. The continuous scarf is produced in a press using specialized tooling and a press program prescribed by TenCate.

Of each type two specimens are produced: an induction welded specimen and a press joined specimen. The specimens are tested in tension to determine the tensile strength and stiffness. This gives the performance of the induction welded joints with respect to the press joined specimens. Additionally, both of the welded specimens are compared to the pristine specimens.

By measuring the temperature along the weld-line of multiple test specimens, an induction welding program is obtained for each joint type. Achieving a consistent temperature along the weld-line is challenging due to the thermal conductivity of carbon fibers and other effects inside the laminate. Similar to the continuous scarfed specimens, the press joined specimens are created using specialized tooling.

Before testing the specimens in tension, they are scanned using a C-scan. The press bonded specimens show no flaws, whereas the induction welded specimens do not return the signal to the transducer. Micrography of the specimens shows similar results as the C-scan. The press joined specimens show little to no flaws and the induction welded specimens show a significant amount of voids and small unjoined sections near the tips for the continuous scarf and stepped lap specimen.

The tensile tests show that all induction welded joints perform less than the press joined specimens with a percentage of about 73-78%. The conventional scarf and the continuous scarf result in a similar failure strength recovery of about 44% of the pristine failure strength for the press joined specimens. Both the conventional scarf and the continuous scarf show similar behavior in welding and the tensile testing, but the continuous scarf is more difficult to produce. Therefore the conventional scarf joint is preferred over the continuous scarf joint. The stepped lap joint has the best performance, recovering about 59% of the pristine stiffness. The stiffness of all tested specimens is between 92%-99% of the pristine stiffness.

Inspection using digital image correlation and finite element modeling indicates the failure initiates inside the PPS matrix in between the parts at the location of the first or last step. Finite element modeling also suggests that a smaller angle for the scarf joint or a longer overlap for the stepped lap joint would increase failure strength.

# 1

# Introduction

This master's thesis is performed at Kok & Van Engelen Composite Structures (KVE Composites) in The Hague in collaboration with the Aerospace Engineering faculty of the TU Delft. This chapter contains the motivation, research questions, and global structure of the report.

## 1.1. Motivation

Composites in the aerospace industry have experienced a steady growth in the past few decades. Airliners such as the Boeing 787, Airbus A350, and Airbus A380 are produced with 50%, 53% and 22% composite materials respectively [7, 8]. Smaller and military aircraft, which are subjected to less strict regulations than commercial airliners, have already been constructed solely from composites [8, 9].

The majority of the composites used in aircraft nowadays are Thermosetting Composites (TSC). Although Thermoplastic Composites (TPC) have higher material cost, require higher processing temperatures, and higher processing pressures, their superior toughness, unlimited shelf life, and ability to be welded make them an interesting alternative [10].

Of the different welding processes for TPC, Induction Welding (IW), Resistance Welding (RW), and Ultrasonic Welding (UW) are the most mature and promising for automation [1, 11, 12]. These processes can roughly be sorted into three different applications: IW is most suited for complex shapes and continuous welds, RW is best applied to long straight welds, and UW is best suited for spot welding applications [12]. An additional benefit to IW is that Carbon Fibers (CF) can be heated without an additional susceptor.

Data gathered in 1996, collected from about 6.6 million flights, show that a crack, hole, or delamination in composite parts occurs once per aircraft per year [13]. As the amount of composites in aircraft has only grown, the number of composite defects has likely increased as well. As unscheduled downtime of an aircraft can result in cost as high as $100 000 per day, it is essential to have good repair methods available for TPC and TSC [14].

Traditional repair methods, applying an external patch using fasteners, induce stress concentrations that reduce the strength of composite structures. Additionally, external patches adjust the aerodynamic properties of the aircraft. In order to restore the original properties of the structure, stepped lap or scarf repairs can be used. These three repair types are shown in Figure 1.1. To avoid the stress concentrations induced by fasteners, repair patches can be bonded using adhesive or can be co-bonded by curing a TSC on to the original structure. Although these methods are effective for TSC, TPC need extensive surface treatment before adhesive can be applied, making welding an interesting alternative [15]. Theoretical research has shown that for an average composite permanent repair welding can be used to reduce the repair time from 15-16 hours to 5.5-7.5 hours [14].

In this thesis the possibility to repair Carbon Fiber Reinforced Thermoplastic Composites (CFRTP) using induction welding is investigated. As will become clear in Chapter 2, there have been limited recordings of repairs to TPC using welding, hence the research will be limited to the joining of a straight welding section instead of a patch repair.

Figure 1.1: An external patch repair (top), a stepped lap repair (middle), and a scarf repair (bottom)

## 1.2. Research Questions, Aims, and Objectives

To guide the project and ensure the goal is reached, a research question is formed. This research question, shown below, is supported by a number of sub-questions.

*Is an induction welded scarf or stepped lap repair a feasible method to repair CFRTP aircraft structures and regain pristine strength and stiffness?*

1. *What tooling and process parameters are necessary to bond a scarf or stepped lap joint?*
   (a) *What are the technical problems that need to be overcome to have a successful induction welding repair?*
   (b) *What are the material problems that need to be overcome to have a successful induction welding repair?*
2. *Which scarf angle/overlap length should be used to recover the pristine strength?*
3. *Which joint type results in the best performing joint?*
   (a) *Which repair type results in a strength closest to the pristine specimen?*
   (b) *Which repair type results in a stiffness closest to the pristine specimen?*
4. *Are the strength and stiffness recovered to within 10% of the pristine properties?*

Following from the research question is the research objective, which is stated below:

*Investigating the feasibility of induction welded scarf or stepped lap repairs in tensile CFRTP aircraft structures using experiments and simulations*

Similar to the research question, four sub-objectives are formulated to help define the scope of this project. These objectives are listed below.

- *Determine the welding process parameters that result in a proper joint along the interface using experiments*
- *Use analytic equations to determine the required scarf angle or stepped lap overlap to recover pristine strength*
- *Use tensile testing to establish whether the three induction welded scarf joints have strength and stiffness properties within 10% of the pristine properties*
- *Determine the best performing scarf design based on the stiffness, strength, and process parameters*

## 1.3. Structure of the Report

This thesis consists of six chapters. The second chapter contains the literature review, which elaborates on the research performed in the field of thermoplastic repair, induction welding, and inspection techniques. In the third chapter the conceptual design is explained, selecting the material and geometrical parameters of the joints. In this chapter the coil parameters are mentioned, as well as the test method used to evaluate the joints. A short section is dedicated to the possible use of heat sinks to draw away heat from areas that do not need to reach a higher temperature than the $T_m$.

In the fourth chapter the production of the continuous scarf, the pressure frame and the welding station, the induction welded specimen, and the press joined specimens are discussed. In the fifth chapter the produced specimens are tested. First non destructively, using a C-scan, before Micrography is performed and the joints are tested in tension to determining their performance. The tensile tests are also simulated using Finite Element Modeling (FEM) to investigate the exact cause of failure. This thesis is concluded in Chapter 6.

# 2

# Literature Review

In this chapter, the state-of-the-art of TPC repair and IW are discussed. In the last section, inspection techniques are compared.

## 2.1. Thermoplastic Repair

Scarf or stepped lap repairs are the aerodynamically flush alternative to externally bonded or bolted patches. Additionally, the load eccentricity of an externally bonded patch is significantly higher. An overview of the best practices in such repairs is provided in Section 2.1.1. Simple analytical equations exist to estimate the required scarf angle, which are discussed in Section 2.1.2. A FEM analysis, as reviewed in Section 2.1.3, can be used to optimize the design. This section is concluded with a short discussion about the fatigue sensitivity of scarf joints.

### 2.1.1. Scarf Joints Best Practice

Using FEM, parametric studies have been performed investigating the optimum scarf angle. These studies concluded either that a smaller scarf angle [16–19], or a scarf angle of 3° is the optimum scarf angle [20–23]. As the scarf angle decreases, the load is transfered more through shear and less through peel. For most common aerospace adhesives, the failure mode changes from adhesive failure to adherent failure at around 3°. Any additional reduction in angle does not lead to an increase in the failure strength [24–26].

These parametric FEM studies also showed that the deviation from the average shear stress can be significant, especially for smaller scarf angles. In a $[0_2/90_2/0_2/90_2]_s$ laminate with a load applied in the 0° direction, the highest peak stresses were observed close to the 0°, and thus stiffest, plies in the laminate [19]. Breitzman et al. used a downhill simplex optimization algorithm to find the patch lay-up resulting in the lowest peak stresses [24, 27]. Although his optimized laminate was unbalanced, unsymmetrical, and did not match the stiffness of the parent laminate it was concluded that high stiffness plies in the parent laminate are best matched by low stiffness plies in the patch laminate. A similar conclusion is reached by Neilson et al. using a genetic algorithm while taking into account the stiffness of the adherent and imposing a symmetric laminate constraint [23]. A stiffness match is required to ensure the load path of the original structure is not altered and asymmetrical laminates introduce unwanted bending in the structure.

It is advised to place the stiffest plies away from the surface because the increased peak stresses may cause the feathered edge of the scarf to peel off [28–30]. However this can not always be combined with the advise to match high stiffness and low stiffness plies from Breitzman and Neilson et al. Another method to reduce the peel stresses of the thin edges is to add an over-ply on top of the patch. The feathered edge peeling off and an over-ply added to prevent the peeling off is shown schematically in Figure 2.1. It has been shown that an over-ply can significantly increase the failure load of the scarf joint [27, 30, 31]. An over-ply, although beneficial for the ultimate strength, distorts the surface, adds an eccentricity to the joint, and adds weight to an otherwise weight neutral repair.

The thickness of the used adhesive or added matrix layer is also a point of interest. If the adhesive is too thin, it will show brittle behavior. Resulting in a high sensitivity to stress peaks. If it is too thick,

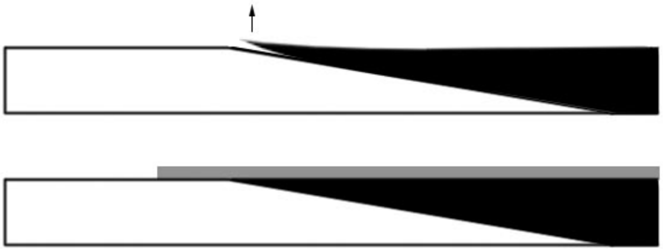

Figure 2.1: Feathered edge peeling off under tensile loading (top) and an added over-ply to prevent the feathered edge from peeling off (bottom)

its behavior will be plastic, reducing the effective load transfer through the adhesive [32]. It is common to have an adhesive thickness of 0.1-0.3 $mm$ [22, 32, 33].

The above mentioned practices hold for both a tapered and a stepped lap scarf. For a stepped lap scarf, it should be added that the transfered load depends heavily on the number of steps in the joint. More steps will decrease the peak stresses at the edges of a step, increasing the failure strength of the joint.

### 2.1.2. Analytical Solutions of Scarf Joints

Analytical methods to calculate the exact stresses inside scarf patches are not available, but simple analytical equations to estimate the scarf angle of joints are discussed in literature [26, 34, 35]. The equation, shown in Equation (2.1), is derived from simple stress transformation and is only valid for parent and patch laminates of equal stiffness and expansion coefficient. For aircraft structures, which are often designed using a maximum strain criteria, the first form of the equation is used. For this thesis, $E\varepsilon_u$ is replaced by the failure stress of the laminate.

$$\alpha_{plastic} = \frac{1}{2}\sin^{-1}\frac{2\tau_f}{E\varepsilon_u} = \frac{1}{2}\sin^{-1}\frac{2\tau_f}{\sigma_u} \tag{2.1}$$

Equation (2.1) is valid for adhesives or added matrix layer with plastic behavior. Wang et al. extended this to brittle and ductile adhesive [35]. For brittle adhesives it is necessary to include the stress concentrations in the adhesive, which can be included using a $K_t$ as shown in Equation (2.2). An approximation of this stress concentration factor is given in Equation (2.3). Investigations using FEM have shown that this equation gives conservative results as the equation gives an upper bound for the $K_t$ [21].

$$\alpha_{brittle} = \frac{1}{2}\sin^{-1}\frac{2\tau_f}{K_t\sigma_u} \tag{2.2}$$

$$K_t = \frac{n_{total}}{n_0 + n_{\pm 45}\frac{E_{45}}{E_0} + n_{90}\frac{E_{90}}{E_0}} \tag{2.3}$$

To estimate the ductile failure of a scarf repair Equation (2.4) is used. This equations is equal to Equation (2.2) except for $\tau_p$, which is replaced by the maximum shear strain derived using Neuber's Rule.

$$\alpha_{ductile} = \frac{1}{2}\sin^{-1}\frac{2\sqrt{G\tau_f\gamma_f}}{K_t\sigma_u} \tag{2.4}$$

The equations mentioned above are purely based on the shear stresses in the adhesive or matrix layer. Although peel stresses are present, these are insignificant compared to the shear stresses for scarf angles smaller than 5° [16, 33]

For stepped lap repairs, the length of the overlap needed to withstand the ultimate stress can be estimated using Equation (2.5). It is important to note that the number of steps has a significant influence on the peak stresses in the adhesive. Increasing the number of steps will increase the joint strength [35, 36].

$$L_{stepped} = t\frac{\sigma_u}{\tau_f} \tag{2.5}$$

### 2.1.3. Modeling of Scarf Joints

FEM has enabled more detailed analysis of the stresses and strains inside the scarf joint or repair. The laminate is modeled per ply with at least one element through the thickness of the ply, although often the mesh is refined near the interface region [18, 22, 26, 37].

The failure of the parent and patch laminate is modeled using conventional criteria such as Tsai-Wu, Tsai-Hill, and Hashin [22, 26, 35, 38]. The failure in the adhesive is often analyzed using the maximum shear stress [22, 26, 38]. Alternatively Christensen failure criterion can be used, which is an extension of von Mises failure criterion which also includes brittle failure [39]. Riccio et al. compared three different methods to model the plastic failure behavior of the adhesive. They concluded that a multi-linear stress-strain curve performs better than both the stress-strain curve at room temperature and the Drucker-Prager yield criterion [37]. To predict final failure, Damage Zone Modeling (DZM) can be used. For this method the model is run at the experimentally determined failure load, resulting in a percentage of failed elements. The geometry of the model can now be changed and the new geometry is assumed to fail at the same percentage of failed elements. The use of this method is limited as major changes in the geometry may result in different failure modes [26, 40].

For ply failure, the Tsai-Hill criterion will be used. For the adhesive failure it is unknown whether the failure will be brittle or ductile and whether shear is the primary failure mode. Therefore, Christensen criterion will be used to determine failure in the matrix layer in between the two parts. Once the number of failed elements is known and the failure force has been determined experimentally, DMZ modelling can be used to predict the effect of slight changes to the geometry.

### 2.1.4. Fatigue Considerations

In general, CFRTP shows superior fatigue behavior when compared to their metal counterparts. Unlike homogeneous materials, where initiation and propagation of a single crack dominate the fatigue behavior, fatigue in composites consists of fiber/matrix de-bonding, delaminations, fiber fractures, or matrix cracking [41]. Several studies have found that the impact of typical bond line flaws or anomalies on the static strength of a scarf repair is negligible. However, when tested in fatigue, flaws or defects can significantly influence the failure strength [33, 42, 43]. No comparison between the fatigue behavior of a pristine specimen and a scarfed or stepped joint has been found.

It is unknown what influence a scarfed or stepped lap repair has on CFRTP structures and it is considered beyond the scope of this thesis to investigate this. If a proper repair is achieved using this method, more research in terms of fatigue will be required to validate the long term behavior.

## 2.2. Induction Welding

This section consists of three parts, the first section starts with a introduction on induction heating which is followed by a review of the different heating mechanisms that can occur in CF weaves during induction welding. Section 2.2.3 then discusses what to take into account when designing and producing an induction coil. This section is concluded by a short subsection on the FEM of induction coils.

### 2.2.1. Composite Joining using Induction Welding

For induction heating, three different instruments are required: a generator, an induction coil, and a susceptor [3]. The generator supplies an Alternating Current (AC) to the induction coil with a certain frequency and Amperage. This current induces an alternating magnetic field. When an electrically conductive susceptor is placed inside this magnetic field a current is generated in the susceptor, opposing the change in direction in the magnetic field [44]. The induced currents are called eddy currents. In combination with the internal resistance of a material these currents result in an elevated temperature in the material. Alternatively, magnetic materials can be heated as well. These materials, which could also be electrically conductive, generate heat through magnetic hysteresis losses [12].

A few requirements need to be met for a successful induction weld. The interface should be heated above the $T_m$ for crystalline or semi-crystalline materials or the $T_g$ for amorphous materials [1, 11]. Additionally the parts should be pressurized to prevent decompaction and ensure intimate contact between the parts. For the material used in this thesis, five harness satin weave (5HS) CF/Polyphenylene Sulfide (PPS) by TenCate, the critical decompaction pressure has been found to be 4.9 $bar$ [45].

The magnetic field induces currents in the susceptor, which in turn induces a magnetic field in the opposite direction with respect to the original magnetic field. Due to this secondary magnetic field, the top of the laminate heats up more than the bottom of the laminate. This is called the skin effect [1, 46, 47]. To alter the temperature profile, the skin can be cooled. Two cooling methods have been mentioned in literature: active cooling using air or passive cooling using a heat sink [48–50]. Apart from cooling the surface, the heat sink also controls the cooling process after heating. A more crystalline structure in the matrix can be obtained by a slower cooling process [50]. As the heating inside CF laminates relies on the flow off electricity inside the laminate, isolating layers, such as a 10 $gsm$ Glass Fiber (GF) tissue, can be added in between CF UD plies to prevent the heating of these plies [11]. This method can be used to focus the heat generation to a specific part of the laminate.

An important factor in the heating of the laminate is the penetration depth $\delta$. The penetration depth can be calculated using Equation (2.6), in which $\rho_e$ is the electric resistivity in $\Omega m$, $f$ is the frequency of the magnetic field in $Hz$, and $\mu$ is the magnetic permeability of the CFRTP in $H/m$ [51]. This depth is defined as the depth where the eddy currents have decreased to $1/e$ or 37% of its value at the surface [46]. As can be deduced from the equation, a higher frequency results in a lower penetration depth. If $\delta$ is significantly larger than the thickness of the workpiece, the temperature distribution can be considered uniform throughout the thickness [51]. Typical induction welding frequencies are about 200-500 $kHz$, resulting in a penetration depth of about 7-25 $mm$ [3]. A disadvantage of a lower frequency is that more power is needed, which can become the limiting factor.

$$\delta = \sqrt{\frac{\rho_e}{\pi f \mu}} \tag{2.6}$$

Another effect that should be taken into account is the edge effect. When the specimen becomes smaller, the loops of the eddy currents can be restricted. This forces the currents to follow the edge of the laminate, creating a higher current density as shown in Figure 2.2. The higher energy densities result in higher temperatures near the edge of the laminate.

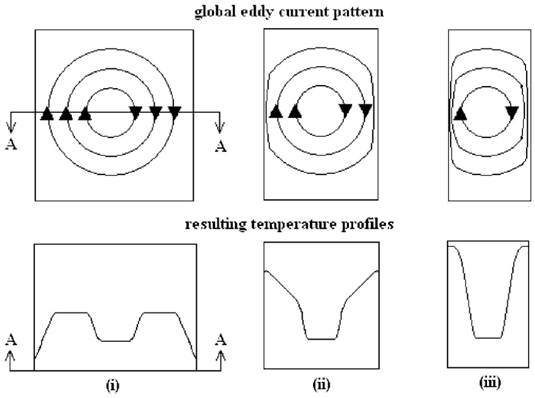

Figure 2.2: Restricted eddy currents due to the edge effect [1]

As will be mentioned in Section 2.2.2, conductive loops must exist in a laminate in order to generate heat using induction welding. When an isotropic material or a quasi-isotropic laminate is used, the heating pattern will mirror the shape of the coil. However, when a laminate becomes more orthotropic the heating pattern can deviate significantly. Following the fibers instead of mirroring the shape of the coil [52].

### 2.2.2. Heating Mechanism

For metals, heat is generated by internal resistance according to Joule's first law or hysteresis loss for magnetic materials [53]. In CFRTP, the CFs act as the electrical conductor and the matrix acts as the insulator. Due to the conductive properties of CF, it is possible to heat a CFRTP without an external susceptor. A requirement for susceptorless welding in CFRTP is that the CF form a closed conductive loop such that the eddy currents can be created. As such, Uni-Directional (UD) laminates hardly heat up when placed inside an alternating magnetic field.

Three different heating mechanisms are recognized when eddy currents are applied to CF: Joule loss, dielectric heating, and contact resistance heating [1, 54–57]. For Joule loss, heating the CFs heat up because of internal resistance of the fibers when a current is applied. For dielectric heating, there is a small amount of matrix material between two fibers. The fibers, isolated by the PPS matrix, act as an capacitor, heating at fiber junctions. Contact resistance heating also happens at the fiber junctions, although now the fibers are in contact with each other.

There have been many studies investigating the dominant heating mechanism in susceptorless CF welding, although no consensus has been reached on the exact heating mechanism. Miller et al. found that Joule heating is the primary heating occurring in CFRTP welding. However, this is based on the assumption that all the fibers are in good contact with each other [51, 57]. Fink et al. observed that even when the fibers are not in contact with each other, heating still occurred. They proposed a theory stating that the fibers, separated by a small amount of non conductive matrix material, act as capacitors. As such, heat is generated in the matrix by dielectric losses [58–61]. Yarlagadda et al. introduced the theory that contact resistance at the fiber junctions should also be considered. They connected a Direct Current (DC) power source, ruling out the dielectric effect which needs an AC, to woven CFs and showed the heating still occurred at the junction [52].

Yarlagadda et al. extended their research creating a model that takes in account the three different heating mechanisms. They concluded that all three mechanisms can be dominant depending on the processing parameters. Below a contact resistance of $10^3$ Ω for CF, fiber heating becomes the predominant heating mechanism [57]. In UD materials, contact resistance is in general higher than the threshold resistance, making junction heating the dominant heating source. Woven fabric have a low enough contact resistance to facilitate Joule heating. If both dielectric and contact resistance are present, contact resistance is the dominant heating mechanism. One should note that during the welding process, when temperature rises and pressure is applied, the contact resistance may reduce allowing fiber heating to become the dominant heating mechanism [57].

### 2.2.3. Coil Design

Induction welding has been used in metals since 1916 [1]. As such, the coil design has been subject to many studies and useful guidelines are available. Copper is often selected for coil material due to its high thermal and electrical conductivity, and formability. A common issue regarding production of a coil is collapse of the tube. This can be prevented by filling the tube with a granular material such as sand during manufacturing, simulating a solid rod [62].

The leads should be placed as close together as possible while preventing arcing. The closer the leads are, the more they cancel out the magnetic field they create, reducing energy loss by limiting the size of redundant magnetic fields. The combined inductance of the leads should be at least 10 times smaller than the inductance of the coil to limit the voltage loss in the leads to 10% or less [62].

Besides the design of the coil itself, it is also possible to change the magnetic field using concentrators. Concentrators are soft magnetic materials with low electric conductivity and a relative permeability of less than one. This material is placed around a coil, containing the magnetic field in a smaller area. This results in a higher flux density in the workpiece. [2]. A visual representation of this effect is shown in Figure 2.3.

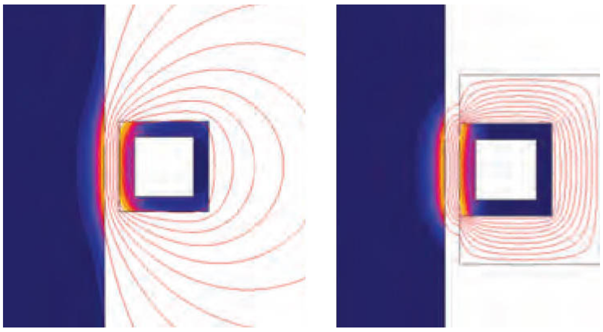

Figure 2.3: The effect of a concentrator placed around the coil on the magnetic field distribution [2]

There are three basic geometries that are often used; a single-turn helical, multi-turn helical, and pancake coil. These three different coils are illustrated in Figure 2.4. A single-turn coil creates a magnetic field through the inside of the coil, as shown in Figure 2.5. A multi-turn coil creates a magnetic field with the same basic shape but with extended and more powerful as the single turn coil. A pancake coil has the ability to heat a big flat area.

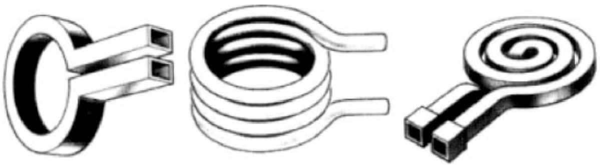

Figure 2.4: A single-turn helical, multi-turn helical, and pancake coil [3]

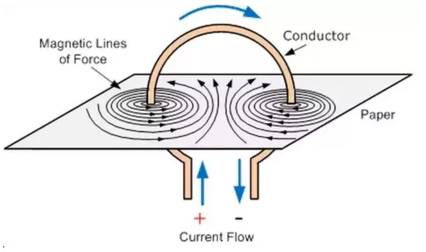

Figure 2.5: Magnetic lines through a single-turn helical coil [4]

### 2.2.4. Heating Mechanisms and Modeling of CFRTP Induction Welding

To predict the heat generated in the laminate FEM is used. Full three-dimensional (3D) analysis has only recently been available due to the coupling of three different physical models. Namely thermal, structural, and electro mechanical. In combination with the ongoing discussion on which heating mechanism is predominant, FEM of CF induction welding is still in the early stages [47].

Some recent papers do not discuss the different heat generation mechanisms and state that the heat is generated by Joule losses [53, 63]. While other acknowledge the three different heating mechanisms but assume only Joule losses in the model [46, 49, 55]. O'Shaughnessey argues that by measuring the resistivity of the complete laminate, the resistance of the junction is included as well. This would eliminate the need to include both effects in the analysis [46].

The only model taking into account all three mechanisms is made by Yarlagadda et al. to identify the effect of each mechanism [52]. Later work by Kim and Lundström use a simplified version of this model by generalizing dielectric heating and contact resistance to a single junction resistance mechanism. This is valid as both dielectric impedance and the contact resistance can be modeled as a resistor at the junction of the fibers [56, 64].

There are two types of analysis that can be run. Either a Boundary Element Method (BEM) is combined with FEM analysis or a full FEM analysis is run. In the case of a BEM/FEM analysis, the influence of the electro magnetic field on the outer face of the laminate is calculated. This is then used to determine the response of the laminate using a FEM analysis. An advantage of this method is that a moving coil can be simulated without having to calculate the electromagnetic response for each step. A full FEM analysis requires the modeling of laminate, coil, and surrounding air [47].

## 2.3. Inspection Techniques

Thermocouples are a common tool used to monitor the temperature of a specimen. Two issues arise when using thermocouples in induction welding, the first being that thermocouples may be influenced by the magnetic field. Thermocouples with magnetic materials are heated by magnetic hysteresis, influencing the measured temperature. Type E thermocouple are not affected by the magnetic field and give accurate measurements if the frequency is lower than 1 $MHz$ [59]. Type K thermocouples, which are often used in literature, could be influenced by the magnetic field as they contain Alumel. The error has been recorded to be as high as 150% when the thermocouple is at 100$^{\circ}C$ and placed inside a strong magnetic field [65]. The curie temperature of Alumel is 152°$C$, at which point the thermocouple should no longer be influenced by the magnetic field [66].

The second issue with thermocouples is that, when placed in between the two parts or at the surface of the specimen, they will be embedded in or leave an imprint on the specimen during welding. This makes it difficult to measure the interface temperature for the specimens that will be used for tensile testing without affecting the mechanical properties of the specimens.

Alternatively fiber optic sensors could be used. This analysis technique, based on glass fiber sensors, is not influenced by the magnetic field, can handle high temperatures, and is very accurate. The drawbacks are that the equipment is expensive, the cables are vulnerable, and the same issue regarding imprints on the specimens are present.

Thermal imaging using an Infrared (IR) camera can reveal the heat pattern at a surface of the specimen and, if validated using a thermocouple, give the exact temperatures at any point at the surface. Thermal cameras use infrared radiation emitted and reflected by the composite strip. Thermal imaging can also be used to find flaws in the specimen. A pristine specimen will heat up uniformly while flaws will disturb this heating process. This technique is relatively expensive and is less detailed than ultrasonic scanning [67, 68]. Shearography uses a similar method, but uses stress instead of heating. Structural flaws will disturb the strain pattern which would be uniform for a pristine specimen [67, 68].

Ultrasonic scanning is a non destructive testing method that is often used to find flaws in a composite structure. Ultrasonic scanning requires a couplant, such as water, to minimize the energy loss to the environment. C-scan, which has a good resolution and high scanning speed, can determine the flaw location, size, depth, and orientation. However, a disadvantage of C-scan is the difficulty to ensure accurate measurements [67, 69]. A Deliberate flaw, such as an inserted piece of Teflon on the interface, can help find the correct C-scan settings needed to find interface flaws.

Radiographic testing uses X-rays to visualize flaws in the structure. The application to CFRTP is limited due to the low absorption of X-rays by CFs. Penetrants can be used to highlight flaws, but this results in a contamination of the parts and only works if the flaw is breaking the surface [68].

Unlike the techniques mentioned above, micrography is a destructive testing method. By cutting a test specimen, polishing, and placing the sample under a microscope, detailed images of the interface in between the welded parts can be obtained. Preferably the cut is not placed parallel to one of the fibers directions to prevent fiber chipping during grinding. Such images give a good indication of the amount of voids and the quality of the bond.

## 2.4. Conclusion

Scarf or stepped lap joints are a necessity in the repair when the structure is to be restored to original strength, stiffness, and aerodynamic properties. Stiffness, should be matched for the parts and if possible low stiffness plies should be coupled with high stiffness plies to reduce the stress concentrations within a laminate. Scarf angles around 3° or stepped lap joints with multiple steps are needed to create strong joints, simple approximations can be used to estimate the needed scarf angle and stepped lap overlap length. FEM can be used to obtain a better insight in the failure location and can be used to investigate slight variations in a tested geometry.

Induction welding requires a generator, induction coil and a susceptor. In CFRTP the CF acts as a susceptor. The material should be heated above the melting point and be pressurized to at least 4.9 $bar$ for the complete duration of the weld. A lower frequency results in a larger penetration depth, at the cost of a higher power consumption. The edge effect can result in a distorted current flow in the specimen and should be taken into account.

For an efficient coil square oxygen free copper tubes should be used with leads with just enough spacing to prevent arcing. Concentrators can increase the efficiency of this coil as well. For this thesis, the efficiency of the coil is of less interest as only a few products need to be welded. Modeling of induction coils in combination with CF is still in its early stage and requires a lot of processing power if moving coils are to be simulated.

Non-magnetic thermocouples are the most reliable method to measure the temperature of the specimens during welding, although they can only be used during welding trials. During the welding of the final test specimens, an IR camera can be used to monitor the temperature. C-scanning is a reliable NDT method to inspect the laminate for defects when the set up correctly. Micrography is often used to get a more detailed look of the interface and possible flaws.

# 3

# Conceptual Design

In the next sections the conceptual design is discussed. First, the material used in this thesis is introduced after which the different repair concepts are explained. In Section 3.3, the reasoning behind the chosen coil is given and this chapter is concluded by a short section about heat-sinks.

## 3.1. Material

5HS CF/PPS, which is manufactured by TenCate and supplied as semi-preg and pre-consolidated panels, is the material used in this thesis. The pre-consolidated panels, produced as 3.66 $m$ by 1.22 $m$ panels on a press at 320°$C$ and 10 $bar$, are supplied at a dimension of 0.4 by 0.4 $m$. In consultation with KVE and TenCate it is decided to use a $[0/90]_{5s}$ stacking sequence, which resembles stacking sequences used by the aerospace industry. Given the simple stacking sequence, the maximum tensile stress in the laminate is equal to the maximum tensile stress for a single ply. The most important material and laminate properties are listed in Table 3.1.

Table 3.1: Material and laminate properties of TenCate Cetex Carbon T300 3K 5HS at 23°$C$

| Property | Value | Unit | Source |
|---:|:---:|:---|:---|
| $t_{ply}$ | 0.31 | $mm$ | [70] |
| $t_{lam}$ | 3.1 | $mm$ | [70] |
| $T_g$ | 90 | $^\circ C$ | [70] |
| $T_m$ | 280 | $^\circ C$ | [70] |
| $\tau_{xy\,u\,pps}$ | 32.1 | $MPa$ | [71] |
| $\rho_{lam}$ | 1550 | $kg/m^3$ | [70] |
| $\sigma_{x\,ut}$ | 757 | $MPa$ | [70] |
| $\sigma_{x\,uc}$ | 643 | $MPa$ | [70] |
| $E_{x\,t}$ | 55.8 | $GPa$ | [70] |

The recommended manufacturing pressure of CF/PPS is about 7-10 $bar$ [70]. If an already consolidated laminate is heated above $T_m$, the pressure can be reduced to a pressure of at least 4.7 $bar$ as mentioned in Chapter 2. Due to the woven CF material, it is expected that Joule heating is the predominant heating mechanism. The woven CF also ensures that eddy currents can flow almost unrestricted through a ply. However, it should be noted that in the area that needs to be heated, namely the interface between the parts, the fibers are no longer continuous. It is unclear how the eddy currents responsible for the heating will react to these discontinuous fibers.

## 3.2. Repair Design

As discussed in Section 2.1, the most efficient repairs in terms of load transfer and aerodynamics are scarf or stepped lap repairs. Three different type of repairs are compared in this thesis: a conventional (CV) scarf, a continuous (CT) scarf, and a stepped lap (ST) scarf, which are all shown in Figure 3.1. The conventional scarf and stepped lap scarf will be milled using a five axis Computer Numeric Control

(CNC) milling machine to ensure an accurate fit. Attempting to mill an infinitely thin scarf edge will result in damages at the thin edge and unpredictable behavior. Therefore, the first and last ply of the scarf repairs are stepped. The steps are 0.31 $mm$ high due to the ply thickness.

Induction welding requires the flow of electricity and it is yet unclear how a conventional milled scarf joint will behave during induction welding. The second scarfed repair concept, the continuous scarf, is added to ensure the flow of electricity along the interface of the joint. This continuous scarf is produced using special tooling and could provide a more uniform temperature distribution along the interface of the joint.

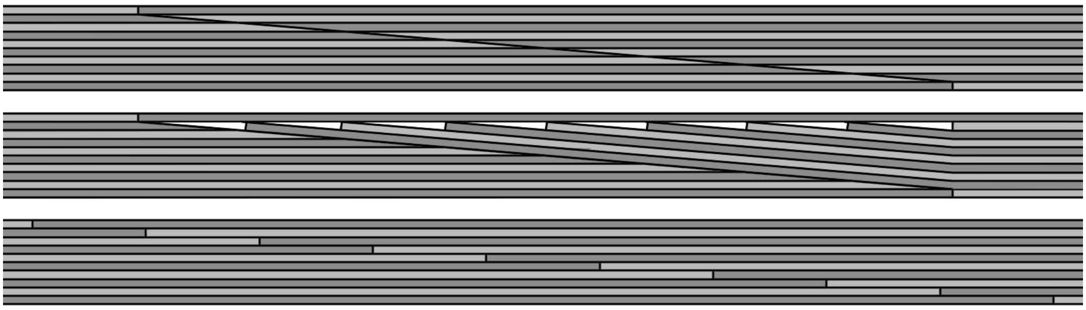

Figure 3.1: The geometries of a conventional scarf joint(top), continuous scarf joint(middle), and stepped lap joint (bottom)

The angle needed to transfer a certain load can be calculated using Equations (2.1), (2.2), (2.4) and (2.5). Because no additional PPS layer will be added in between the parts, it is expected that the scarf joint will fail in brittle failure. However, $K_t$ equals $1$ for the stacking sequence used and thus Equation (2.2) simplifies to Equation (2.1). This equation is used in Equation (3.1) to calculate the scarf angle. The stepped lap repair will be stepped for each layer to minimize the peel stresses at the start and end of each step. The overlap length needed is calculated using Equation (3.2).

$$\alpha_{scarf} = \frac{1}{2}\sin^{-1}\frac{2 \cdot 62.1e6}{758e6} = 4.7° \tag{3.1}$$

$$L_{stepped} = t\frac{\sigma_u}{\tau_f} = 3.1\frac{758e6}{62.1e6} = 37.8\ mm \tag{3.2}$$

These equations result in a scarf angle of 4.7° that is used for both the conventional and the continuous scarf which corresponds to an overlap of 30.2 $mm$. It should be noted that Equation (3.1) is derived assuming that the complete thickness of the laminate is used to create the scarf joint and transfer the shear load. The first and last ply are stepped, which reduces the area that is used to transfer the shear load. The steps in the scarf joint have been introduced to the design after the desired scarf angle has been calculated. The need for a lower scarf angle was not realized until after the laminates had been milled. The stepped lap joint needs an overlap of 37.8 $mm$ to fully transfer the failure load. The detailed geometry of the joints can be found in Appendix A.

## 3.3. Coil Design

The global design of the coil can be described by two variables: the length and the geometry. The frequency of the coil is mainly driven by its length. A longer coil results in a lower frequency, which in turn increases the penetration depth at the cost of a higher required voltage. The generator can generate up to 2 $kW$. A longer coil will have a higher resistance limiting the maximum current output. Previous work at KVE has shown that a frequency of 300 to 400 $kHz$ can be used up to a maximum current of about 300-350 $A$, which is the theoretical current limit of the generator.

The current density inside the laminate decreases exponentially following Equation (3.3), where $\frac{J_d}{J_0}$ is the normalized current density at distance $d$ from the surface and $\delta$ is the penetration depth as calculated by Equation (2.6). The magnetic permeability in this equation can be assumed to be equal to that of air, $1.256e^{-6}$ $H/m$, for non-magnetic materials [51]. The resistivity of CF/PPS has been measured to be $9.48553e^{-5}$ $\Omega m$ in the direction of the fibers at room temperature in previous work at KVE. At higher temperatures the penetration depth decreases, but the shape of the graph is similar.

$$\frac{J_d}{J_0} = \frac{1}{e^{\frac{d}{\delta}}} \tag{3.3}$$

Equation (2.6) can be inserted into Equation (3.3) to obtain the decrease in current density as a function of frequency at a certain depth. This function is plotted in Figure 3.2 for a frequency range of 200 to 400 $kHz$. In the figure, it can be seen that increasing the frequency below 300 $kHz$ provides a limited increase in the current density.

As mentioned before, the generator is able to provide the maximum current for a frequency range of about 300 to 400 $kHz$. The lower bound of this range, 300 $kHz$, will provide a slightly higher penetration depth and will be aimed for in the production of the coil. In Figure 3.3, coils frequency at 200 $A$ is plotted against the coil length. These values are taken from previous work at KVE Composites. A linear trend-line is plotted in the same figure, which shows that a length of about 800 $mm$ is needed to give a frequency of 300 $kHz$. By only using data from coils having a similar geometry as the coil used in this thesis, a more accurate prediction could be obtained. However, available data is limited so various coil shapes are used to construct the graph in Figure 3.3.

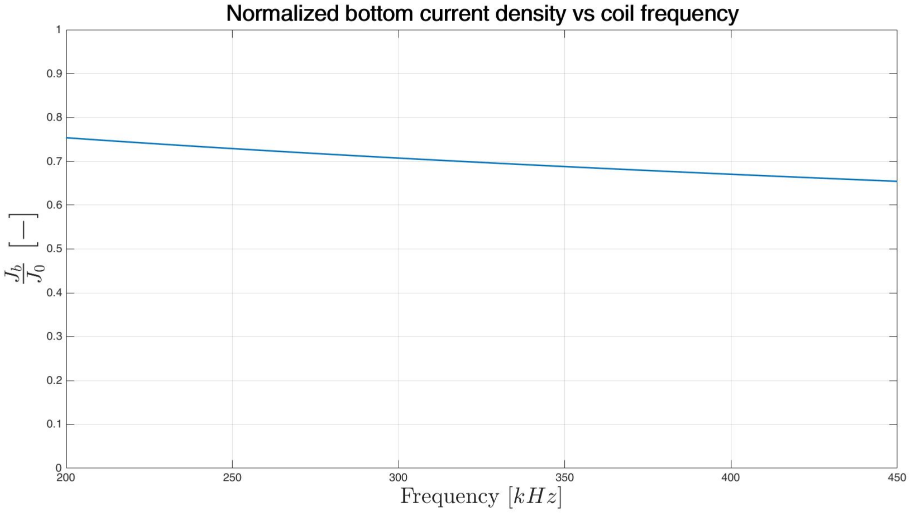

Figure 3.2: Bottom current density over top current density plotted against the coil frequency

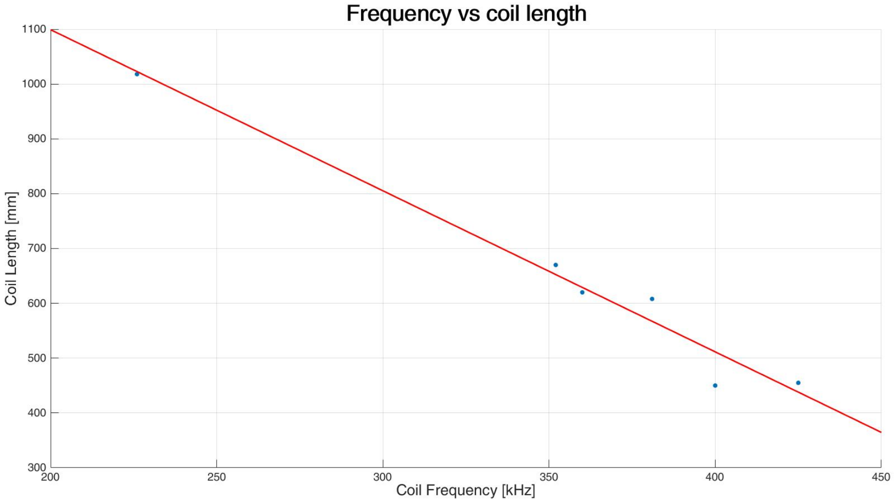

Figure 3.3: Coil length versus frequency at 200 $A$, data-points are obtained from previous work at KVE Composites fitted with a linear polynomial curve using Matlab

The scarf and stepped lap joint have a simple geometry, two flat plates with an overlap of 30.2 and 37.8 $mm$ that need to be welded together along a straight weld-line. Therefore, a simple single turn coil, shown in Figure 3.4, will be used. This leaves two variables to determine: the width of the coil and the angle of the coil with respect to the weld surface. In an attempt to determine these variables, the coil and the scarfed specimens are simulated in ANSYS mechanical APDL using an adapted version of a code available at KVE composites. This scarfed model, explained in Appendix B, does not agree with temperature measurements and cannot be used to predict the needed width or needed welding program.

Instead, a validated model of a pristine laminate is used to investigate the influence of different coil angles with respect to the laminate surface for a pristine laminate. Although the scarfed specimens is expected to react different, this model gives an indication on what heating pattern to expect. Two conclusions can be drawn. First of all, a longer heating time is needed when the angle of the coil with respect tot the surface is increased. Secondly, the size of the heated area does not change for an increased coil angle, but it does shift towards the lowest part of the coil. Both conclusions do not improve the heating pattern for the joint geometry. Therefore, a coil with a straight section parallel to the surface will be used.

As seen in Figure 3.5 the heated area essentially mirrors the coil. Therefore, the width of the straight section of the coil is set to 40 $mm$. This is slightly wider than the width of the stepped lap joint, the widest joint that needs to be welded. The final dimensions of the coil are shown in Appendix C. The total length of the coil is about 800 $mm$. The inner radius of the bends is set to 7.5 $mm$, which from previous experience at KVE is possible without wrinkling in the tube. The tube is filled with sand to prevent flattening or ripples during bending. A gap of 4 $mm$ between the leads is taken into account to prevent arcing between the leads. The copper tubing is bend by hand using 3D printed tooling to ensure the correct dimensions are obtained.

The coil is tested and results in a frequency of 340 $kHz$ and a maximum current of 345 $A$ for a static test. The maximum available current reduces to 335 $A$ when the welding head is moving at a velocity of 5 $mm/s$. Provided the frequency of 340 $kHz$, the penetration depth for this coil is calculated to be 8.4 $mm$. Although this penetration depth is larger than the laminate thickness of 3.4 $mm$, it is not significantly larger and an uniform temperature throughout the thickness can not be assumed.

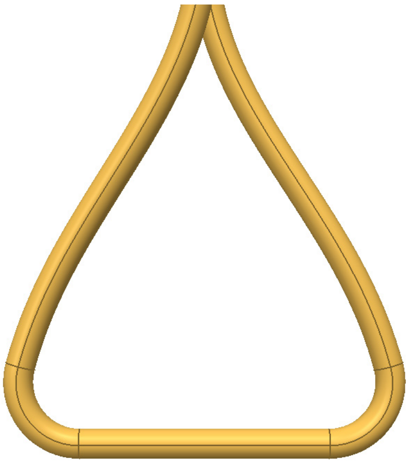

Figure 3.4: CAD drawing of the single turn coil used in this thesis

## 3.4. Heat-sink Design

Conventional CF induction welding applications have a heat-sink placed on one or two of the outer surfaces of the parts. Often this heat-sink also functions as a support to apply pressure to the parts. A fully overlapping heat-sink is not possible for the repair joint because the top and bottom surface at the interface need to be above the $T_m$ as well. Ceramic heat-sinks, placed at an offset with respect to the interface in between the composite parts, are considered. The heat-sinks are shown schematically in

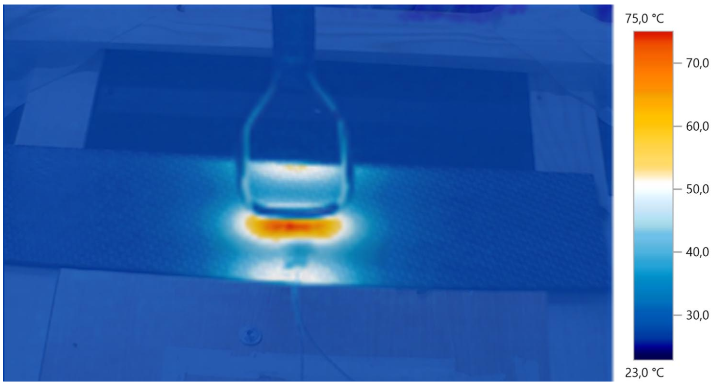

Figure 3.5: IR picture visualizing the heating pattern of a single turn coil

Figure 3.6.

Simulations are run to investigate the effect of these heat-sinks and whether they can be used to obtain an uniform temperature distribution along the interface in between the composite parts. As mentioned in Appendix B, the model does not result in realistic temperatures when a scarf joint is modeled. Instead, the effects of heat-sinks on the heating pattern in a pristine laminate, which is validated by KVE, is investigated using FEM. This resulted in two conclusions. First of all, the time needed to obtain a temperature of about $320^{\circ}C$ increased from 50 $s$ without heat-sinks to about 800 $s$ when heat-sinks are added. Secondly, the resulting heating pattern depends greatly on the positioning of the heat-sinks. An offset of a few millimeters results in different temperatures and heat distributions. As the model to predict the temperatures does not present realistic results, the position cannot be determined accurately. The longer heating duration and critical positioning of the heat-sinks led to the decision to continue without heat-sinks.

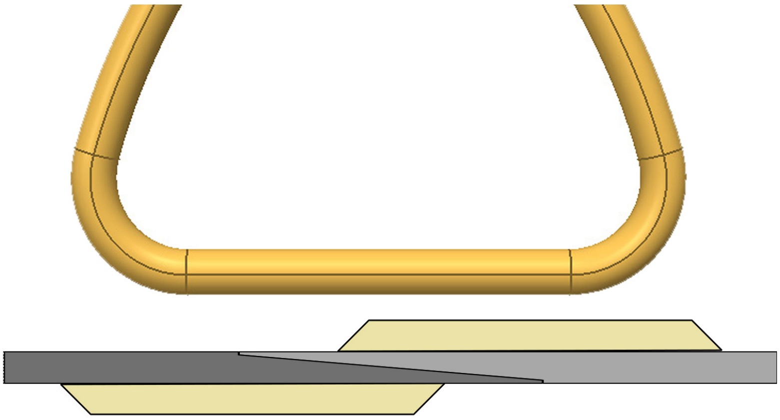

Figure 3.6: Schematic depiction of the heat-sinks placed at the top and bottom of the laminate with an offset with respect to the interface in between the two parts

## 3.5. Test Setup

Welding is performed using 130 $mm$ by 140 $mm$ parts for the CV and CT specimen and 130 $mm$ by 144 $mm$ parts for the ST specimen. The resulting welded specimens are 130 by 250 $mm$ due to overlap in the joints. The width of 130 $mm$ allows for four tensile test samples to be cut from the welded specimens, taking into account 30 $mm$ of waste material. Two methods will be used to join the parts. Induction welding and press joining. The induction welded parts will be compared to the press joined specimens and the pristine specimens to determine its performance.

The parts that will be welded together, and their corresponding identification, are listed in Table 3.2. All parts are milled into the preferred shape except for PR-1, which is not milled, and CTI-2 and CTP-2, which need to be produced using special tooling.

Table 3.2: The CNC milled and pressed parts and their identification before welding

| Joint | Heating Method | Name |
|---|---|---|
| Pristine | | PR-1 |
| Conventional Scarf | Induction | CVI-1, CVI-2 |
| | Joos Press | CVP-1, CVP-2 |
| Continuous Scarf | Induction | CTI-1, CTI-2 |
| | Joos Press | CTP-1, CTP-2 |
| Stepped lap joint | Induction | STI-1, STI-2 |
| | Joos Press | STP-1, STP-2 |

Before tensile testing, all parts are scanned using a pulse echo C-scan and of each specimen a micrography sample is produced to inspect the interface between the parts. The performance of the repair will be based on the tensile strength and stiffness of the welded specimens. The tensile test will be performed following the ASTM D3039 standard using the recommended specimens dimensions for a balanced and symmetric laminate of 25 by 250 $mm$ [6]. Three specimens of each scarf design will be tested in tension and for each joint type, one additional specimen will be cut, polished, and viewed under the microscope. The resulting tensile strength of these welded specimens will be compared to the pristine strength of uncut specimens and press joined specimens. The press joined specimens will be produced using the Joos Press at TU Delft. This will be explained in more detail in Section 4.5.

This method results in a total of 28 specimens of which 6 will be inspected using micrography and 22 will be tested in tension according to ASTM D3039. The identifications of these specimens are listed in Table 3.3.

Table 3.3: Tensile test specimens

| | | Tensile Testing | Micrography |
|---|---|---|---|
| Pristine | | PR-T1, PR-T2, PR-T3, PR-T4 | - |
| Conventional Scarf | Induction | CVI-T1, CVI-T2, CVI-T3 | CVI-T4 |
| | Joos Press | CVP-T1, CVP-T2, CVP-T3 | CVP-T4 |
| Continuous Scarf | Induction | CTI-T1, CTI-T2, CTI-T3 | CTI-T4 |
| | Joos Press | CTP-T1, CTP-T2, CTP-T3 | CTP-T4 |
| Stepped lap joint | Induction | STI-T1, STI-T2, STI-T3 | STI-T4 |
| | Joos Press | STP-T1, STP-T2, STP-T3 | STP-T4 |

## 3.6. Conclusion

The material, 5HS CF/PPS, is supplied by TenCate in a stacking sequence of $[(0/90)_5]_s$, resulting in a laminate thickness of 3.1-3.11 $mm$. Three different repair joints will be tested that are flush with the surface. A conventional scarf, a continuous scarf, and a stepped lap joint. The scarf joints have an angle of 4.7° and the stepped lap joint has an overlap of 37.8 $mm$.

A single turn coil, with a horizontal section of 40 $mm$ wide and a total length of 800 $mm$, is produced. This coil has a maximum current of 335 $A$ while moving at a frequency of 340 $kHz$. This frequency results in a penetration depth of 8.4 $mm$ and a minimum specimen width of about 50 $mm$ to eliminate the edge effect.

The parts which are to be welded together are milled using a five axis CNC milling machine. Of each joint type, an induction welded and press joined specimens will be produced. Additionally pristine test samples are cut from the supplied panels. These specimens will be compared using tensile tests to determine the stiffness and failure strength of the specimens. Before testing the samples in tension, they are scanned using a C-scan. Furthermore of each joint type a test sample is inspected using micrography.

# 4

# Production

This chapter discusses the production of the specimens and tooling required to produce the specimens. The first section explains the process to create the continuous scarfed parts. In Sections 4.2 to 4.4, the welding station and pressure frame, measurements concerning the interface temperature, and the welding trials are discussed. This chapter is finalized by a section about the press joined specimens.

## 4.1. Continuous Scarf

The continuous scarf is produced using CF/PPS semi-preg, supplied by TenCate, and the Joos Press at the TU Delft. Special tooling is milled from aluminum. This tooling consists of a plate with a 3.1 $mm$ deep cavity, where one of the four sides of the cavity is an exact replica of the conventional scarf geometry. The cavity is 160 $mm$ wide and 150 $mm$ long at the location of the top layer. The lengths of all plies are listed in Table 4.1. Once cut, the plies are placed inside the tooling as shown schematically in Figure 4.1 and ultrasonically spot welded at two corners to prevent the layers from moving during the consolidation cycle.

Table 4.1: Length of the plies placed in the aluminum tooling, from top to bottom

| Ply | length | | Ply | length | |
|---|---|---|---|---|---|
| 1 | 150 | $mm$ | 6 | 135 | $mm$ |
| 2 | 120 | $mm$ | 7 | 139 | $mm$ |
| 3 | 124 | $mm$ | 8 | 143 | $mm$ |
| 4 | 127 | $mm$ | 9 | 146 | $mm$ |
| 5 | 131 | $mm$ | 10 | 120 | $mm$ |

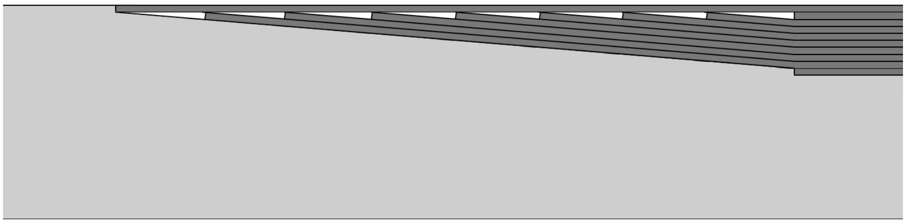

Figure 4.1: Detailed schematic look of the semi-preg lay-up inside the tooling

The consolidation cycle consists of a heating phase at a rate of 6 $°C/min$ to 320$°C$ at a pressure of 2 $bars$. This temperature is maintained for 40 minutes before the pressure is increased to 10 $bars$. After holding at 320$°C$ and 10 $bars$ for 20 minutes, the temperature is decreased to room temperature at a rate of 15 $°C/min$. A graphite plate is placed on top and below the tooling to ensure evenly distributed heat during the heating and the cooling phase. After unloading the parts are cut to 130 $mm$ wide and 140 $mm$ long pieces and marked CTI-2, CTI-2T, and CTP-2. The average thickness, measured at nine points along the un-scarfed edges, of CTI-2 is about 2.95 $mm$ and that of CTP-2 is 2.91 $mm$. The scarf geometry mirrors that of the CNC milled conventional scarf, resulting in good contact without any gaps when placed together. This thickness is less than that of the milled parts of 3.1 $mm$ due to squeeze flow of the resin resulting in a higher fiber content. As shown in Appendix D, the higher fiber content does not result in a different failure force. However, because of the lower thickness, does result in a significantly higher failure stress. Therefore, the failure stress and the stiffness will be normalized using the thickness, resulting in comparable results.

Microscopic pictures of the complete interface of both CTI-2 and CTP-2 can be found in Appendix G.1, where it can be seen that the plies are parallel to the scarf angled at 4.7°. A few details are highlighted in this section. In Figure 4.2, the tip of CTP-2 is shown. It can be seen that the 0° filaments fall about 0.25 $mm$ short of reaching the tip, but that the 90° filaments have distributed themselves to fill the PPS matrix. In Figure 4.3 the initial step of the scarf is shown. The top ply has been cut about 0.5 $mm$ too long, resulting in a pushed down ply and a resin rich area at the location of the step. In the figure, the correct ply position is indicated by the green area, whereas the actual ply position is indicated by the red area.

As seen in Figure 4.4, the layer has been cut about 1.3 $mm$ short resulting in a resin rich area with a few 90° filaments. These small manufacturing defects are not easily avoided and are likely to occur when a patch is produced for a repair. Therefore, it is decided to note the defects and use these parts for welding and tensile testing.

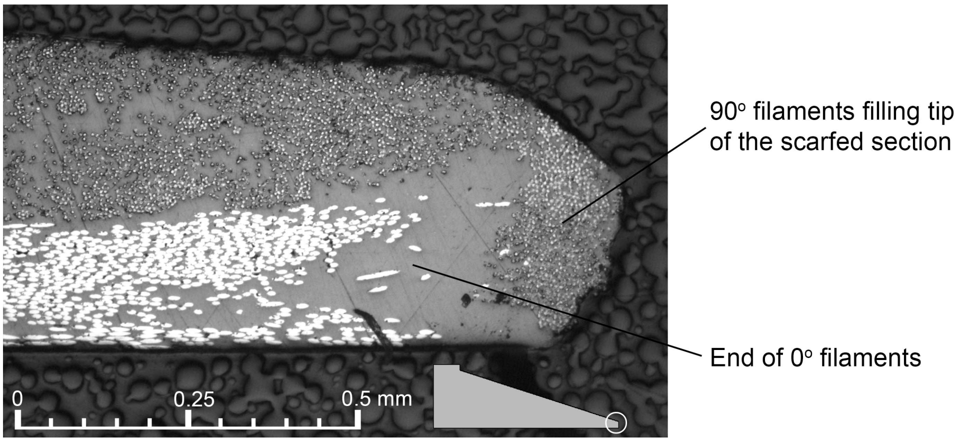

Figure 4.2: Tip of the CTP-2 part. 0° plies are light whereas 90° plies are dark. A schematic overview indication where the microscope picture is positioned with respect to the scarf is shown in the figure. The bottom ply can be seen to be 0.25 $mm$ too short.

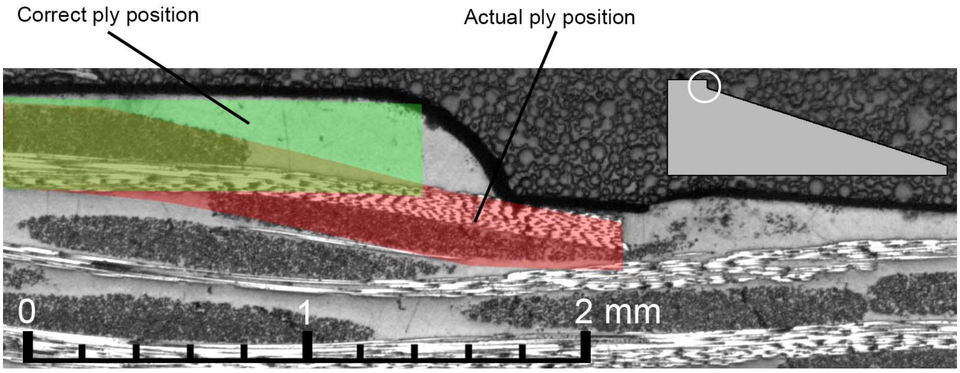

Figure 4.3: Step of the CTP-2 part. 0° plies are light whereas 90° plies are dark. A schematic overview indication where the microscope picture is positioned with respect to the scarf is shown in the figure.

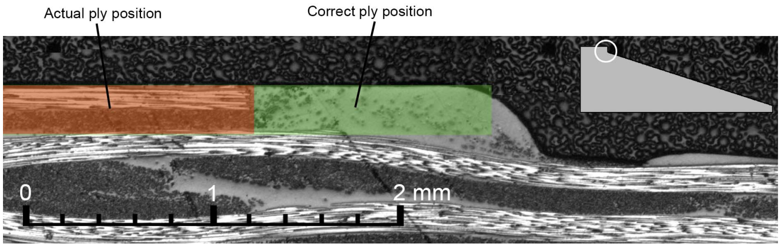

Figure 4.4: Step of the CTI-2 part. 0° plies are light whereas 90° plies are dark. A schematic overview indication where the microscope picture is positioned with respect to the scarf is shown in the figure.

## 4.2. Welding Station

A welding station connected to a linear guide is available at KVE Composites for research and design development. This 2 $kW$ generator has a maximum current output of about 300 to 350 $A$. The welding station is shown in Figure 4.5. The generator is indicated in the figure by 1. The welding head, indicated by 2, is placed on a linear guide which can move for about 600 $mm$ along the guide as indicated by the arrows. Indicated in the figure by 3.1 and 3.2 is the bottom and top of the pressure frame respectively. Both the linear guide and the generator are controlled using a laptop and a programmable logic controller.

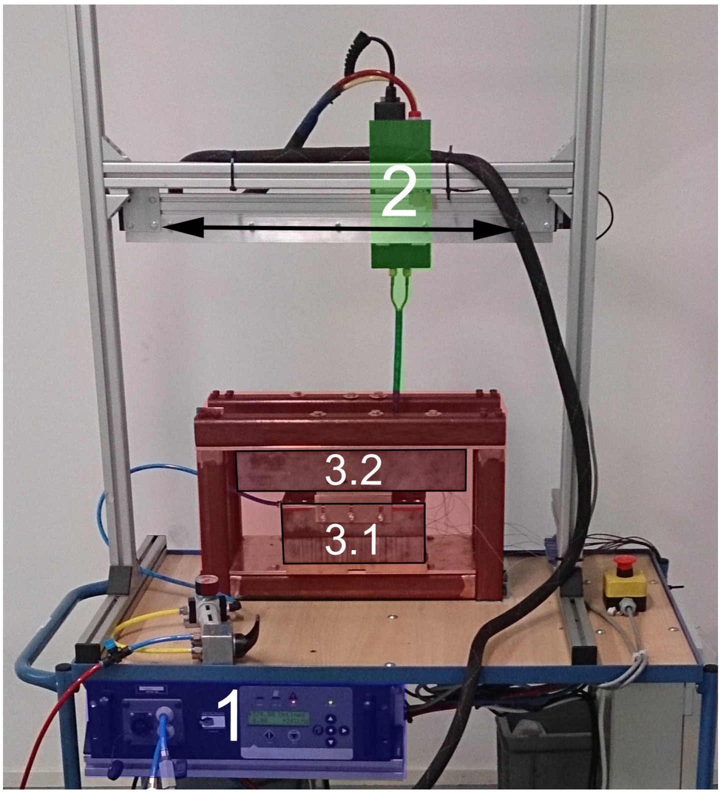

Figure 4.5: Welding station with the generator (1), the welding head on a linear guide (2), Bottom of the pressure frame with silicon balloon (3.1), and the top of the pressure frame (3.2)

The pressure frame in Figure 4.5 is an pre-existing pressure frame available at KVE Composites that has been adapted to support parts of 130 by 250 $mm$. The pressure is applied by an inflatable silicon balloon, with a size of 200 by 130 $mm$, inside a tooling board block. This tooling board block is indicated in Figure 4.5 by 3.1. The cushion pushes the parts up against a tooling board support block, indicated by 3.2 in the figure. This top part of the pressure frame has a 70 $mm$ wide gap in the middle to allow the 64.5 $mm$ wide coil to pass through. Two support plates are added to support the CF/PPS parts at the gap, one plate above and one below the parts. This setup has been shown schematically in Figure 4.6. The support plates have the same dimensions as the CF/PPS parts, 130 by 250 $mm$. With a gap of 70 $mm$ that is bridged, 180 $mm$ of the support plates is clamped against the top pressure frame with 5 $bar$.

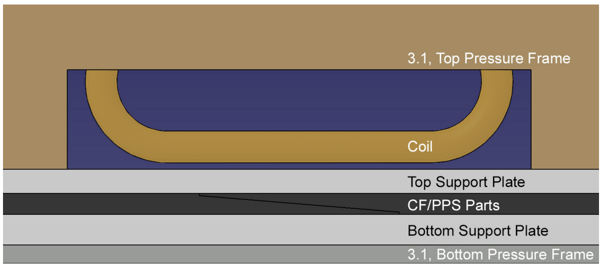

Figure 4.6: Schematic lay-out showing the support plates, parts, and inflatable silicon cushion

The close vicinity of the support plates, the coil, and the weld interface require these plates to be able to resist temperatures well above the processing temperature of 320°$C$ and not heat up because of the alternating magnetic field. Glass Fiber (GF) is a suitable material as it is non magnetic or conductive and thus does not alter the magnetic field created by the coil. Initially epoxy is used, in combination with 3 $mm$ thick silicone sheets to shield the GF/Epoxy plates from the welding temperatures.

The deflection of the support plates due to the applied pressure of 5 $bar$ can be estimated using Equation (4.1), in which $\delta_c$ is the deflection in the middle of the plate in $m$. The boundary conditions of this equation assume that edges of the plates are fixed, which is realistic as the support plates are clamped against the pressure frame with 5 $bars$. As at the welding temperature the CF/PPS will provide no stiffness, any additional stiffness due to the parts being welded is neglected. The stiffness of the GF/epoxy is assumed to be 35 $GPa$. More accurate results would be obtained if the stiffness of the GF/epoxy at higher temperatures is used. However, both the temperature during welding and the stiffness of the GF/epoxy used at higher temperatures is unknown. Equation (4.1) is based on a number of assumptions and calculated at room temperature while the deflection of the support plates at the processing temperature is of main interest. The results will be an indication at best and should be compared to deflection measurements to confirm the accuracy.

$$\delta_c = \frac{qL^4}{384EI} \tag{4.1}$$

This equation is plotted in Figure 4.7 for a support plate thickness of 1 to 10 $mm$ with a step size of 0.5 $mm$. This equation gives a deflection less than 0.1 $mm$ for a plate thickness larger than 4 $mm$. As this equation is based on a number of assumptions, three plates are produced to verify the deflection. 600 $g/m^2$ UD glass fiber is used stacked in 6, 8, and 10 layers to produce plates with an approximate thickness of 3.3, 4.3, and 5.3. $mm$. During pressurization to 5 $bar$, the combination of the 3.3 and 5.3 $mm$ plates shows a slight deflection, whereas the combination of the 4.3 and 5.3 $mm$ plates is barely visible. At this stage, it was neglected to measure the deflection of the support plates to verify Equation (4.1) and the support plates are permanently deformed by performing a high temperature test explained in the next paragraph.

The GF/epoxy support plates are not able to withstand the processing temperatures of 320°. Therefore, a 3 $mm$ thick silicon shielding layer is added between the CF/PPS parts and the support plates. This silicon layer, in combination with the top support plates thickness of 4.3 $mm$ and a coil height of 0.5 $mm$ above the support plate, results in a coupling distance between the CF/PPS laminate and the coil of 7.8 $mm$. A few welding trials are run to investigate whether the GF/epoxy support plates are sufficiently shielded. Low temperature trials are run at 3, 2, 1, and 0.74 $mm/s$ coil velocities giving average top surface temperatures of 99, 111, 156, and 182°$C$ respectively. These results are used to predict a coil velocity of 0.28 $mm/s$, which is needed to obtain an average top temperature of 300°$C$. In Section 4.4 the procedure, thermocouples, and thermocouple locations used to obtain these measurements are explained in more detail.

Two conclusions can be drawn from the these experiments. First of all, the silicone layer does not shield the GF/epoxy support plates and the support plates are permanently deformed resulting in a specimen deflection of about 2.1 $mm$, shown schematically in Figure 4.8. Secondly, the 7.8 $mm$

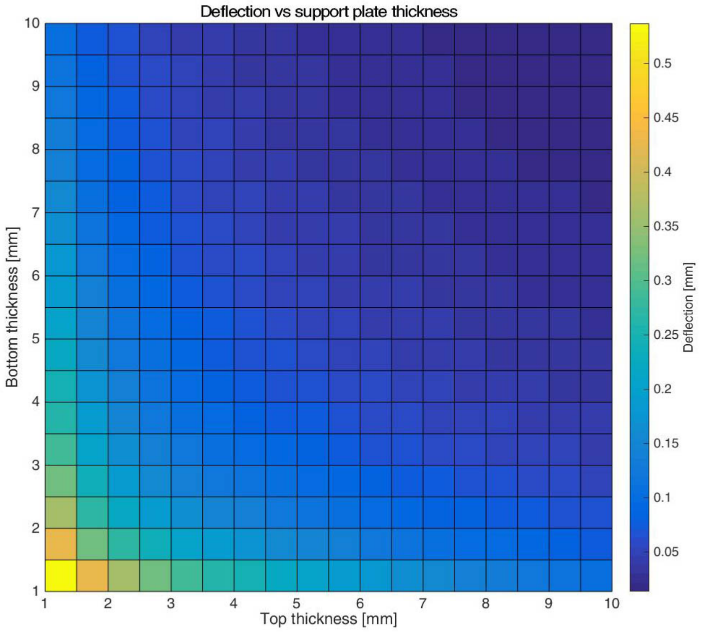

Figure 4.7: Deflection as a function of the top and bottom support plate thickness

coupling distance between the top of the CF/PPS laminate and the coil results in a slow coil velocity of around 0.3 $mm/s$.

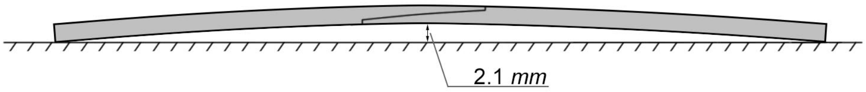

Figure 4.8: Schematic display of the deflection in the middle of the welded specimen

As the silicon layer does not provide sufficient shielding for the epoxy support plates, a different matrix material is needed for the support plates that is able to withstand temperatures to well above the process temperature of 320$^\circ C$. A small batch of Lonza PT-30® cyanate ester is available at KVE composites, which, if given the correct post-curing cycle, has a $T_g$ higher than 400$^\circ C$ [72]. The curing cycle for this material and plate thickness is determined in consultation with Lonza. This cure and post-cure cycle is shown in fig. 4.9. The resin is infused at 100$^\circ C$ to obtain a viscosity of around 400 $mPa \cdot s$.

Using this cure and post-cure cycle, two plates with 8 and 10 layers of 600 $g/m^2$ are produced. The infusion is performed in the oven, opening the door on several occasions to monitor the progress, resulting in a decrease in temperature and increase in viscosity of the resin. Lacking a programmable oven, the heating rate is obtained by manually increasing the target temperature of the oven while monitoring the temperature of the laminate using a thermocouple.

The resulting plates have thicknesses of 3.6 and 4.6 $mm$ and a lower surface quality than desired. The support plates, shown in Figure 4.10, have small grooves in between the yarns that are caused by a lower infusion viscosity than required. When 5 $bar$ of pressure is applied to CF/PPS parts and support plates placed in the pressure frame as shown in Figure 4.6, a deflection of 0.23 $mm$ is measured in the middle of the 70 $mm$ wide bridged section. Using Equation (4.1), and an assumed stiffness of 35 $GPa$, the predicted deflection is 0.24 $mm$. This prediction is remarkably close, taking into account the assumptions made. This deflection is higher than desired. However, as mentioned before, the stiffness of the support material is unknown at the process temperature, resulting in an estimated deflection at best. On top of that, the batch of PT-30 available at KVE had been exhausted and restocking would result in a significant delay in the project. Therefore, it is decided to continue with the 3.6 and 4.6 $mm$ thick plates and note the deflection of the welding specimens.

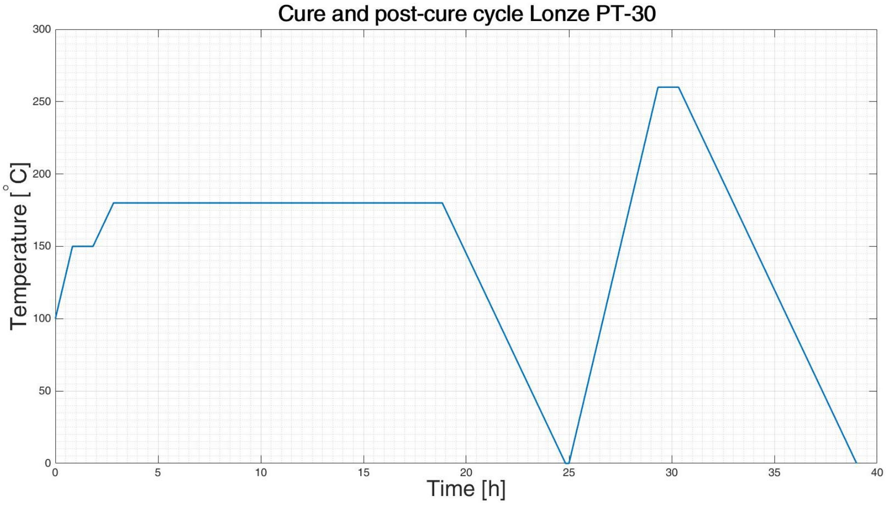

Figure 4.9: Cure and post-cure cycle of the Lonza PT-30 Resin

Figure 4.10: Surface of the cyanate ester support plates, grooves visible between UD yarns

## 4.3. Interface Temperature

The interface between the two parts can only be measured when a temperature sensor is placed in between the parts. Thermo-electra T05-02-E thermocouples are used. These thermocouples are twisted, isolated with extruded Fluorinated Ethylene Propylene (FEP), and have a wire diameter of 0.2 $mm$. The FEP has a maximum operating temperature of 215$°C$ which is lower than the processing temperature of the PPS. Therefore, the thermocouple wires are untwisted for a length of about 80 $mm$, stripped from the FEP, and shielded again with a polyimide tape. An added benefit is that the thickness of the thermocouples is reduced to the wire diameter thickness of 0.2 $mm$.

A simple experiment is performed to investigate whether poor contact between the parts results in a different temperature. First, an experiment is run without any material between the CF/PPS parts and three thermocouples placed along the weld-line. Then, a second experiment is run with polyimide tape placed in between the CF/PPS parts to prevent any flow of electricity between the parts. The resulting temperatures, shown in Appendix E, show that there is a significant difference between the temperatures when the contact between the parts is isolated.

Two grooves are cut on the interface of one of the test parts in an attempt to measure the interface temperature with a minimal impact on the flow of electricity. The 1 $mm$ wide and 0.6 $mm$ deep grooves, and the thermocouple locations used for the comparison are shown in Figure 4.11. For the stepped lap joints no grooves are cut. Instead, the parts are placed at an offset and thermocouples are inserted in between the parts as shown in Figure 4.12. The temperatures, including the interface temperatures, are measured using this setup and compared to the temperature of parts without grooves for the scarfed parts and without an offset for the stepped lap parts. At least three tests are run per variation with a power of 310 $A$, coil velocity of 8 $mm/s$, and a coupling distance of 4.1 $mm$ between the coil and the top surface of the laminate.

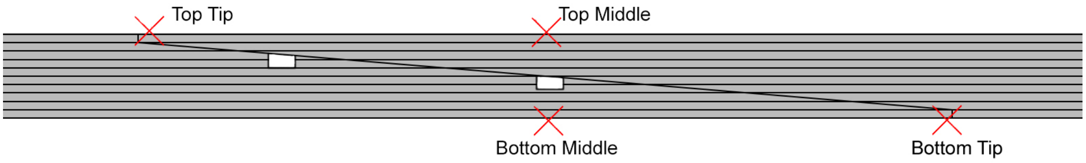

Figure 4.11: The grooves and the thermocouple locations for the interface comparison tests of the scarfed specimens

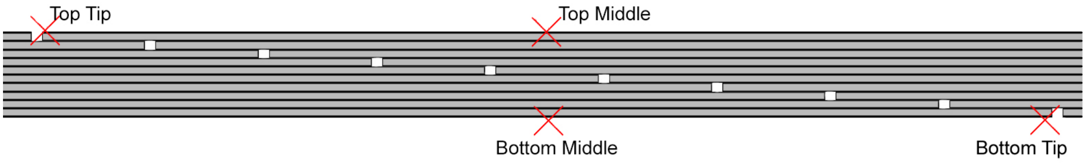

Figure 4.12: Thermocouple locations for the interface comparison tests of the stepped lap specimens

The results of these tests are compared using a z-test, which is a test that determines the probability that two datasets are statistically similar. In general, it is accepted that when the resulting probability is higher than 5%, the datasets are similar. The results of the z-test showed that for at least three out of four thermocouples, the temperatures are significantly different when comparing the joints with and without interface measurements. It is therefore concluded that any temperature sensor placed in between or inside the parts significantly alters the measured temperatures. This is likely caused by altering the flow of the electric currents inside or in between the parts. The resulting probabilities are shown in Appendix E.

## 4.4. Induction Welding

In the first section, the method used to obtain the welding programs is discussed. In the next section the welding of the CVI, STI, and CTI specimens is presented.

### 4.4.1. Welding Trials

The maximum current output, as determined in Section 3.3, is higher than the actual current that can be used during welding due to influence of the pressure frame. The maximum current that can be used during welding is determined by an experiment at a welding speed of 5 $mm/s$, as to not overheat the laminate. This shows that a maximum current of 310 $A$ can be applied which operates at a frequency of 340 $kHz$.

Next, the temperature distribution perpendicular to the weld-line is investigated to determine where the thermocouples should be placed to measure the temperature distribution along the weld-line. Eight thermocouples, the maximum that can be connected to the welding station, are placed on the parts as shown in Figure 4.13. The same thermocouples as described in Section 4.3 are used. Six tests per variation are run at a velocity of 8 $mm/s$ and 310 $A$. These results are plotted in Figures 4.14 to 4.16. Tests at slower coil velocities have also been run and similar distributions are found.

It can be seen that the temperatures are increasing and become inconsistent towards $TC_1$ and $TC_4$, the tips of the scarfed sections. This could be explained by placing resulting in a gap between the two plates. If such a gap is present at the tip the current flow would be interrupted locally, essentially creating an edge effect which could increase the temperature. The thermocouples directly underneath the coil, $TC_3$ on the top surface and $TC_6$ on the bottom surface, are consistent. Additionally, for each joint type the temperature at the top surface is approximately equal to the temperature at the bottom surface, measured at $TC_3$ and $TC_6$. Therefore, it is decided to place the thermocouples to determine the distribution along the weld-line at the top surface at the location of $TC_3$.

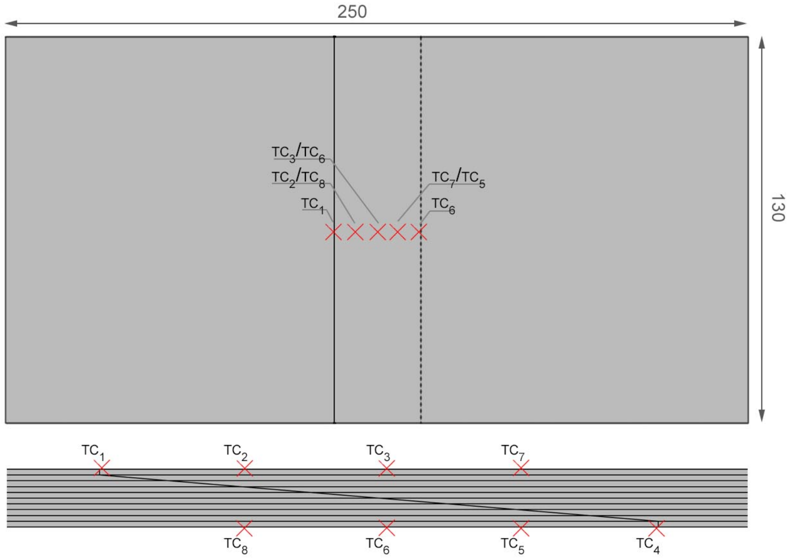

Figure 4.13: Locations of the thermocouples to measure the distribution perpendicular to the weld-line

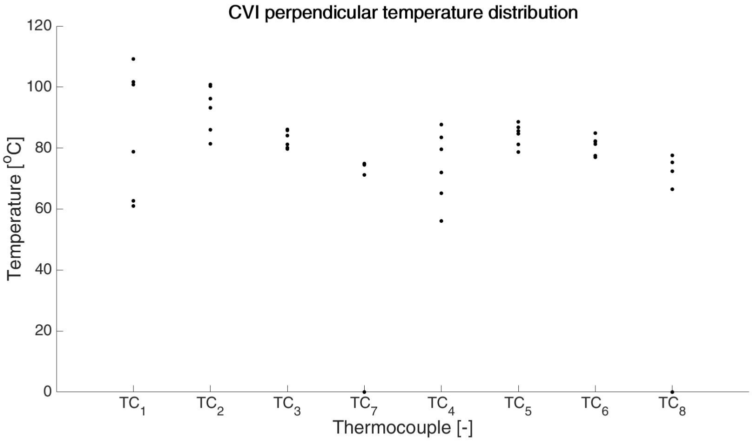

Figure 4.14: Maximum measured temperatures in the CVI specimen with thermocouples placed as indicated in Figure 4.13

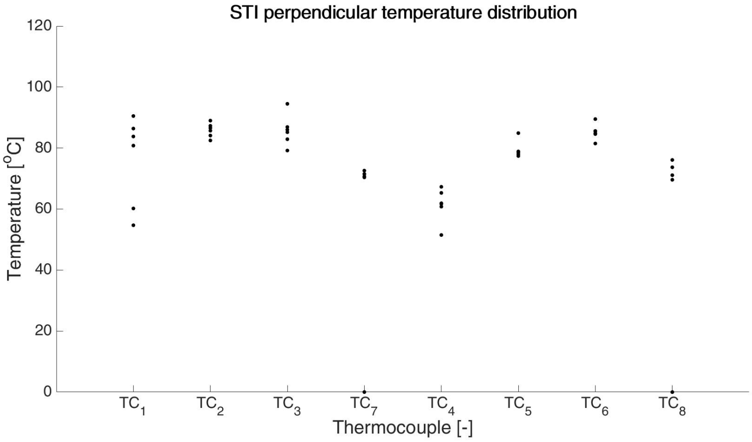

Figure 4.15: Maximum measured temperatures in the CTI specimen with thermocouples placed as indicated in Figure 4.13

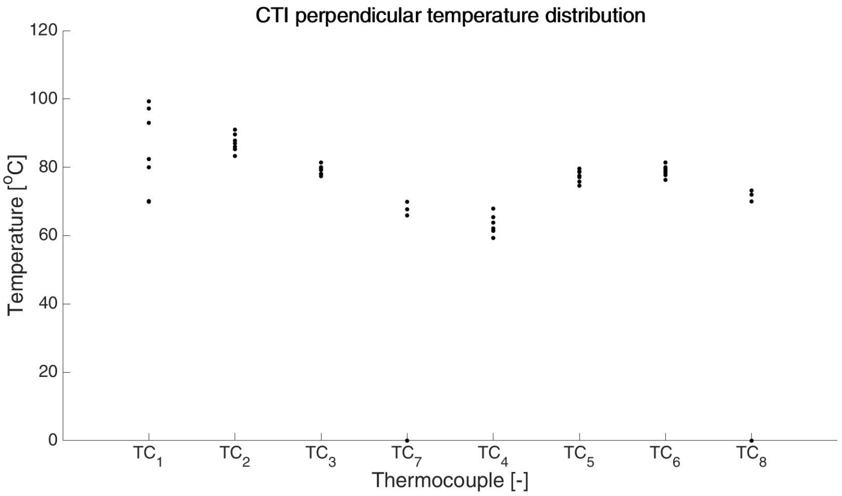

Figure 4.16: Maximum measured temperatures in the STI specimen with thermocouples placed as indicated in Figure 4.13

For a consistent weld-quality an uniform temperature distribution along the weld-line is desired. To entirely join the parts, the complete interface in between the parts needs to reach at least 280 $°C$. The CF/PPS parts should not experience a temperature higher than 400$°C$, at which temperature the degradation of PPS initiates [73–76]. Taking into account a margin of safety, as the temperatures inside the interface are not known, the temperatures measured along the weld-line should remain within 310-370$°C$ for a proper weld.

To predict the temperature distribution along the weld-line, seven thermocouples are placed as indicated in Figure 4.17 and 27 experiments are run at 310 $A$. Three runs, for the three joint types, for three different welding speeds of 12, 8, and 6 $mm/s$. One of these temperature profiles, run at 310 $A$ and 8 $mm/s$, is shown in Figure 4.18. It can be seen that the thermocouples do not reach their highest temperatures when the coil is directly above the thermocouple, but rather after a small delay. This is caused by a the heating pattern generated by the coil that is wider than the coil itself. Therefore, a thermocouple is heated before the coil is positioned directly above its exact position and will still be heated when the coil has passed over the thermocouple.

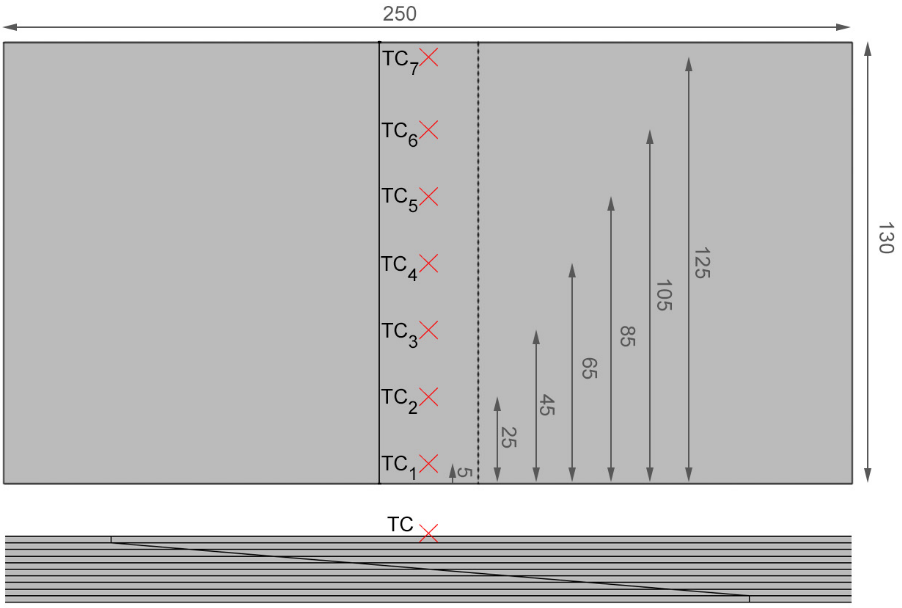

Figure 4.17: Locations of the thermocouples to measure the distribution along the weld-line, all dimensions are in $mm$

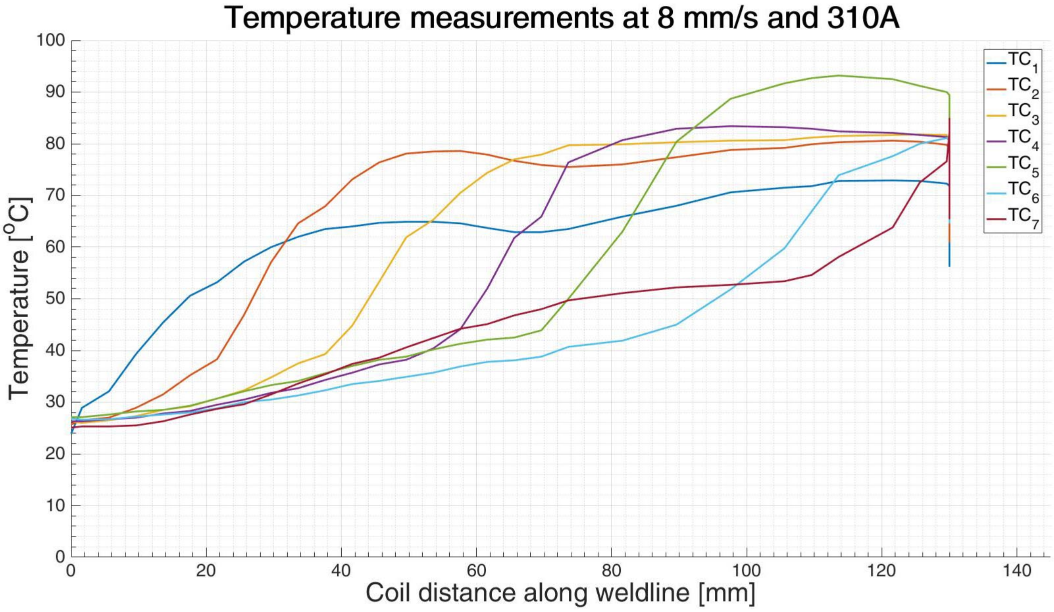

Figure 4.18: Temperature distribution with thermocouples placed as shown in Figure 4.17

Also, each thermocouples, except for $TC_1$, experiences a certain pre-heating before the coil passes over a thermocouple. The last thermocouple, placed at 125 $mm$, already heats up when the coil is at about 15 $mm$ from the start of the specimen. This can be attributed to the conductivity of CF. This interaction results in higher temperatures in $TC_4$ and $TC_5$, whereas $TC_6$ and $TC_7$ lack the additional heating after the coil has passed to reach the higher temperatures. Finally, it can be seen that $TC_7$ heats up about 10$°C$ after the coil has been turned off, which is again attributed to the conductivity in the CF although a delay in the data logger system may also have contributed slightly.

For the first two thermocouples, the highest temperature is reached with a larger delay. As seen in the graph, the thermocouples cool down before a second stage of heating is seen. Both thermocouples reach their highest temperature when the coil is almost at the end of the parts. This cannot be attributed to conductivity within the part, as this would result in steady heating instead of a cooling down phase. Additionally, if conduction was the source of this second heating phase, $TC_2$ would initiate the heating phase before $TC_1$ starts to heat up again. As can be seen in the graph, $TC_1$ starts its second heating phase around 65 $mm$, whereas $TC_2$ initiates its second heating phase around 75 $mm$, indicating that the second heating stage initiates at the edge.

It is investigated whether the edge effect could explain this second heating phase. Two simulations on a 130 by 250 $mm$ pristine specimen, which is validated, are run to investigate this possibility. Although the scarfed specimen will likely behave different than the pristine specimens, these simulations give an indication to what extend the edge effect may play a role. In the first simulation, the coil is placed at the center of the laminate. In the second simulation, the coil is placed at 100 $mm$ from the left edge and 30 $mm$ from the right edge. As can be seen in Figure 4.19, both edges experience a higher current density, even when the coil has almost reached the opposite edge. However, for the thermocouples to experience a cooling phase, the current densities at the edge need to decrease first, before increasing again when the coil moves further away from the edge. Although there is an area in between the coil and the edge that experiences a lower current density, it can also be seen that this area almost disappears when the coil approaches the edge. As such the cooling phase seen in $TC_1$ and $TC_2$ cannot be explained by the higher current densities. Further research is required to fully understand this cooling and heating phase. However, as will be shown in the following paragraphs, the second heating phase becomes a smaller issues at lower welding speeds.

As mentioned before, 27 tests are run. Three for each of the three joint types at three different welding velocities, being 12, 8, and 6 $mm/s$ logging seven thermocouples along the top surface as shown in Figure 4.17. It has been found that a power function is a good representation of the welding temperature as a function of coil speed. To predict the needed coil speed, power curves are fitted to two temperatures. The maximum measured temperatures during the welding cycle, $T_{max}$, and the average

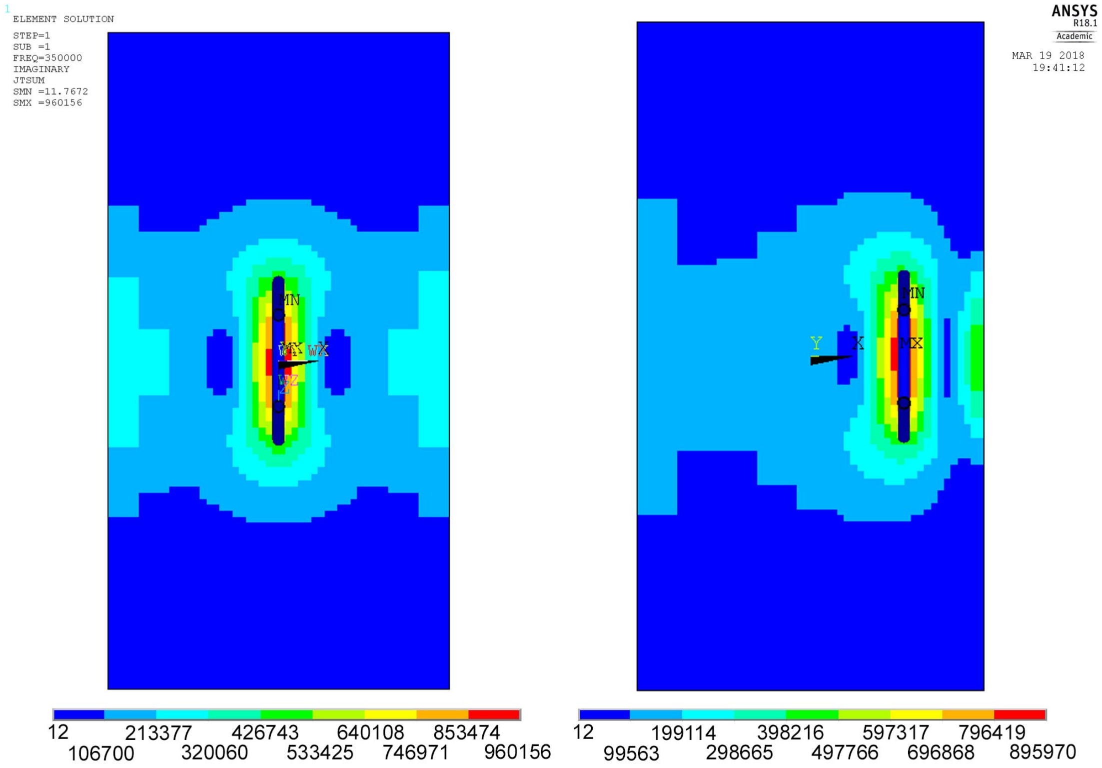

Figure 4.19: Simulate current densities for a 130 by 250 $mm$ specimen with a coil placed in the center of the specimen (left) and at 100 $mm$ from the initial edge (right)

of the seven maximum temperatures measured along the weld-line, $T_{avg}$.

For the conventional scarfed parts these power functions are used to predict the temperature for a coil velocity of 3 $mm/s$. The predicted results, a $T_{avg}$ of $132.1^{\circ}C$ and a $T_{max}$ of $155.0^{\circ}C$, are close to the measured temperatures, $T_{avg}$ being $133.5^{\circ}C$ and $T_{max}$ being $153.4^{\circ}C$ on average for two runs. The power function used for this prediction are shown in Figure 4.20. These two runs are used to update the power functions.

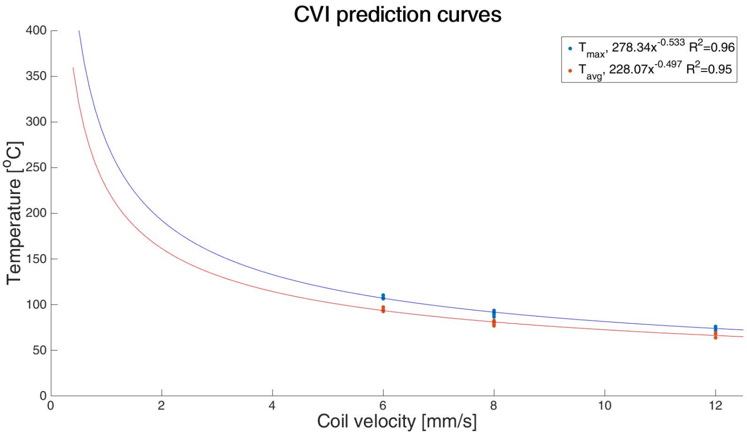

Figure 4.20: Prediction of the maximum and average temperature as a function of coil velocity for the CVI parts

To obtain an average temperature of $320^{\circ}C$, the suggested processing temperature, a coil speed of 0.53 $mm/s$ would be required. At this welding velocity a maximum temperature of $383^{\circ}C$ is predicted, which is close to the degradation onset of $400^{\circ}C$ of PPS. As this is a trial run, the target for $T_{avg}$ will be $300^{\circ}C$ which requires a coil velocity of 0.6 $mm/s$ and results in a predicted $T_{max}$ of $358^{\circ}C$.

Before any parts are welded together, they are first dried in an oven at 120°$C$ for 10 hours to evaporate any moisture the parts might have absorbed and to reduce the risk of voids in the laminate. The resulting temperature profile can be seen in Figure 4.21, where the thermocouples are again located as indicated in Figure 4.17. The maximum temperature reached is 308.1°$C$. The average of the maximum temperatures of each coil, $T_{avg}$, is 270 °$C$. Both of these values are significantly lower than predicted.

Unlike the temperature profile in Figure 4.18, the maximum temperatures are increasing consistently. Similar to the low temperature test, the thermocouples reach their highest temperature when the coil has moved 10 $mm$ past the location of the thermocouple. The first and last thermocouple do not follow this pattern. The first thermocouple reaches its highest temperature when the coil is 95 $mm$ into the weld-line. The last thermocouple does not reach the same temperature as the previous thermocouple as the power is turned off before the coil moves 10 $mm$ past the thermocouple.

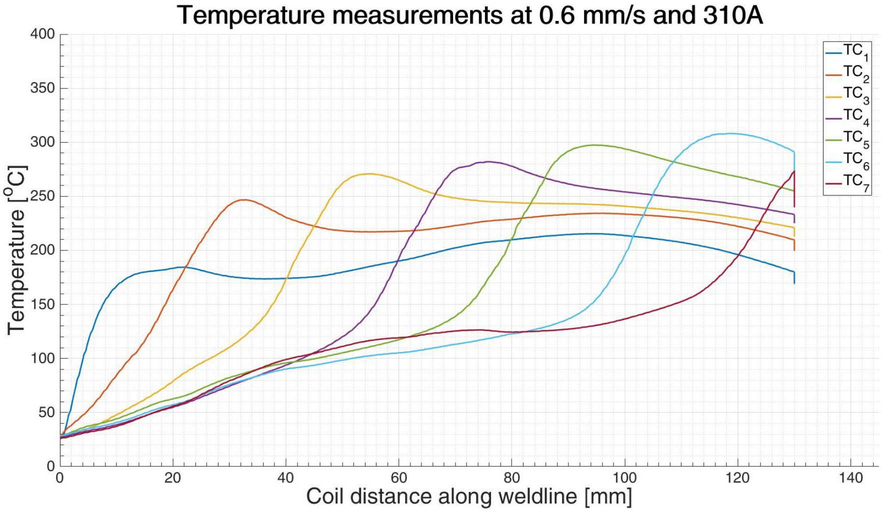

Figure 4.21: Temperature distribution with thermocouples placed as shown in Figure 4.17

To obtain an uniform temperature distribution along the weld line, three tools can be used. Preheating of the laminate before the coil starts moving, adjusting the power input or coils velocity during welding, and post-heating the laminate after the coil stops moving. As initial estimate the coil speed is set to 0.4 $mm/s$, which would result in an average temperature of 338°$C$ when no additional changes are made. Based on low temperature tests the first two thermocouples will experience an increase in temperature due to the pre-heating discussed later on and only the last thermocouple will be affected by post-heating. As such, the temperature of the 4$^{th}$, 5$^{th}$, and 6$^{th}$ thermocouple should be decreased to obtain an uniform temperature distribution. To achieve this, the power is decreased from 310 $A$ to 290 $A$ at 60 $mm$. At this location $TC_4$, $TC_5$, and $TC_6$ are still experiencing heating and $TC_2$ and $TC_3$ have reached their highest temperature. At 100 $mm$ from the start the power is lowered again, now to 280 $A$, to reduce the temperature of the 6$^{th}$ thermocouple and at 125 $mm$ the power is restored to 310A to assist in the post-heating.

Based on low temperature tests, a heating rate of about 3 $deg/s$ is assumed for pre-heating. The predicted temperature for $TC_1$ is about 240°$C$ needing a temperature increase of 90°$C$ or 30 $s$ of preheating duration. The temperature of $TC_7$ cannot be predicted due to the changes to the power program, although it is expected post-heating is necessary. Initially the post-heating is set to 10 $s$.

The resulting temperatures are shown in Figure 4.22 and the welded specimen is shown in Figure 4.23. It can be seen that the welding width behaves similarly to the measured temperatures. Furthermore, only at $TC_5$, with a measured temperature of 335 °$C$, the complete interface is joined. It is also clear that the pre-heat duration is not sufficient to join the start of the weld-line. To join the complete interface along the weld-line, the pre-heat duration needs to be increased and the coil velocity needs to be decreased to increase the overall temperature. It is also interesting to note that due to pre-heating, the peak temperatures of the first thermocouple are almost the same, whereas without pre-heating the temperature at the second peak is higher. Moreover, in subsequent trials the pre-heat time is increased and the first peak, about 10 $mm$ after the coil has passed the thermocouple, is observed to be the highest temperature for $TC_1$.

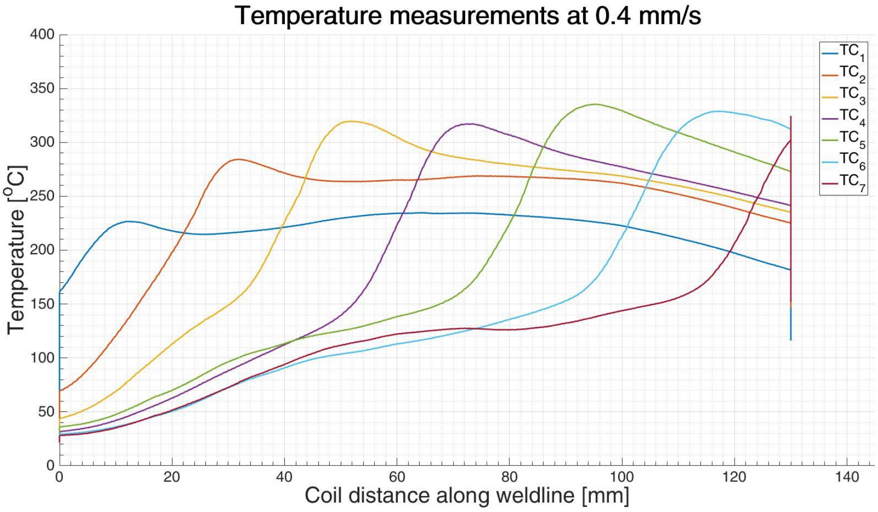

Figure 4.22: Temperature distribution with thermocouples placed as shown in Figure 4.17

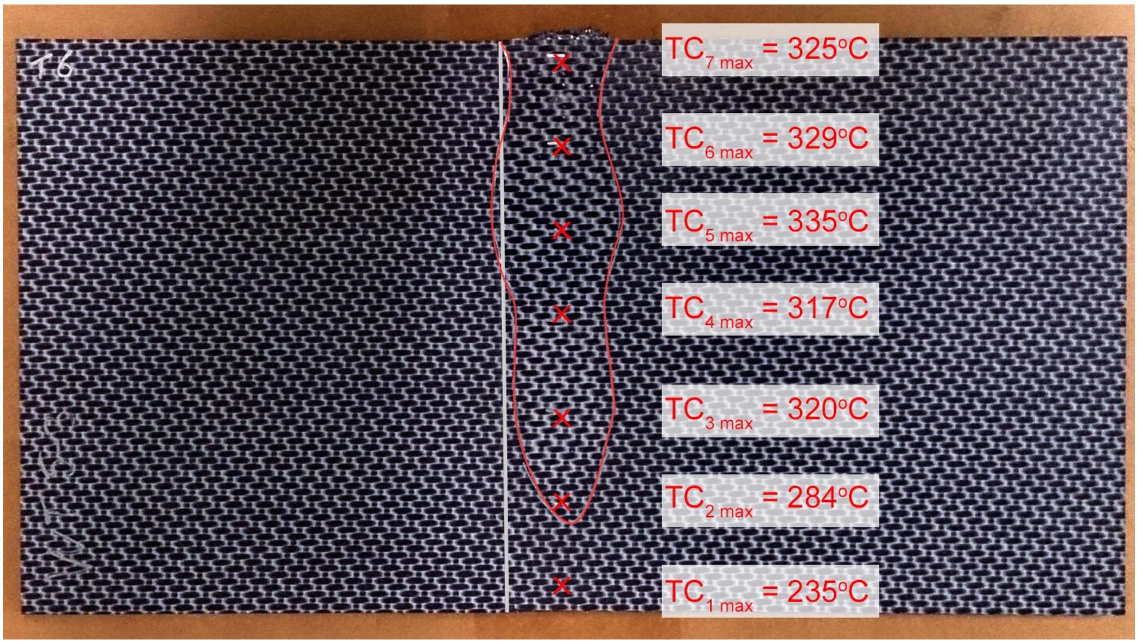

Figure 4.23: Area that has experienced temperatures above $T_m$ at the bottom of the specimen (red encircled area), run at 0.4 $mm/s$ and 310/290/280 $A$

### 4.4.2. Welding of the Mechanical Testing Specimens

After several iterations, the final welding programs for the CVI, CTI, and STI specimens are set. The exact temperatures during welding cannot be determined as thermocouples placed on the parts during welding will leave a significant imprint. To approximate the temperatures achieved during welding, three IR pictures of the top support plate are made during welding. One as the coil starts moving, one when the coil is in the middle of the specimen, and one when the coil stops moving. These IR temperatures are fitted to $TC_1$, $TC_3$, and $TC_6$ respectively, the results of this are shown in Figure 4.24 and using these equations the temperature during welding is estimated.

The welding trials showed that the overlap of the STI specimen is too wide to be joined in a single run using the produced coil. To completely join the interface, a wider coil or multiple weld cycles are needed. As a wider coil requires a new coil and tooling, the parts are welded twice with, both with the coil placed at an offset to the center of the part. This offset is shown schematically in Figures 4.25 and 4.26 and after a few iterations it is found that an offset of 10 $mm$ is sufficient to weld the complete interface. Two different welding programs are constructed for the two different coil offsets. The welding programs, as well as the approximate temperatures during welding, are shown in Table 4.2.

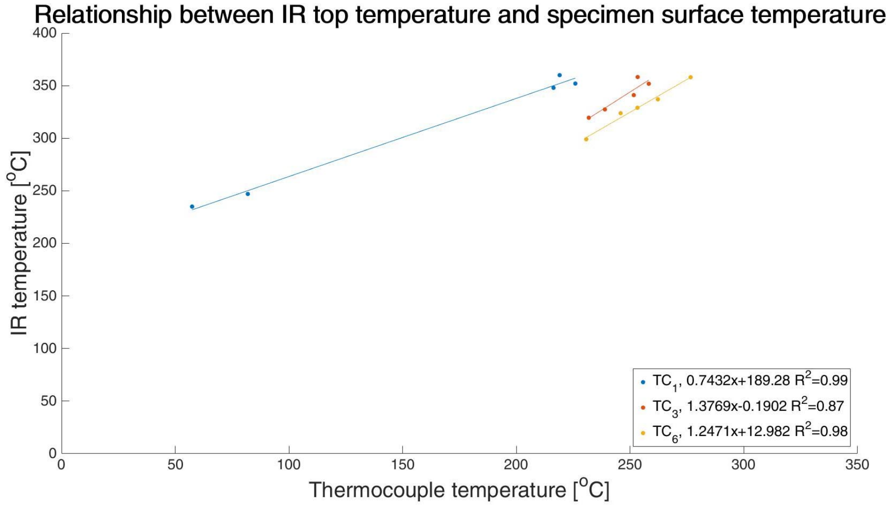

Figure 4.24: Relationship between the IR measured temperature of the support plate and the thermocouple measured temperature of the specimen surface

Table 4.2: CVI welding program and temperatures during welding

| Specimen | CVI | CTI | STI-W1 | STI-W2 | |
|---|---|---|---|---|---|
| Coil velocity | 0.37 | 0.37 | 0.42 | 0.40 | $[mm/s]$ |
| Pre-heat duration | 170 | 180 | 150 | 120 | $[s]$ |
| Post-heat duration | 15 | 15 | 10 | 5 | $[s]$ |
| $\mathrm{I}_{0-65mm}$ | 310 | 310 | 310 | 285 | $[A]$ |
| $\mathrm{I}_{65-125mm}$ | 265 | 285 | 285 | 270 | $[A]$ |
| $\mathrm{I}_{125-130mm}$ | 310 | 310 | 310 | 285 | $[A]$ |
| $TC_1$ | 380 | 350 | 370 | 347 | $[^\circ C]$ |
| $TC_3$ | 385 | 373 | 359 | 330 | $[^\circ C]$ |
| $TC_6$ | 324 | 345 | 347 | 314 | $[^\circ C]$ |

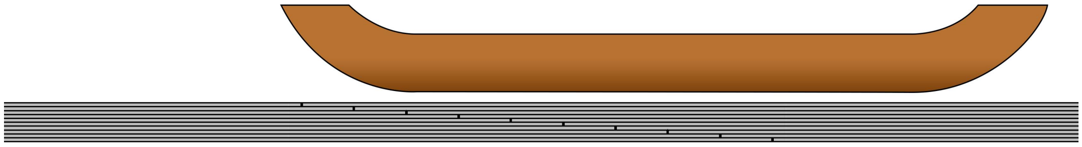

Figure 4.25: First position of the coil used to weld the STI specimen

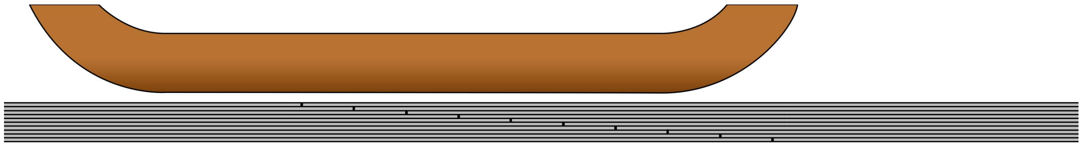

Figure 4.26: Second position of the coil used to weld the STI specimen

The temperatures during welding of the CVI specimen are higher than expected and desired. A trial run, with a pre-heating duration of 180 $s$, post-heating duration of 30 $s$, and a reduced current of 270 $A$ between 75 and 125 $mm$ resulted in IR predicted temperatures of 357°$C$, 355°$C$, and 358°$C$ for $TC_1$, $TC_3$, and $TC_6$ respectively. The final program has reduced current settings and shorter pre- and post-heating durations as to obtain a slightly lower temperature. However, it can be seen in Table 4.2 that the temperature distribution is less uniform and significantly higher than the temperatures measured during the welding trials.

Two distinct difference can be noted between the welding trials and the final weld that could influence the higher welding temperatures. First of all, there are no thermocouples placed on the top surface of the parts, which reduces the coupling distance between the laminate and the coil by few tenths of a millimeter. Although this reduced distance could explain the temperature increase, a similar increase is not seen in the CT and ST specimen. Secondly, there is a difference in the surface quality of the welding specimens. The specimens for the welding trials are milled on a 3 axial CNC using a ball nose end mill which is stepped down to create an angled surface due to logistical difficulties. This is in contrast to the tensile test specimens which are milled on a 5 axial CNC machine with a flat end mill placed at an angle of 4.7°. The resulting surfaces can be seen in Figure 4.27. The surface quality of the 5 axial CNC machine is significantly rougher than the 3 axial parts. As discussed in Section 4.3, the contact between the parts can significantly alter the temperatures in the parts. It is expected that the difference in surface quality is the root of the higher temperatures in the CVI specimen. There are no similar tests to investigate whether this behavior also occurs during the welding of the CTI specimen.

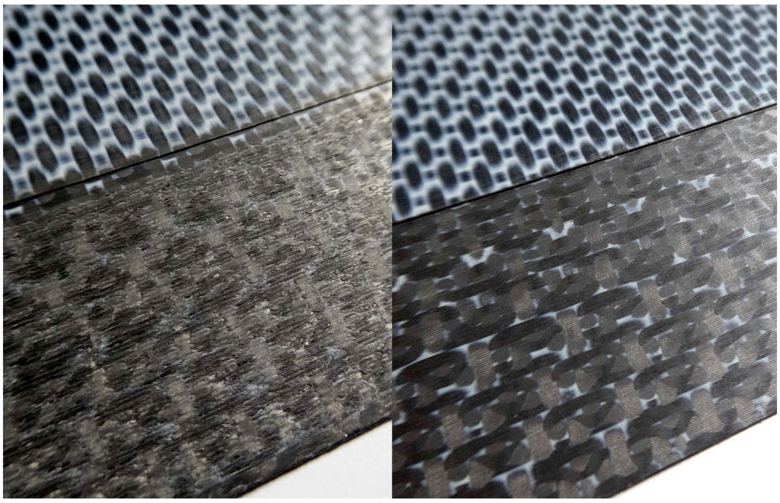

Figure 4.27: Surface comparison between two different CNC machines, five axis CNC(left) and a three axis CNC (right)

Although the temperatures during welding of the CTI specimen are sufficiently high and only slightly less than the temperatures of the CVI specimen, a slight unjoined area is visible both on the top and the bottom of the interface. This indicates that the temperature distribution for the CTI specimen does not result in an even temperature distribution along the interface in between the parts. The extent of non-joined section in the STI and CTI parts will be examined in Section 5.2.

The STI specimen has been joined completely along the bottom, and mostly joined at the top. The extent of the unjoined area will be inspected using micrography. There are two possible explanations for this unjoined gap on the top surface. The temperatures during the second weld are slightly lower than the first weld, although these lower temperatures by themselves would not have resulted in an incomplete bond. It is suspected that the already joined section of the interface changes the flow of electricity inside the specimen resulting in a different heat distribution during welding. This could draw away heat from the not yet bonded part by allowing an easier path for the electricity to flow. This cannot be confirmed as there are not enough test samples to extend the scope of this thesis.

All induction welded specimens have a curvature after welding with a maximum deflection of about 1 $mm$. This deflection is shown schematically in Figure 4.28. This deflection is significantly more that the deflection of the support plates measured at room temperature, being 0.23 $mm$. This is attributed to the decreased stiffness of the GF/cyanate ester support plates at eleveted temperatures and the complete loss of stiffness of the CF/PPS plates above $T_m$.

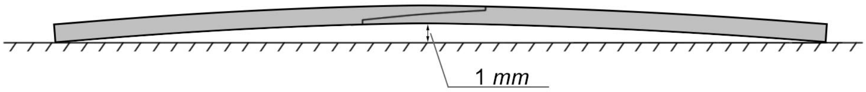

Figure 4.28: Deflection of the tensile test specimens

The support plate, which should not degrade until 420°$C$ is reached, is shown in Figure 4.29. Its surface has clearly been degraded along the weld-line. The highest temperature measured during all of the welding trials has been 389°$C$, which should have been no problem for the cyanate ester. An imprint of the degraded support plates can be seen on the top surface of all the welded parts.

The thermocouples have been verified to give the correct temperature by measuring the temperature of boiling water. Therefore, it is expected that the temperatures during welding have not exceeded the 400°. The cyanate ester used originated from a July 2016 batch which should be within manufacturers specifications when refrigerated during storage. It cannot be guaranteed that the resin has been stored properly, but, according to the manufacturer, improper storage or old resin would result in a lower viscosity without affecting the final material properties.

Figure 4.29: Degradation of the surface of the cyanate ester support plates after welding

## 4.5. Press Joined Specimens

The induction welded specimens will be compared to pristine specimens as well as press joined specimens. This second test series is performed to verify that, even if the pristine strength is not obtained, the induction welded repair is performed correctly. This perfect joint is performed using the Joos Press at the TU Delft and specially designed aluminum tooling.

This tooling consists of a female mold with two removable sides which fits a male mold. Two parts that will be joined are placed inside the female mold with the male mold on top. This is shown schematically in Figure 4.30. The female mold is milled at a size of 250.2 by 130.2 $mm$ to allow the parts and the male mold of 250 by 130 $mm$ to fit. On top of and below this tooling, graphite plates are placed to ensure an even distribution of heat during heating and cooling. The press is run at 320°$C$ and 10 $bar$, the same program as described in Section 4.1. Before being joined in the press, the parts are dried in an oven at 120°$C$ for 10 hours.

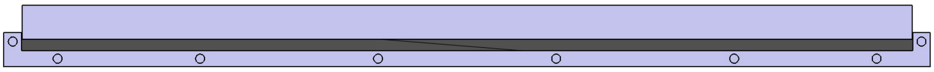

Figure 4.30: Schematic side view of the press join tool with circles indicating the location of the screws used to attach the sides

The produced specimens are measured, the results are listed in Table 4.3. The shown length is an average of two measurements at different locations and the width is the average of three measurements at different locations. The thickness is measured at six different location along the edges of the specimen. The thicknesses of the resulting specimens are significantly smaller than the thicknesses of the supplied plates, which is 3.1 $mm$, due to squeeze-flow during manufacturing. As shown in Appendix D, this does influence the failure stress but does not affect the failure load. Additionally, the amount of squeeze-flow increases with the number of press cycles the tooling has experienced. The CVP specimen has been produced first, the CTP specimen second, and the STP specimen third.

Table 4.3: Tensile test specimens

| | CVP | CTP | STP | |
|---|---|---|---|---|
| $L_{avg}$ | 251,45 | 251,58 | 251,80 | $mm$ |
| $w_{avg}$ | 130,87 | 130,99 | 131,30 | $mm$ |
| $t_{avg}$ | 2.85 | 2.65 | 2.54 | $mm$ |

During the press cycle the aluminum tooling is deformed by the thermal expansion and the applied pressure, which is reversed when the tooling is cooled down and the pressure is released. Consequently, the pressed specimen is compressed lengthwise resulting in a curvature, as shown in Figure 4.31. After unloading the specimen returns to a flat, non-curved state.

The maximum stress experienced by the composite specimen under compression by the female mold is calculated to determine whether the specimens have been damaged during unloading. The maximum stress can be related to the stiffness of the specimen, radius of curvature due to bending, and maximum distance from the neutral axis. This relation is shown in Equation (4.2) and calculated for the CTP specimen. The radius of curvature is obtained using Catia and the resulting tensile and compressive stress are given in Table 4.4. As the specimens are unloaded at elevated temperatures, the elevated material properties are used. At 80°$C$ the stiffness is 56.5 $GPa$, the tensile strength is 730 $MPa$, and the compressive strength is 558 $MPa$ [70]. The ratios are sufficiently low to suggest that the specimens have not been damaged by the tooling.

Figure 4.31: Compressed CTP specimen after consolidation before unloading

$$\sigma_m = \frac{Ey}{R} = \frac{56.5e^9 \cdot \frac{2.65e^{-3}}{2}}{1.01} = 78.2\,MPa \tag{4.2}$$

Table 4.4: Maximum bending stresses

| | CVP | CTP | STP | |
|---|---|---|---|---|
| R | 1030 | 1010 | 960 | $mm$ |
| $t_{avg}$ | 2.85 | 2.65 | 2.54 | $mm$ |
| $\sigma_m$ | 78.2 | 74.1 | 74.7 | $MPa$ |
| ${}^{\sigma_m}/_{\sigma_{x\ ut}}$ | 0.11 | 0.10 | 0.10 | – |
| ${}^{\sigma_m}/_{\sigma_{x\ uc}}$ | 0.14 | 0.13 | 0.13 | – |

## 4.6. Conclusion

Two continuous scarf parts are produced using special tooling. These parts are slightly thinner the thickness of the pristine parts and contain some minor defects in ply location. An existing pressure frame is modified such that the 130 $mm$ wide parts can be pressurized during welding. The support plates need to be non conductive, both in electrical and thermal sense, and non magnetic. GF/epoxy support plates could not be shielded from the high temperatures during welding. Therefore, cyanate ester support plates are manufactured which should have a $T_g$ higher than 400$°C$. These plates result in a deflection of about 0.2 $mm$ when 5 $bars$ of pressure is applied.

During welding there is a flow of electricity between the two parts. Placing thermocouples in between the two parts results in significantly different temperatures during welding. Grooves are cut in an attempt to measure the interface temperature. However, the temperatures measured at the grooved part are significantly different from the temperatures measured at a non-grooved part. Therefore, it is concluded that the temperatures at the interface between the parts cannot be measured without influencing the measured temperatures.

Experiments can provide a prediction of the temperature reached during welding if fitted with a power function, which is accurate for similar welding head velocities. Experiments at a welding head velocity of 12 $mm/s$, 8 $mm/s$, and 6 $mm/s$ provided an accurate prediction for an experiment at 3 $mm/s$. For significantly lower welding speeds, such as 0.6 $mm/s$, the fitted power curves over predict the temperatures. To weld the parts using induction welding, low coil velocities of around 0.4 $mm/s$ are required. A specialized welding program with a pre-heating time, changing current, and post-heating time is required due to thermal conductivity within the specimens.

By visually inspecting the CVI specimen at the top and bottom surface, it is concluded that the parts have been completely joined, whereas the CTI specimen has a slight gap both on the top and bottom surface between the two parts. This gap cannot be explained by the temperatures during welding as the temperatures reached during the welding of the CVI and the CTI sample are comparable. Two runs, with different welding programs, are required to completely join the parts due to the longer overlap of the STI specimen. The resulting STI specimen has a slight gap at the top surface.

The temperatures estimated during the welding of the CVI specimen are higher than expected. This is attributed to the different surface qualities of the tensile testing specimens and the welding trial specimens. During welding of the specimens it also became clear that the cyanate ester support plates are not able to withstand temperatures up to 400 $°C$ and deflect significantly at welding temperatures. This deflection resulted in a deflection of about 1 $mm$ in the induction welded specimens.

The perfectly joint specimens are produced using special tooling using the Joos press. The produced parts are thinner than the original panels which result in higher failure stresses but similar failure loads. To compare the thinner parts the failure stresses will be normalized using their thickness. During unloading, the parts have been compressed by the tooling. However, it is unlikely the compression has resulted in damages to the specimens.

# 5

# Testing

The testing of the specimens consists of a non destructive and a destructive phase. In the first section, the specimens are scanned using a C-scan to reveal major defects inside the specimens. After all specimens have been scanned, they are cut using a Proth cutting machine to ensure a consistent sample width for tensile testing. Of each specimen a microscope sample is cut, polished, and viewed under a microscope in Section 5.2. In Sections 5.3 and 5.4, the results of the tensile tests and the FEM models simulating these tests are presented. Before concluding this chapter in Section 5.6, the results of the tensile tests and FEM analysis are discussed in Section 5.5.

## 5.1. C-scan

Before the tensile test specimens are cut, the welded specimens are scanned using a handheld pulse echo C-scan to reveal any large flaws. The wave velocity through the thickness in the material is calibrated by measuring the time delay in a pristine specimen with a known thickness. This calibration results in a wave velocity of 2840 $m/s$ for the CF/PPS laminate. An OLYMPUS 5L64-A12 transducer is used which has an effective scanning width of 38.4 $mm$. This width is sufficiently large to scan the complete joint interface in one run.

Three gates are set. Gate I is set as entry signal, gate B is placed over the exit signal, and gate A is placed in between the entry and exit signal. Gate A is the main gate of interest, any peaks in the return intensity indicate a flaw in the material. The scans are performed with the specimen and transducer submerged in water to provide a good coupling between the transducer and the specimen.

The press joined specimens reveal no flaws or defects inside the parts. In Figure 5.1, the percentage of the signal that is returned within the A gate of the overlap of the CVP specimen is shown. This scan is performed along the weld-line and, as the joint interface is about 30 $mm$ wide, also includes a small section of the pristine laminate. It can be seen that a negligible amount of the signal is returned within the A-gate and the joint interface cannot be distinguished from the pristine laminate. The scan results for the CTP and STP specimens are similar and can be found in Appendix F.

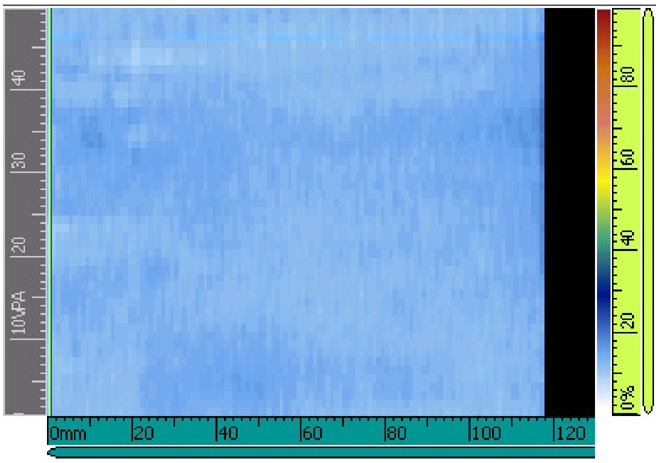

Figure 5.1: Resulting return percentage for the A gate for the overlap of the CVP specimen

The A-gate and B-gate return signals for the CVI specimen are shown in Figure 5.2. C-scan results for all the specimens are shown in Appendix F. In Figure 5.2, it can be seen that for the first half of the specimen a significant amount of the signal is returned within the A-gate, indicating flaws or defects in this area. For the second, half the A-gate shows better results. However, the B-gate, which should return the signal from the bottom of the laminate, barely returns any signal. As the entry signal is visible for the complete scan, the loss of signal for the second half is not due to poor contact between the transducer and the specimen.

As will be shown in Section 5.2, there is a significant amount of voids in the induction welded specimens which could explain part of the signal loss. The top surface of the induction welded parts has mirrored the pattern of the degraded surface of the cyanate ester shown in Figure 4.29. This rough surface finish in combination with the high void content is expected to be the cause of the loss of C-scan signal.

The same pattern can be seen for the continuous scarf and stepped lap specimen. To eliminate the possibility of a scanning or set-up error, the STI specimen is scanned with a through transmission C-scan at the TU Delft. This image, also shown in Appendix F, shows a similar image as the scan made using the pulse echo C-scan. The void content is analyzed in Section 5.2.

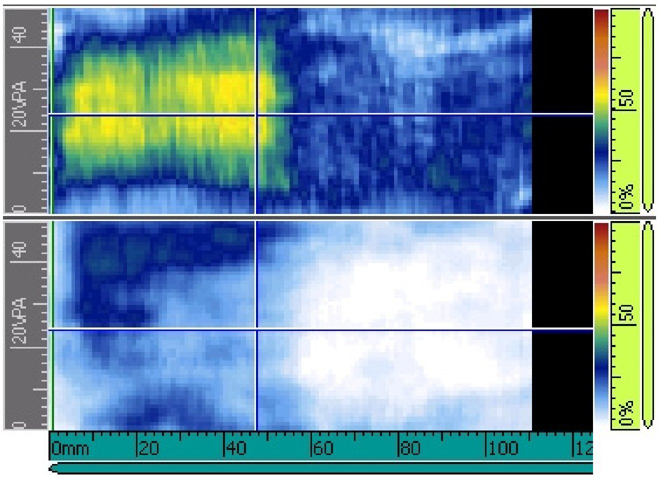

Figure 5.2: Resulting return percentage for the A gate (top) and B gate (bottom) for the overlap of the CVI specimen

## 5.2. Micrography

Out of each specimen, microscope samples are cut. Three samples out of each induction welded specimens, because of the C-scan results that indicate flaws in the joint interface, and one sample per press joined specimen. The three induction welded samples are cut at a spacing of 4-5 $mm$ to investigate the consistency of the samples. To reduce the risk of fiber chipping during grinding, the microscopy samples are cut at an angle with respect tot the 0° fibers. The micrography sample holders have a diameter of 30 $mm$ which allows for samples up to 25 $mm$ to be used. The interface is longer than 25 $mm$. Therefore, each microscopy sample is split into two parts. The cutting angle of the samples is chosen such that the sample is 50 $mm$ long and extends 5 $mm$ past the onset of the interface on either side. This method results in an cutting angle of 53° for the CV and CT samples and 41° for the ST samples.The cutting line of the three induction welded micrography samples is shown in Figure 5.3.

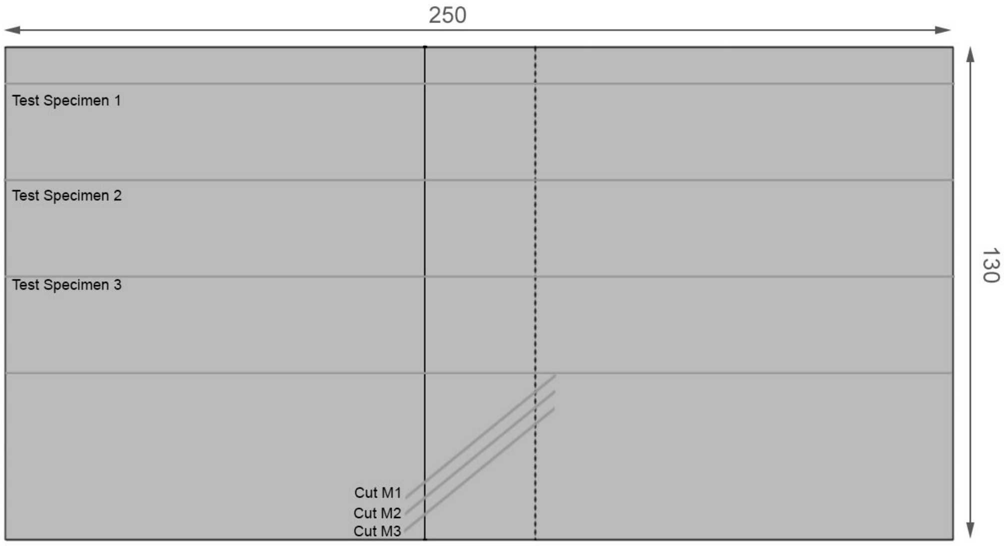

Figure 5.3: Cutting line for the micrography samples

The complete pictures of the samples are given in Appendix G. These pictures are best viewed zoomed in on the original PDF due to their high resolution. A few points of interest are highlighted in this section. Although the press joined samples show no gaps along the interface or any major voids, a few small voids can be found. In Figure 5.4 the initial step of the continuous scarf is shown, which is also shown in Figure 4.3 before joining. In the images taken before joining the parts, it can be seen that the top ply has been pressed down. This top ply repositioned itself to the correct position during press joining of the parts as can be seen in Figure 5.4.

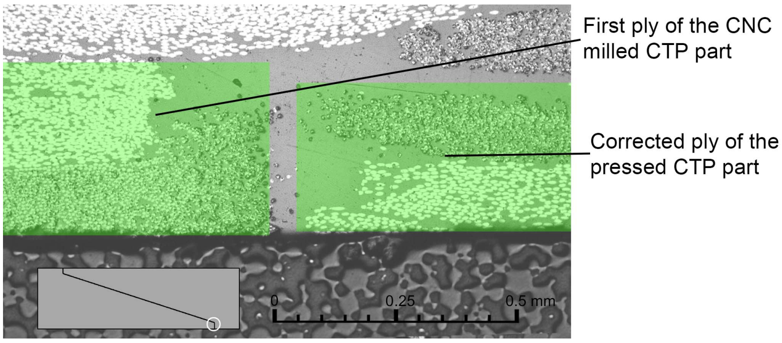

Figure 5.4: The initial step of the CTP parts after joining into the CTP sample. An overview picture to indicate the location of the picture with respect to the interface between the parts is shown.

The induction welded samples show a different picture. In Appendix G, it can be seen that there are a significant number of voids in the induction welded parts. From the micrography pictures, the area of the voids, $A_v$, is obtained by isolating the darker colors. Using Equation (5.1), the void fraction is calculated. The reference area, $A_{ref}$, for all samples is the complete area in between the start and end of the interface. A schematic representation of the voids in the $CVI-M1$ sample and the areas used to calculate the void content are shown in Figure 5.5.

$$V_v = \frac{A_v}{A_{ref} - A_v} \tag{5.1}$$

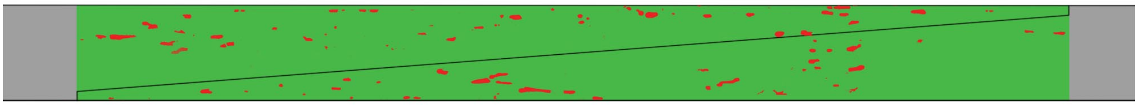

Figure 5.5: Schematic display of the voids in the $CVI - M1$ sample. The reference area (green) and void area (red) used to calculated the void content are indicated in the figure.

The resulting void fractions are listed in Table 5.1. Each specimen has three samples except for the CTI specimen. An mistake was made during the production of the CTI-M3 specimen, such that only half of the interface can be seen. Therefore, this sample cannot be not used. It can be seen that the void content increases from sample M3 to M1, only slightly for the STI samples and more for the CVI and CTI samples. As can be seen in Figure 5.3, this indicates an increased void content towards the middle of the specimen. This can be linked to the temperatures during welding. Where the STI specimen experienced a fairly consistent temperature during welding, the CVI and CTI specimens obtained a higher temperature in the middle of the specimen.

Table 5.1: Void content based on micrography images

| Sample ID | $V_v$ | Sample ID | $V_v$ | Sample ID | $V_v$ |
|---|---|---|---|---|---|
| $CVI - M1$ | 2.88% | $CTI - M1$ | 1.45% | $STI - M1$ | 2.04% |
| $CVI - M2$ | 2.42% | $CTI - M2$ | 0.76% | $STI - M2$ | 1.69% |
| $CVI - M3$ | 1.75% | | | $STI - M3$ | 1.54% |

Although the void content can have a significant influence on the fatigue life and Inter Laminar Shear Strength (ILSS), it is expected that the failure strength of the induction welded samples is not influenced. The main reasoning behind this conclusion is that most voids are located away from the weld-line and none are placed at the initial step of the joint, which is expected to induce the failure in the welded samples.

There are multiple possible causes for these voids such as moisture in the laminate, air trapped between the parts, degradation of the PPS, and insufficient pressure. The parts are dried ten hours at 120°$C$ before welding which eliminates the moisture in the laminate. If air trapped in between the parts would have been the cause, the voids would be concentrated around the interface in between the parts and similar show less variation between the different microscopy samples. The degradation of PPS initiates around 400°$C$ and results in $H_2S$ gas to be created. Although this could explain the voids, no temperatures higher than 389°$C$ have been measured. These voids are likely due to insufficient pressure during welding. The applied pressure of 5 $bar$ is close to the critical pressure of 4.9 $bar$. Any reduction of pressure would have induced the voids in the induction welded samples.

It should be noted that a normal consolidated laminate can have a void content of 1-2% which is too small to be visible on these micrography images. The void fractions shown in Table 5.1 cannot be compared directly to void fractions obtained using standard void determination methods such as ASTM D2734.

In Figure 5.6, the interface in between the CNC milled part (top) and the pressed CTI part (bottom) is shown. The parts have not been joined properly resulting in a gap in between the parts, indicated by the red area. It can be seen that the CNC milled parts has whole and chipped fibers along the interface, whereas the pressed part only has complete fibers along the interface. It should also be noted that a thin layer of PPS is found between the fibers and the interface at the pressed part. This thin layer of PPS could result in a reduced flow of electricity between the two parts. And could result in an incomplete joint. No additional PPS film has been added to the joints.

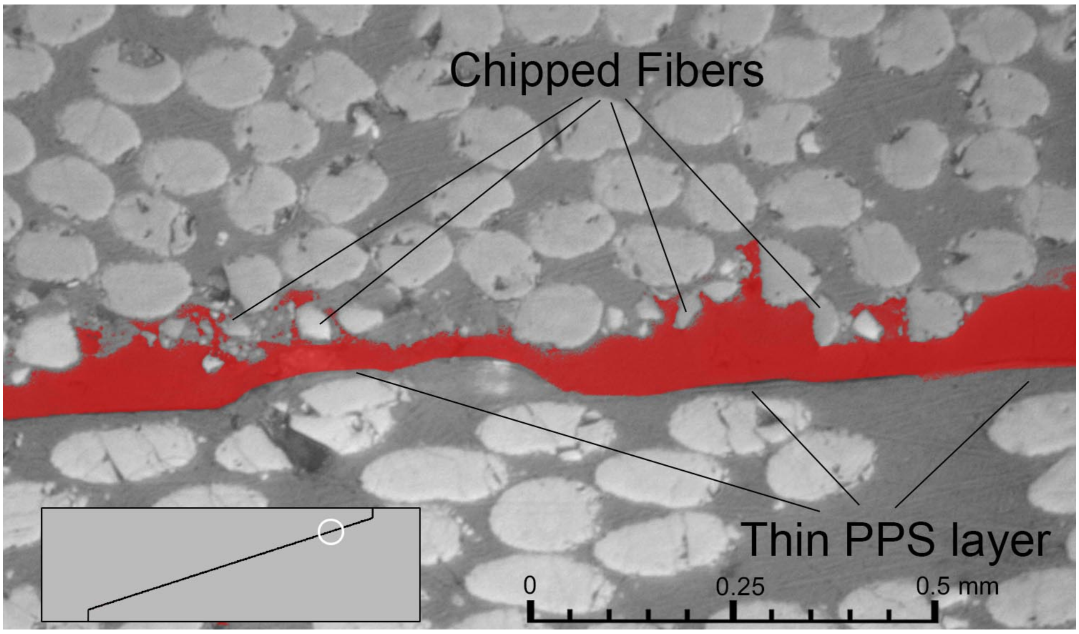

Figure 5.6: Difference in fibers at the surface of the CNC milled (top) and the pressed parts (bottom), gap in between the parts is indicated by the red area. A schematic overview to indicate where the picture has been taken is shown in the bottom left corner

Although the CTI specimen experienced surface temperatures close to the CVI specimen, it can be seen in Appendix G that there is a gap of about 2 $mm$ deep into the interface at the top and 4 $mm$ deep into the interface at the bottom. This is shown schematically in Figure 5.7. These gaps could be explained by the resin rich areas at the tip and the thin layer of PPS at the interface of the $CTI-2$ part preventing an unobstructed flow of electricity in between the parts. A mismatch between the shapes of the parts could have resulted in the gap at the location of the tips of the parts. However, the unjoined section at the angled interface in between the parts are unlikely to be caused by a mismatch in the shape.

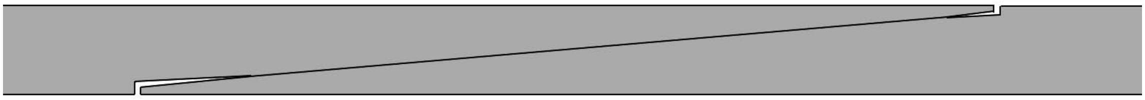

Figure 5.7: Schematic visual of the gaps at the top and bottom surface of the CTI specimen

A similar gap of about 1.5 $mm$ long can be found at the top of the STI specimen. The gap is about 0.1 $mm$ wide at the tip, preventing any flow of electricity to heat up the tip. Also, as mentioned before, it is suspected that the already welded section of the specimen creates an easier path for the electricity to flow.

## 5.3. Tensile Testing

In this chapter, the result of the tensile tests are provided. The tests are performed on a 250 $kN$ Zwick tensile test bench at a velocity of 2 $mm/min$. An extensometer with a spacing of 70 $mm$ to bridge over the joint interface is placed on the samples to accurately measure the strain. The pristine samples are monitored using the extensometer up to an applied load of 40 $kN$, instead of the failure load of about 59 $kN$, due to a more aggressive failure than the welded samples.

To obtain a detailed strain distribution along the scarf interface, a speckle pattern is applied to one side of the samples which is monitored every half second using Digital Image Correlation (DIC). This setup is shown in Figure 5.8. DIC is only applied to the joined samples. The samples are gripped over a distance of 50 $mm$ on both sides, resulting in a spacing between the clamps of 150 $mm$. 160 $g/m^2$ paper is applied to the clamped regions using super glue.

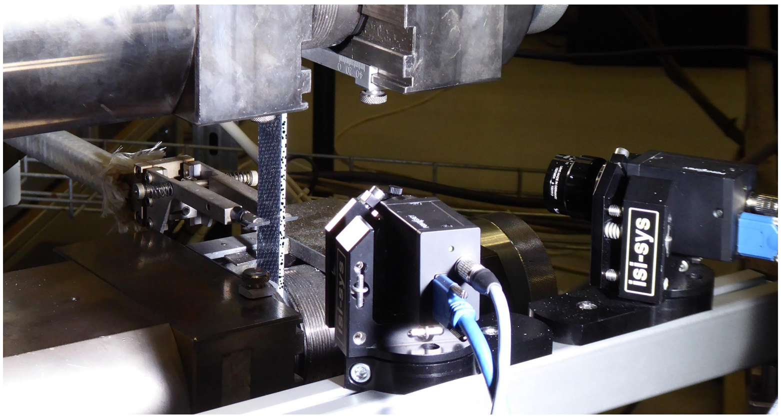

Figure 5.8: DIC monitoring of one of the sides of one of the test samples

The press welded samples are thinner due to additional squeeze-flow of the resin during joining of the part. As shown in Appendix D, the different thickness does not influence the failure load of the samples, but does affect the failure stress and stiffness. To compare the joined samples with the pristine samples, the stresses and stiffnesses are normalized using the pristine thickness of 3.1 $mm$. These normalized stresses and stiffnesses are compared to the pristine strength and stiffness given in Section 3.1.

The pristine samples result in a high coefficient of variation (COV) and a lower failure stress due to failure at the grips. Details can be found in Appendix I. Instead of using these values, the failure stress and stiffness as given by TenCate, 757 $MPa$ and 55.8 $GPa$ respectively, will be used to compare to the the induction welded and press joined samples.

For this comparison a t-test is used. This t-test is a statistical test that determines the probability that a certain value, for instance the pristine stiffness, could be found within a certain data set, for instance the stiffnesses of the of the tested samples. If this probability is higher than 5%, the single value is considered to be within the dataset. A z-test is used to compare the induction welded and press joined samples. This test is similar to the z-test, except for the addition of a standard deviation. By using a mean value and a standard deviation, two datasets can be compared with each other instead of reducing one of the datasets to a singular mean value.

### 5.3.1. Conventional Scarf

The results of the tensile test are shown in Table 5.2 and the average values, standard deviation, and COV are given in Table 5.3. For the welded samples the stiffness is obtained from the DIC measurements as the extensometer measurements are inaccurate. Details about how the stiffness is obtained and prove that the extensometer values are inaccurate can be found in Appendix H.

The failure stress of the CVI and CVP samples are confirmed to be statistically different from the pristine failure stress. Additionally, a z-test is used to determine that the CVI and CVP samples are statistically different, which is true for the normalized maximum stress. The stiffness of the pressed and induction welded samples are considered equal to each other and equal to the pristine stiffness. The induction welded scarf samples recover 32.4% of the pristine strength and the press bonded samples recover about 44.0% of the pristine strength. The stiffness recovery is 94.3% for the induction welded and 98.7% for the press joined samples.

DIC shows that the failure initiates at the tips of the interfaces. This is best seen in the sequence provided in Figure 5.9. It can be seen that about 30% of the failure load the first crack appears at the location of the step in the scarf joint. This crack grows inside the step until it progresses into the angled section of the scarf at around 80% of the failure load. This crack continuous to grow until final failure is reached. Just before final failure, the crack length inside the angled section measures about 1.6 $mm$. Similar progressive failure can be seen in all CV specimens, both induction welded as press joined.

The induction welded samples obtain a failure load that is 73.6% of the failure load of the pressed samples. The induction welded samples show an initial curvature with a maximum deflection of 1 $mm$, as shown in Figure 4.28, which introduces an additional tensile stress to one side of the sample and a compressive stress to the opposite side of the sample. From the DIC images, it can be concluded that the failure initiates at the tensile side for all induction welded samples, suggesting that the initial bending moment is the cause of the lower failure strength of the induction welded samples.

It can also be seen that the induction welded specimens have a consistently higher COV for all properties. It can be seen in Table 5.2 that the first sample has a lower failure stress than the second sample, which in turn has a lower failure stress than the third sample. The first samples are cut from the welded specimen as indicated in Figure 5.3. These increasing failure stresses towards the middle of the specimen can be correlated with an increasing welding temperature towards the middle of the specimen.

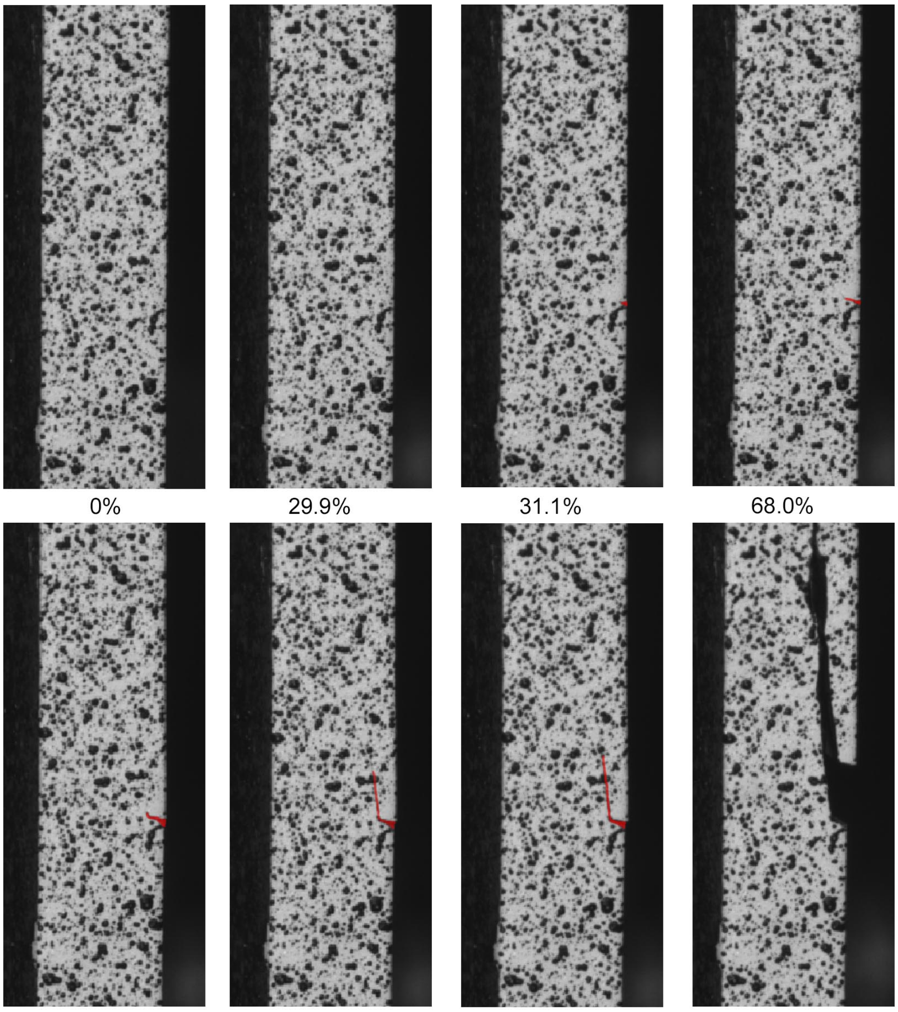
0% 29.9% 31.1% 68.0%

82.2% 94.7% 99.0% 100%

Figure 5.9: Progressive failure in the PPS matrix in between the CVP-T2 sample before final failure, crack indicated by the red area, underneath the frame the applied load as a percentage of the failure load is given

Table 5.2: Dimensions of the conventional scarf samples

| ID | $w_0$ | $t_0$ | $F_{max}$ | $\frac{t}{t_{ref}}$ | $\sigma_{max\,norm}$ | $\varepsilon_{F_{max}}$ | $E_{norm\,DIC}$ |
|---|---|---|---|---|---|---|---|
|  | $[mm]$ | $[mm]$ | $[N]$ | $[-]$ | $[MPa]$ | $[-]$ | $[GPa]$ |
| $CVI-T1$ | 25.41 | 3.32 | 18555 | 1.07 | 235 | 0.0090 | 56.95 |
| $CVI-T2$ | 25.46 | 3.19 | 19077 | 1.03 | 241 | 0.0094 | 47.84 |
| $CVI-T3$ | 25.42 | 3.34 | 20357 | 1.07 | 258 | 0.0101 | 53.13 |
| $CVP-T1$ | 25.46 | 2.87 | 26623 | 0.92 | 336 | 0.0131 | 57.84 |
| $CVP-T2$ | 25.45 | 2.92 | 25753 | 0.94 | 326 | 0.0123 | 52.77 |
| $CVP-T3$ | 25.44 | 2.89 | 26555 | 0.93 | 336 | 0.0129 | 54.67 |

Table 5.3: Weibull distribution for the conventional scarf joint

| | $t_0$ | | $F_{max}$ | | $\sigma_{max\,norm}$ | | $E_{norm\,DIC}$ | |
|---|---|---|---|---|---|---|---|---|
| | $CVI$ | $CVP$ | $CVI$ | $CVP$ | $CVI$ | $CVP$ | $CVI$ | $CVP$ |
| | $[mm]$ | $[mm]$ | $[N]$ | $[N]$ | $[MPa]$ | $[MPa]$ | $[GPa]$ | $[GPa]$ |
| $\bar{x}$ | 3.28 | 2.89 | 19330 | 26310 | 245 | 333 | 52.64 | 55.09 |
| $s$ | 0.08 | 0.03 | 927 | 484 | 12 | 6 | 4.57 | 2.56 |
| $COV$ | 2.48% | 0.87% | 4.80% | 1.84% | 4.88% | 1.74% | 8.69% | 4.65% |

## 5.3.2. Continuous Scarf

The results of the tensile test are shown in Table 5.4 and the average values are shown in Table 5.5. A t-test shows that the results are statistically different from the pristine stress and stiffness. The resulting normalized strengths are respectively 34.0% and 43.3% of the pristine failure stress and 91.9% and 95.9% of the stiffness for the induction welded and press joined samples.

These percentages are close to the conventional scarf results and a z-test show that both the CTI and CVI are statistically similar. This is also shown for the CVP and CTP samples. Therefore, there is no significant difference between the continuous scarf and the conventional scarf. This suggests that the failure modes of the continuous and conventional scarf are similar. The similar failure mode of the CTI and CVI samples is confirmed by the DIC images, showing a progressive failure starting in inside the step in the matrix and continuing into the angles section of the scarf before final failure for all samples.

Again the induction welded samples show a lower failure strength, now 78.4% of the pressed samples. Similar to the CVI samples, the CTI samples have an initial curvature with a maximum deflection of about 1 $mm$, resulting in an additional tensile and compressive load in the samples. However, unlike the CVI samples, all the CTI samples initiate failure at the compressive side of the sample. This contradicts the conclusion that the initial deflection is the cause of the earlier failure in the induction welded samples.

Similar to the CVI specimen, the CTI specimen show a high COV. The samples are cut as shown in Figure 5.3 and it can be seen that the individual samples have an increased failure strength towards the middle of the specimen.

Table 5.4: Dimensions of the continuous scarf samples

| ID | $w_0$ | $t_0$ | $F_{max}$ | $\frac{t}{t_{ref}}$ | $\sigma_{max\,norm}$ | $\varepsilon_{F_{max}}$ | $E_{norm\,DIC}$ |
|---|---|---|---|---|---|---|---|
| | $[mm]$ | $[mm]$ | $[N]$ | $[-]$ | $[MPa]$ | $[-]$ | $[GPa]$ |
| $CTI-T1$ | 25.48 | 3.00 | 16023 | 0.96 | 202 | 0.0083 | 49.39 |
| $CTI-T2$ | 25.40 | 3.05 | 20364 | 0.98 | 258 | 0.0102 | 51.98 |
| $CTI-T3$ | 25.39 | 3.07 | 24464 | 0.99 | 310 | 0.0126 | 52.47 |
| $CTP-T1$ | 25.50 | 2.72 | 25874 | 0.88 | 327 | 0.0124 | 53.74 |
| $CTP-T2$ | 25.48 | 2.74 | 26207 | 0.88 | 331 | 0.0127 | 53.53 |
| $CTP-T3$ | 25.39 | 2.71 | 25684 | 0.87 | 326 | 0.0123 | 53.31 |

Table 5.5: Weibull distribution for the continuous scarf joint

| | $t_0$ | | $F_{max}$ | | $\sigma_{max\,norm}$ | | $E_{norm\,DIC}$ | |
|---|---|---|---|---|---|---|---|---|
| | $CTI$ | $CTP$ | $CTI$ | $CTP$ | $CTI$ | $CTP$ | $CTI$ | $CTP$ |
| | $[mm]$ | $[mm]$ | $[N]$ | $[N]$ | $[MPa]$ | $[MPa]$ | $[GPa]$ | $[GPa]$ |
| $\bar{x}$ | 3.04 | 2.72 | 20284 | 25922 | 257 | 328 | 51.28 | 53.53 |
| $s$ | 0.04 | 0.02 | 422 | 265 | 54 | 2.65 | 1.66 | 0.22 |
| $COV$ | 1.19% | 0.56% | 20.81% | 1.02% | 21.04% | 0.81% | 3.23% | 0.40% |

## 5.3.3. Stepped Lap Scarf

The results of the tensile test are shown in Table 5.6 and the average values are provided in Table 5.7. As with the previous samples a t-test is used to determine the statistical similarity between the tested samples and the pristine laminate properties. The t-test rejects the possibility that the failure strengths of the pressed and induction welded samples are equal to the pristine failure strength. The stiffness is considered equal for the induction welded samples, although the stiffness of the press joined samples is considered different from the pristine stiffness. The z-test also rejects the possibility that the induction welded and pressed samples are statistically similar. The failure strength of the STI samples is 46.2% of the pristine failure strength and the STP samples result in a 59.4% recovery of the pristine failure strength. The stiffnesses are respectively 96.3% and 94.6% of the original stiffness for the STI and the STP samples.

Analysis of the DIC images shows that only two out of six samples show progressive failure. The other four samples fail suddenly before any crack is visible within the sample. Additionally, the crack that is seen in the two progressive failing samples does not show until just before failure. The two progressive failing samples still suggest the failure initiates in the first step in the PPS matrix, but the failure mechanics are different as the joint fails suddenly. For the induction welded specimen with an initial deformation of 1 $mm$ the progressive failure initiates at the compressive side of the sample.

The fracture surface of the $CTP - T1$ sample can be seen in Figure 5.10, indicated in the figure are fibers that have fractured during failure. Similar fracture surfaces can be seen in all STI and STP samples. DIC shows that the failure initiates in the step opposite to the edge that experiences fractured fibers. It is expected that the side at which the fibers are fractured is the last part of the joint to fail, loaded both by a tensile force and a bending moment due to asymmetric load path.

Again the induction welded specimens show a higher COV than the press joined specimens and it can be seen in Table 5.6 that the failure stress of the samples increases towards the center of the specimen. However, unlike the CTI and CVI specimen, the temperatures during welding were decrease towards the center of the specimen.

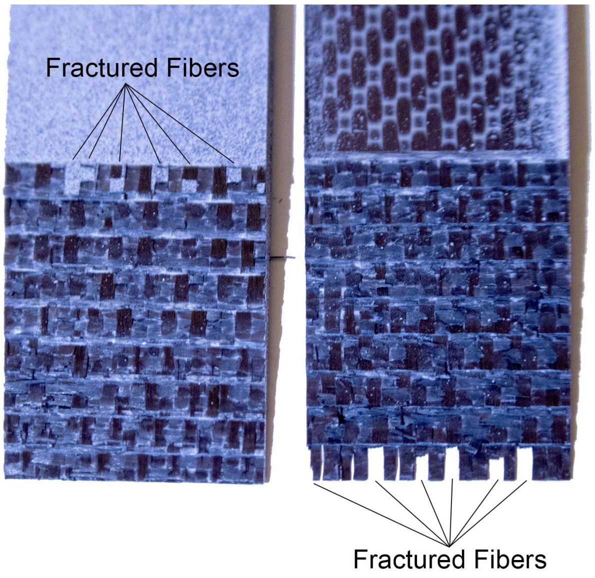

Figure 5.10: Fracture surface of the STP-T1 sample. Fractured fibers are indicated in the picture.

Table 5.6: Dimensions of the stepped lap samples

| ID | $w_0$ | $t_0$ | $F_{max}$ | $\frac{t}{t_{ref}}$ | $\sigma_{max\,norm}$ | $\varepsilon_{F_{max}}$ | $E_{norm\,DIC}$ |
|---|---|---|---|---|---|---|---|
| | $[mm]$ | $[mm]$ | $[N]$ | $[-]$ | $[MPa]$ | $[-]$ | $[GPa]$ |
| $STI - T1$ | 25.45 | 3.03 | 22079 | 0.97 | 279 | 0.0111 | 50.96 |
| $STI - T2$ | 25.37 | 3.07 | 29157 | 0.99 | 370 | 0.0150 | 54.58 |
| $STI - T3$ | 25.38 | 3.15 | 31627 | 1.01 | 401 | 0.0169 | 55.73 |
| $STP - T1$ | 25.42 | 2.61 | 34238 | 0.84 | 433 | 0.0174 | 52.93 |
| $STP - T2$ | 25.40 | 2.61 | 35673 | 0.84 | 452 | 0.0175 | 53.55 |
| $STP - T3$ | 25.39 | 2.57 | 36747 | 0.83 | 466 | 0.0185 | 51.78 |

Table 5.7: Weibull distribution for the stepped lap joint

| | $t_0$ | | $F_{max}$ | | $\sigma_{max\,norm}$ | | $E_{norm\,DIC}$ | |
|---|---|---|---|---|---|---|---|---|
| | $STI$ | $STP$ | $STI$ | $STP$ | $STI$ | $STP$ | $STI$ | $STP$ |
| | $[mm]$ | $[mm]$ | $[N]$ | $[N]$ | $[MPa]$ | $[MPa]$ | $[GPa]$ | $[GPa]$ |
| $\bar{x}$ | 3.08 | 2.60 | 27621 | 35553 | 350 | 450 | 53.76 | 52.75 |
| $s$ | 0.06 | 0.02 | 496 | 126 | 63 | 17 | 2.49 | 0.90 |
| $COV$ | 1.98% | 0.89% | 17.94% | 3.54% | 18.12% | 3.68% | 4.63% | 1.70% |

## 5.4. Finite Element Modeling

FEM is performed to investigate slight variations in the geometry of the joints and quantify the effect of the initial curvature of the induction welded specimen. The plies of the laminate are modeled as separate surfaces and joined to create the laminate. For the welded samples a thin layer of PPS matrix is modeled in between the parts. Due to the expected uniform load through the width of the specimen and the small elements required, 2D shell elements will be used. Shell elements have a single element through the thickness, for which the thickness needs to be specified. The thickness given to the elements will be in the direction of the width of the samples as it is expected there is a limited variation in the stress in this direction. The thickness is set to the width of the specimen divided by 200, to prevent inaccurate result due to high aspect ratio elements. This results in a shell thickness of 0.125 $mm$. Consequently the applied load is also divided by 200.

The boundary conditions applied are similar to the tensile test performed in the previous chapter. The modeled sample has a length of 250 $mm$ with a clamped area of 50 $mm$ on both sides. One side of the samples is clamped, whereas the other side of the sample is allowed to slide in the $x$ direction. The load is applied to the edges of the clamped area that is allowed to move in the $x$ direction. These boundary conditions are shown in Figure 5.11.

Figure 5.11: Boundary conditions used in the FEM model

Failure in the plies is determined using the Tsai-Hill criterion, given in Equation (5.2). The axis are as indicated in Figure 5.11. This criterion states that if the equation is satisfied the laminate has failed. In this equation $X_t$, $Y_t$, and $S$ represent the $0°$ tensile, $90°$ tensile, and shear failure strengths of the material respectively.

$$\frac{\sigma_x^2}{X_t^2} - \frac{\sigma_x \sigma_y}{X_t^2} + \frac{\sigma_y^2}{Y_t^2} + \frac{\tau_{xy}^2}{S^2} \geq 1 \tag{5.2}$$

Failure in the adhesive layer is determined using the Christensen criterion, given in Equation (5.3). Again failure is implied if the equation is satisfied. In addition to see where the PPS matrix has failed, this criterion is also used to determine the number of failed elements in the PPS matrix. The number of failed elements in the PPS matrix divided by the total number of elements in the PPS matrix is the failure ratio or $R_f$. In combination with a test data a critical $R_F$ can be set. It is assumed that if the $R_{f\,crit}$ is reached, the laminate will have failed. Using this $R_{f\,crit}$ it is possible to determine whether slight variations of the tested geometry have failed at a given load. This method is called Damage Zone Modeling (DZM).

$$\begin{aligned}\left(\frac{1}{X_t} - \frac{1}{X_c}\right)(\sigma_{11} + \sigma_{22} + \sigma_{33}) + \left(\frac{1}{2X_tX_c}\right)((\sigma_{11} - \sigma_{22})^2 + (\sigma_{22} - \sigma_{33})^2 + (\sigma_{33} - \sigma_{11})^2) + \ldots \\ \left(\frac{3}{X_tX_c}\right)(\sigma_{12}^2 + \sigma_{23}^2 + \sigma_{31}^2) \geq 1\end{aligned} \tag{5.3}$$

### 5.4.1. Pristine Specimen

The pristine test sample is modeled using 0.31 $mm$ quadrilateral elements, such that each ply has a single element through the thickness. The mechanical properties of the CF/PPS are provided in Table 5.8.

Table 5.8: Material properties of CF/PPS as used for the ANSYS model

| | | | | | | | |
|---|---|---|---|---|---|---|---|
| $\rho$ | 1550 | $[kg/m^3]$ | [70] | $\nu_{xy}$ | 0.033 | $[-]$ | [77] |
| $E_x$ | 55.8 | $[GPa]$ | [70] | $\nu_{yz}$ | 0.36 | $[-]$ | [70] [3] |
| $E_y$ | 51.7 | $[GPa]$ | [70] | $\nu_{xz}$ | 0.36 | $[-]$ | [70] [3] |
| $E_z$ | 3.8 | $[GPa]$ | [70] [1] | $X_t$ | 757 | $[MPa]$ | [70] |
| $G_{xy}$ | 4.04 | $[GPa]$ | [70] | $Y_t$ | 754 | $[MPa]$ | [70] |
| $G_{yz}$ | 4.04 | $[GPa]$ | [70] [2] | $S$ | 119 | $[MPa]$ | [70] |
| $G_{xz}$ | 4.04 | $[GPa]$ | [70] [2] | | | | |

To verify the model a pristine sample is analyzed for tensile strength and three-point bending bending. For the tensile analysis the boundary conditions as shown in Figure 5.11 are used. Given the simple stacking sequence, the laminate should fail at 757 $MPa$ in tension. This translates to a load of 293.34 $N$ FEM model.

The results of the analysis show that the Tsai-Hill criterion results in a value of 1 for the majority of the laminate. At the transition between the fixed clamped area and the free laminate a singularity is found with Tsai-Hill values of 16.4. This singularity is due to the fixed boundary conditions of the clamped area and, as it is not a realistic representation, ignored in the analysis of the results. Additionally, the stiffness of the part determined using the FEM results, 56.3 $GPa$, deviates less than 1% from the pristine stiffness of 55.8 $GPa$.

Finally, a simply supported three-point bending test is simulated. The boundary conditions are shown in Figure 5.12. Using Equation (5.4) and aiming for a deflection of 1 $mm$, the force needed is determined to be 10.64 $N$ for a full width sample and 0.0532 $N$ for the Ansys Model. This deflection should give a $\sigma_m$ of 16.6 $MPa$. Again the results, a simulated deflection of 1 $mm$ and a $\sigma_m$ of 16.8 $MPa$, show a difference of about 1% from the theoretical values.

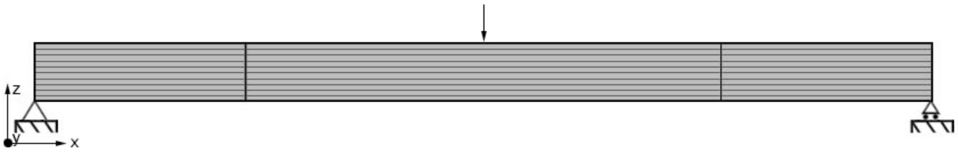

Figure 5.12: Boundary conditions used for the simply supported three-point bending model

$$P = \frac{48\delta EI}{L^3} \tag{5.4}$$

### 5.4.2. Conventional Scarf

As can be seen in the micrography pictures in Appendix G there is no noticeable matrix layer in between the two welded parts. However, a thin layer of matrix needs to be modeled to realistically model the joint. This matrix layer is set to 0.05 $mm$ thickness, the smallest that can be modeled within the academic license meshing limitations. To obtain a constant thickness in the modeled matrix material, a slight height offset is needed between the two parts.

The model is meshed with a multi-zone quadrilateral/triangle method, with an element size of 0.015 $mm$ to obtain three elements through the thickness of the matrix. A section of the resulting mesh can be seen in Figure 5.13. The laminate properties are the same as for the pristine model. The PPS is modeled using a bilinear stress strain curve. The input properties are given in Table 5.9. In Figure 5.14 the stress strain curve for PPS at room temperature is shown, together with the bilinear stress strain

---

[1] Out of plane stiffness assumed to be equal to the matrix stiffness

[2] Shear stiffness of the laminate assumed to be equal in all three planes

[3] Out of plane Poisson's ratio assumed to be equal to resin Poisson's ratio

curve used in the FEM model. The tangent modulus required to model the second linear section of the stress strain curve is chosen such that the curve continues almost horizontal after yield, similar to the tested data. The clamped tensile boundary conditions, as shown in Figure 5.11, are applied to this model.

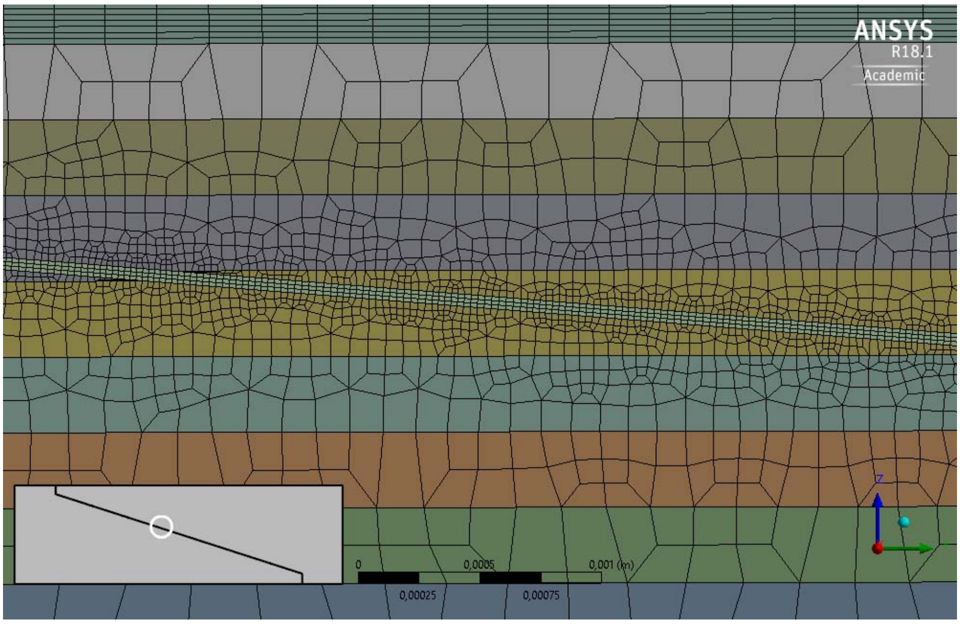

Figure 5.13: Fine mesh of the matrix layer of the CV FEM model

Table 5.9: Material properties of PPS as used for the ANSYS model

| | | | | |
|---|---|---|---|---|
| $\rho$ | 1350 | $[kg/m^3]$ | [70] | |
| $E$ | 3.8 | $[GPa]$ | [70] | |
| $\nu$ | 0.36 | $[-]$ | [70] | |
| $X_{t\ yield}$ | 114 | $[MPa]$ | [70] | [1] |
| Tangent Modulus | 1 | $[MPa]$ | | [2] |
| $X_t$ | 90.3 | $[MPa]$ | [70] | |
| $X_c$ | 148 | $[MPa]$ | [70] | |

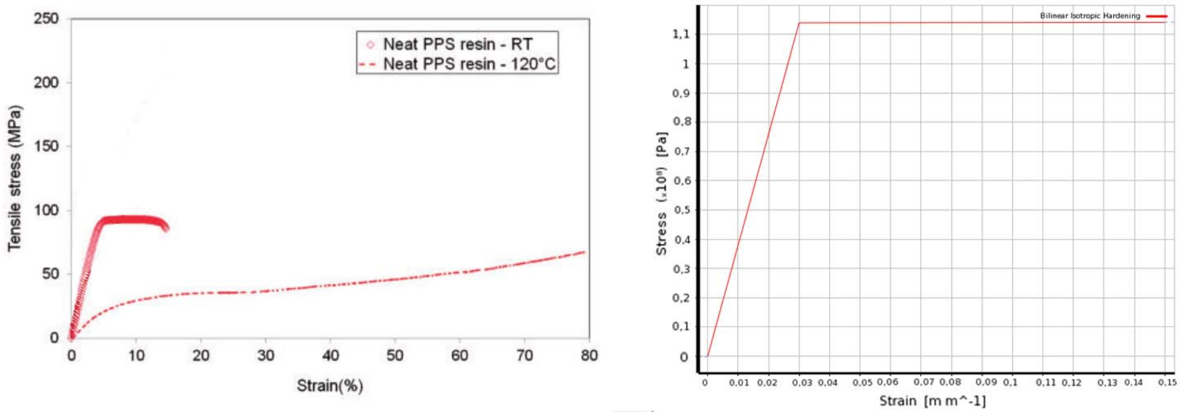

Figure 5.14: Stress Strain curve for pure PPS [5] (left) Simulated bilinear stress strain curve in ANSYS (right)

---

[1] Calculated using the given stiffness and yield strain of 0.03%

[2] The tangent modulus is chosen such that the stress mimics the actual behavior

The average failure stress of the CVP samples, 333 $MPa$ given in Table 5.2, is used to determine the applied load of 129 $N$. At this load the simulation indicates two possible failures. In the ply directly underneath the step a stress concentration can be found resulting in Tsai-Hill values of 2.17, the stress concentration can be seen in Figure 5.15. The majority of the laminate has a Tsai-Hill value of around 0.2 indicating no failure.

The second failure is indicated by the Christensen criterion, which shows a failed PPS layer at the location of the step of the interface and the first 0.8 $mm$ of the scarf. The extent of this failure inside the angled section of the scarf is less than the failure seen during the tensile test, which is about 1.6 $mm$. This can be explained by the fact that the FEM model still transfers load through the PPS that has failed according to the Christensen criterion. In reality the behavior is more complex, with a changing load path and smaller area to transfer the load when the first section of the PPS fails.

The simulated stiffness of the scarf joint of 55.81 $GPa$ is close to the tested and pristine stiffness of 55.1 and 55.8 $GPa$ respectively.

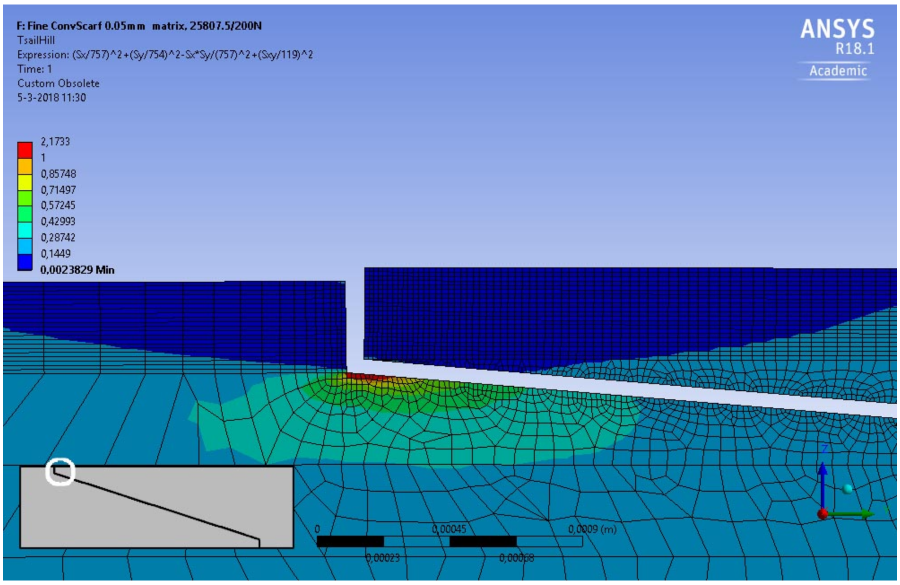

Figure 5.15: Stress concentration in the second ply

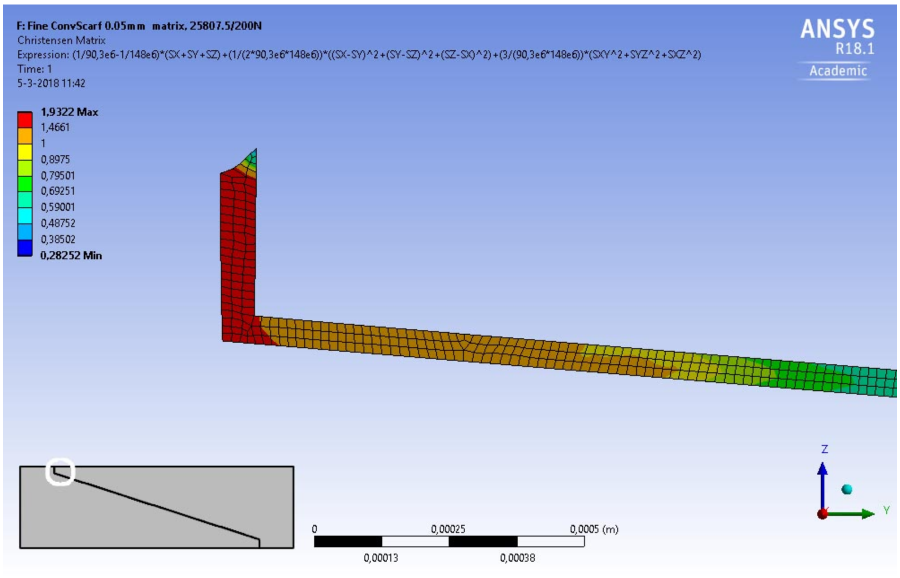

Figure 5.16: Christensen criterion applied to the PPS matrix in between the two parts

The same simulation is run at three different PPS element sizes to investigate the impact of the mesh size on the results. A fine mesh with a PPS element size of 0.015 $mm$, a medium mesh with an element size of 0.025 $mm$, and a coarse mesh with an element size of 0.05 $mm$. Three different results are used for this comparison, the Tsai-Hill concentration at the PPS/Ply interface, the maximum Christensen value, and the ratio of failed PPS elements over the total number of PPS elements, $R_f$. These results are provided in Table 5.10. It can be seen that the failure ratio $R_f$ decreases with a finer mesh and the maximum Christensen criterion experiences a minor increase. On the other hand, the Tsai-Hill concentration increases rapidly with a finer mesh. This suggests that the concentration is a singularity caused by the model. This observation is supported by the DIC which shows the failure initiates inside the PPS matrix in between the parts. Therefore, it is decided to ignore the Tsai-hill concentration shown in Figure 5.15. It should also be noted that the failure ratio has not converged to a constant value yet. However, smaller elements cannot be used due to a meshing limitation in the academic version of ANSYS. The critical failure ratio, $R_{f\ crit}$, is set to 6.89% for the CV joint.

Table 5.10: Comparison between the different element sizes

| | Coarse mesh | Medium mesh | Fine mesh | |
|---|---|---|---|---|
| $N_{PPS\,Elm}$ | 1381 | 4148 | 7653 | [−] |
| Max Tsai-Hill | 1.412 | 1.949 | 2.173 | [−] |
| Max Christensen | 1.838 | 1.893 | 1.932 | [−] |
| $R_f$ | 8.40 | 7.43 | 6.89 | [%] |

To investigate the effect of a thicker matrix line and whether this has a large influence on the results, a simulation is run with a PPS layer of 0.15 $mm$ thick instead of 0.05 $mm$. Two variations of the simulation of this thicker matrix layer are run. The first with the same element size as the fine CV simulation and the second with a bigger element size in the PPS matrix. For the second simulation, the element size is chosen such that the PPS matrix has a similar number of total elements. The results are presented in Table 5.11. The maximum Christensen criterion is slightly higher for the thin PPS matrix when compared tot the thick layer, whereas the failure ratio is higher for both the fine and coarse PPS mesh. From these results it is concluded that a different matrix thickness does not have a significant influence on the FEM results.

Table 5.11: Comparison between the a thin and a thicker PPS matrix

| | 0.05 $mm$ PPS Fine Mesh | 0.15 $mm$ PPS Fine Mesh | 0.15 $mm$ PPS Coarse Mesh | |
|---|---|---|---|---|
| $N_{PPS\,Elm}$ | 7653 | 21128 | 7744 | [−] |
| $R_f$ | 6.89 | 7.55 | 7.31 | [%] |
| Max Christensen | 1.932 | 1.855 | 1.857 | [−] |

The effect of the deflection in the induction welded parts is investigated by applying a point load to the tensile strip. The 10.64 $N$ load, applied in the same location as shown in Figure 5.12, is applied to the CV joint with boundary conditions as shown in Figure 5.11. This load results in curvature of 1 $mm$ in a three point bending test, similar to the initial curvature of the induction welded samples. As the bending introduces a compression at the top of the laminate and a tension at the bottom, the results are split. These results are provided in Table 5.12. As can be seen, the stress is increased at the bottom and decreased at the top. However, the effect is minimal and not likely to be the sole contributer to the lower failure stress of the induction welded samples.

Table 5.12: FEM comparison between the pure tensile test and the tensile test with a forced deflection of 1 $mm$

| | No bending | Bending Top | Bending Bottom | |
|---|---|---|---|---|
| $N_{PPS\,Elm}$ | 7653 | 3826 | 3827 | [−] |
| $R_f$ | 6.89 | 6.77 | 7.08 | [%] |
| Max Christensen | 1.932 | 1.908 | 1.936 | [−] |

Finally, the effect of different scarf angles is investigated and simulations are run with scarf angles of 2.3 and 7.05 $deg$. The results are provided in Table 5.13. It can be seen that an angle of 2.3° results in a lower $R_f$. Likewise the higher angle of 7.05° results in a higher $R_f$. This DZM method indicates that the smaller angle will have a higher failure load and the higher angle will have a lower failure load.

Table 5.13: FEM comparison between different scarf angles

| | 2.3 $deg$ | 4.7 $deg$ | 7.05 $deg$ | |
|---|---|---|---|---|
| $N_{PPS\,Elm}$ | 15478 | 7653 | 5216 | [−] |
| $R_f$ | 2.31 | 6.89 | 17.79 | [%] |
| Max Christensen | 1.925 | 1.932 | 1.9034 | [−] |

## 5.4.3. Continuous Scarf

The continuous scarf is modeled with plies parallel to the interface as shown in Figure 5.17. A new coordinate system for these plies, is defined aligning the $X$ axis parallel to these plies. Triangular sections of PPS matrix are modeled to fill the empty space left by the angled plies. The multi-zone quadrilateral/triangular method failed to mesh due to the added PPS triangles and the method is changed to all triangles, again with an element size of 0.015 $mm$ for the PPS matrix. Quadrilateral shell elements are preferred over triangular elements as they result a better representation when bending loads are applied. However, the test sample is predominantly loaded in tension. To verify this new meshing method a simulation is run for the conventional scarf with an all-triangles mesh, which results in a comparable failure ratio and maximum Christensen criterion in the PPS matrix.

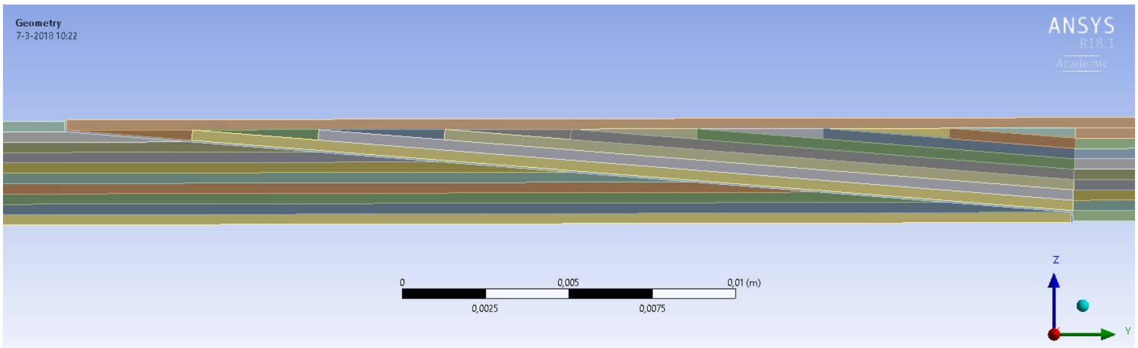

Figure 5.17: Continuous scarfed model

As can be seen in the micrography images in Appendix G, no PPS matrix is visible between the parts. Similar to the CV model, the PPS layer thickness is set to 0,05 $mm$ for the CT model. It can also be seen that in reality the PPS triangles are not as profound as modeled for the simulation.

Similar to the CV model, the failure likely initiates in the step at the surfaces of the joint. This is also supported by the DIC images from the tensile tests. The failure ratio is slightly lower, 5.81% for the CT samples compared to the 6.89% for the CV samples. The Tsai-hill stress concentration is higher and located at a different location. Again, this stress concentration is likely caused by the model and not representative of the actual test samples. The stiffness of the continuous scarfed sample deviates only 1.5% from the pristine stiffness.

## 5.4.4. Stepped Lap Scarf

The stepped lap model is meshed with a multi-zone quadrilateral/triangle mesh with a PPS layer element size of 0.015 $mm$. In the micrography images in Appendix G, no PPS matrix can be seen in between the parts in the through the thickness direction. However, lengthwise resin rich areas are visible with a length of around 0.75 $mm$. Therefore, the PPS layer is modeled with a thickness of 0.05 $mm$ and an additional length at the step of 0.75 $mm$. The surfaces of the FEM model are shown in Figure 5.19.

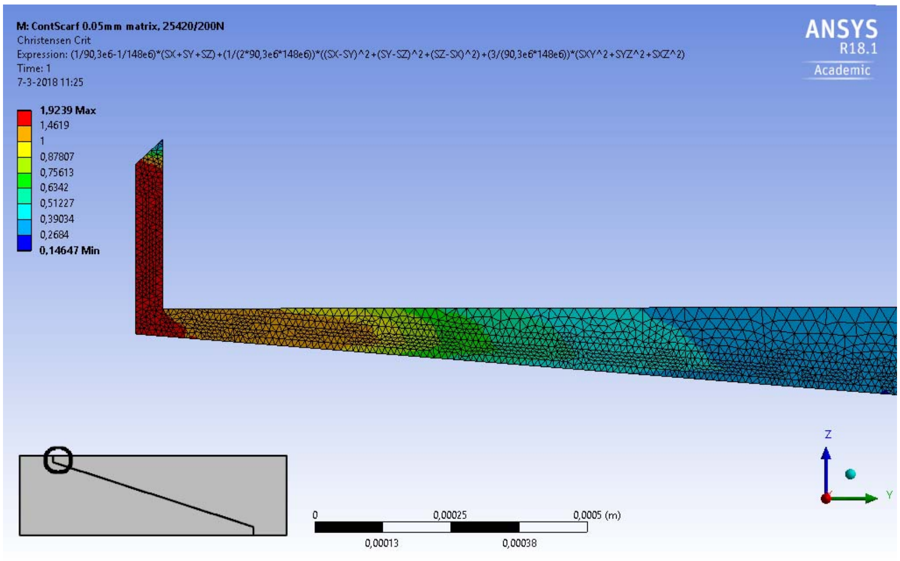

Figure 5.18: Christensen Criterion applied to the PPS matrix of the CV sample

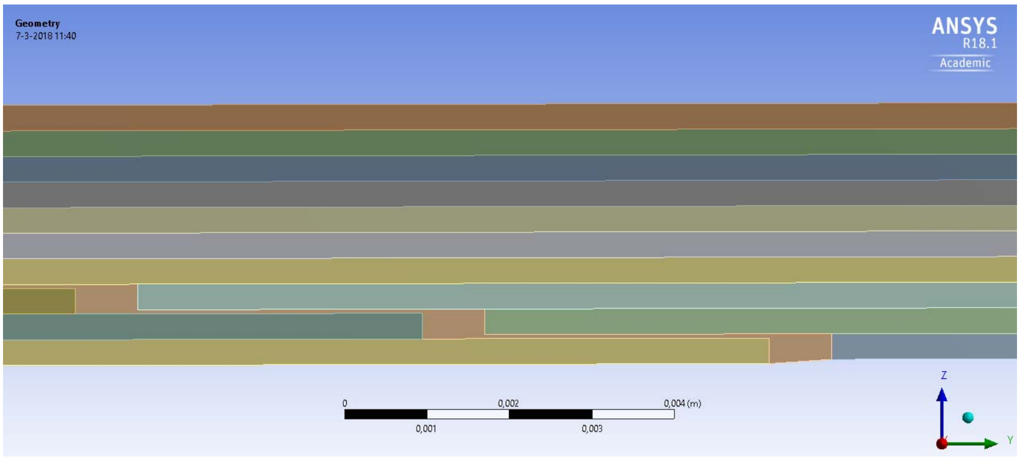

Figure 5.19: Geometry of the PPS matrix of the stepped lap FEM model

Similar to the scarfed samples, the PPS matrix fails at the location of the steps. However, for the stepped lap samples there are more steps that induce stress concentrations. This results in a higher failure ratio of 14.03%, although the maximum Christensen criterion is lower with a value of 1.77. Although each step in the PPS matrix has a number of failed elements, the majority of the failed elements is located in the first and last step of the overlap, also extending into the thin PPS layer. The initial step of the PPS matrix is shown in Figure 5.20 and a step in between the plies is shown in Figure 5.21. Similar to the previous test samples, the stiffness of the stepped lap joint is within 1% of the pristine stiffness.

The higher amount of failed elements in the initial step indicate that the failure initiates at the first step of the interface. This is supported by DIC images taken during the tensile testing. However, as discussed in Section 5.3.3, the failure of the stepped lap specimens is sudden instead of the progressive failure seen in the scarfed specimens. Based on the FEM results, it is likely that once one step fails, the remaining steps fail as well.

There are no stress concentrations in the simulation that would explain the fiber failure as seen on the fracture surfaces. It is expected that failure initiated at the clean side of the fracture surface and the fiber failure is caused by a combination of an increased stress and bending moment.

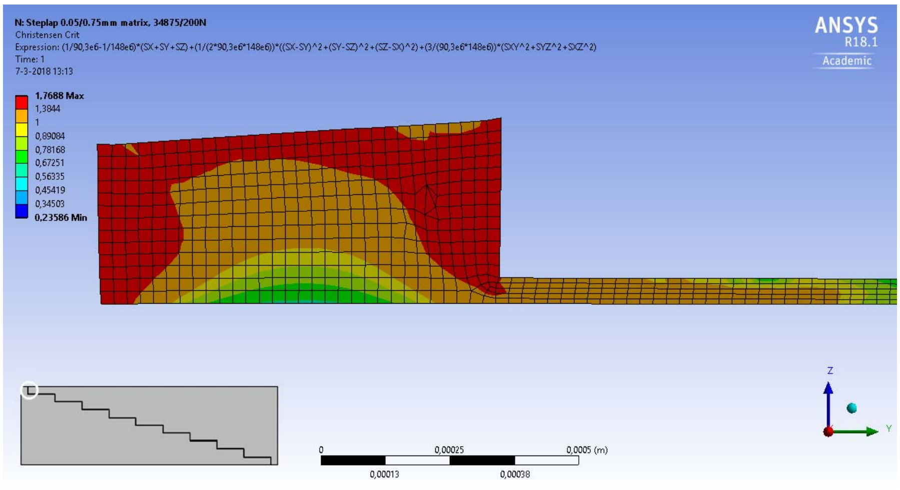

Figure 5.20: Christensen criterion applied to the initial step of the PPS matrix

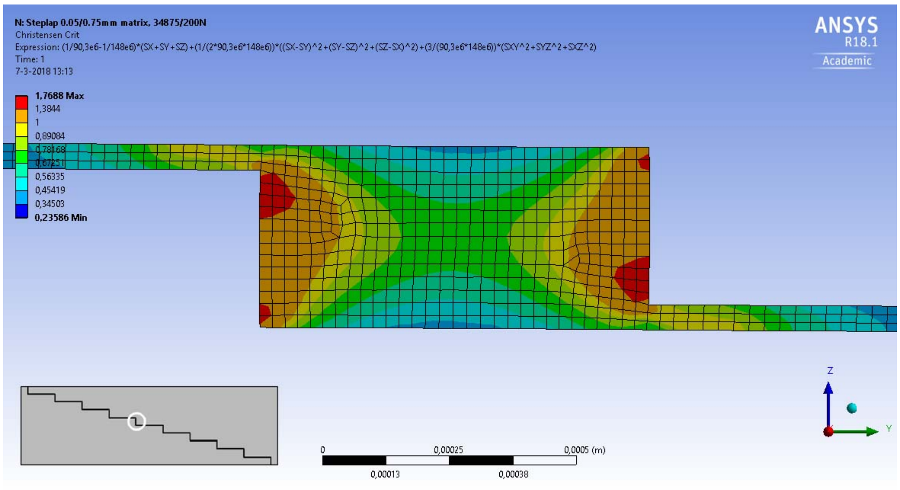

Figure 5.21: Christensen criterion applied to a middle step of the PPS matrix

Finally, it is also investigated whether decreasing the overlap length would be beneficial for the failure load. Two additional simulations are run with an overlap length of 25.2 and 75.6 $mm$. The results are provided in Table 5.14. Similar to the FEM results of the scarf angle, the $R_f$ increases with a decreasing overlap length and decreases with an increasing overlap length. Again, it is indicated by the FEM that increasing the overlap length will result in a higher failure load.

Table 5.14: Comparison different overlap lengths for the stepped lap sample

| | 25.2 $mm$ | 37.8 $mm$ | 75.6 $mm$ | |
|---|---|---|---|---|
| $N_{PPS\,Elm}$ | 7965 | 10084 | 16348 | [−] |
| $R_f$ | 35.58 | 23.08 | 14.03 | [%] |
| Max Christensen | 1.780 | 1.769 | 1.758 | [−] |

## 5.5. Discussion

The recovery of the failure strength for the induction welded specimens and press joined specimens and their standard deviation, as determined in Section 5.3, is summarized in Figure 5.22. It can be seen that the failure stresses of the induction welded specimens are consistently lower than that of the press joined specimens and have a higher COV. The latter indicates that the quality of the weld, as the coil moves from the start to the end of the panel, is not consistent and should be improved.

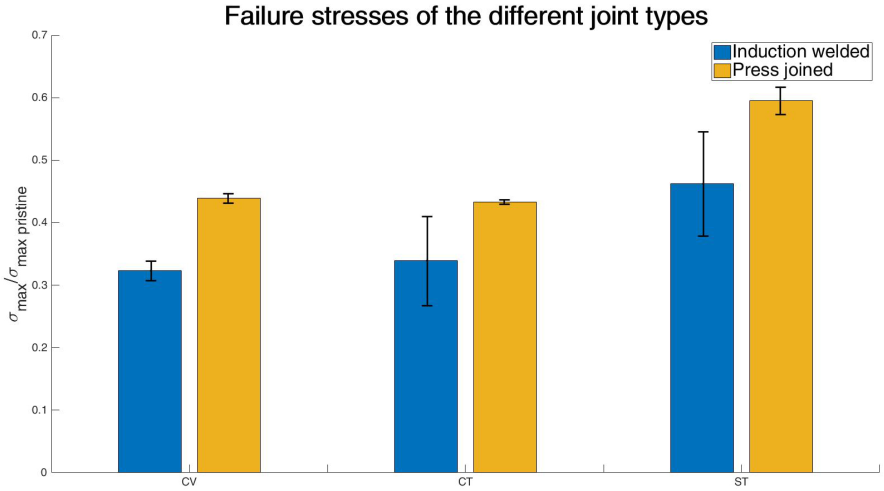

Figure 5.22: Normalized failure stresses and standard deviation of the three different joint types and two different welding methods obtained using tensile testing

Although the recovery strengths of the press joined samples are higher than that of the induction welded samples, it is only about 44% and 59% of the pristine strength for the scarfed specimens and the stepped lap joints respectively. This shows that the simple analytic equations used to determine the needed angle or overlap length over predict the strength. Both equations assume the joint interface is solely loaded in shear load and neglect the normal stresses inside the steps at the top and bottom of the joint. As shown by the DIC and FEM, the failure initiates in the initial steps. Therefore, this can not be neglected during the determination of the scarf angle or overlap length. Additionally, the scarf angle equation assumes the complete thickness of the laminate is used to transfer the shear load, whereas in reality the step in the top and bottom ply reduces the effective area. This has not been taking into account which contributes to the lower failure load of the scarfed samples.

The lower failure stresses of the induction welded specimens can have several causes. Namely, the initial curvature of 1 $mm$ due to deflection during welding, the unjoined areas that can be seen in the CT and ST samples, voids in the welded area, and residual stresses due to local heating during induction welding.

As mentioned, each CVI sample fails at the tensile side induced by the initial deformation. However, the CTI and STI specimens show initial failure at the compressive side. FEM also indicates that the initial curvature of the induction welded specimens has negligible influence on the final failure strength of the specimen. Therefore, the initial deformation is not expected to be the main cause of the lower failure strength in the induction welded specimens.

The initial non-joined areas seen in the microscopy images for the CT and ST joints are not expected to have a major influence on the failure strength either. If these gaps near the tips would have had a significant influence, then one of the following two statements should be true. Either the failure stress of the induction welded CT samples would be lower than that of the failure stress of the induction welded CV samples. Or the failure strength of the press joined CT samples would be higher than that of the CV samples. As can be seen in the results, neither is the case.

The voids inside the laminate are scattered randomly throughout the heated area. The failure initiates at the initial step and continuous throughout the PPS matrix in between the parts, whereas most voids are located away from the interface and initial steps. Additionally, voids in laminates have been shown to significantly reduce the fatigue strength but have a negligible effect on the static strength.

The last factor adding to the induction welded parts are residual stresses caused by the welding process. These stresses can be introduced in the laminate due to the difference in thermal expansion between the fibers and the matrix or consolidating the sections of the laminate at different times. This thermal expansion can affect the laminate both in the through the thickness direction as along the weld-line. In the press joined samples a constant and uniform cooling rate is ensured using controlled cooling and graphite plates to distribute the temperature evenly. For the induction welded specimens, a small section is heated while the remaining laminate is still consolidated. Furthermore, the area that reaches temperatures above $T_m$ is greater at the top surface than at the lower surface. These two characteristics may cause residual stresses that could affect the strength of the parts. It is difficult to either confirm or reject the contribution of residual stresses to the failure strength of the samples. Further investigations are required to determine the exact cause of the lower failure.

The C-scan shows that the induction welded specimens have significant defects within the joint interface. It is expected that this is due to the voids and poor surface quality of the induction welded parts. As the surface quality and voids in the interface region are not likely to be responsible for the lower failure strength, the C-scan results cannot be related to tensile test results.

The resulting failure stresses and stiffnesses of the CV en CT samples equal. Therefore, taking into account the difficult manufacturing process of the continuous scarf specimen, the conventional scarf result in a more efficient joint.

FEM indicates failure similar to the failure seen during tensile testing. However, the model is not able to predict exact failure due to the complex progressive failure of the PPS matrix in between the parts. An indication of the failure strength can be made using DZM for slight alterations within the geometry. To obtain a more accurate prediction of the behavior inside the joints, cohesive damage modeling should be included in the model. Using this method, the progressive failure of the PPS can be modeled.

Finally, no previous research on adhesively bonded or welded scarf or stepped lap joints in CFRTP is conducted to compare to the results of this thesis. There are a number of papers that discuss TPC lap shear joints, both welded and bonded. To compare the scarf and stepped lap joints the normalized shear strength is calculated for all joints. This results in an average shear strength of 31.3 $MPa$ with a standard deviation of 1.1 $MPa$ for the press joined samples and 27.4 $MPa$ with a standard deviation of 4.1 $MPa$ for the induction welded samples. It can be seen in Table 5.15 that shear strengths reached are comparable to the welded Lap Shear Strength (LSS ) mentioned in literature. The adhesive bonded lap shear samples only obtain similar LSS if plasma treatment is applied to the surface. As the machining and vacuum required for plasma treatment is expensive, welding is a very promising option [67, 78, 79].

Table 5.15: LSS for welded and bonded TPC

| Joining Method | LSS | Source |
|---:|:-:|:--|
| Adhesive, no surface preparation | 2-6 $MPa$ | [79–81] |
| Adhesive, sand blasted | 10 $MPa$ | [81] |
| Adhesive, plasma treated | 21-32 $MPa$ | [79, 81] |
| Press joined scarf and stepped lap joints | 27-31 $MPa$ | |
| Welding, (IW, RW, USW) | 27-37 $MPa$ | [46, 76, 82] |

## 5.6. Conclusion

The C-scan shows significant defects in the induction welded specimens whereas the press joint specimens show promising results. The micrography performed on the press joined samples show a bonded joint without flaws apart from a few minor defects. The results of the microscopic analysis of the induction welded samples show a void content of about 2-3%, this is likely caused by insufficient pressure during welding. The CTI samples have not been completely joined along the interface, which might be due to a thin layer of PPS isolating the fibers. The top of the STI parts also experiences a slight gap due to a combination of a lower temperature during welding and two welding runs required to completely join the joint interface. It is expected that during the second welding run for the STI specimen the flow of electricity is redirected towards the already joined section of the specimen. This could reduce the flow of electricity, and therefore the heat generation, in the section of the joint that has not been joined.

DIC and FEM indicate that all joined samples fail at the first step in the joint interface. The press joined samples performed better than the induction welded samples recovering 44.0% for the CVP samples, 43.3% for the CTP samples and 59.4% for the STP samples and the stiffness of the press bonded parts is around 96-99% of the pristine stiffness. The induction welded samples recover 32%, 34%, and 46% of the pristine failure strength for the CVI, CTI, and STI samples respectively. The stiffness is recovered between 92-96% of the pristine stiffness for all induction welded samples. It should be noted that the COV of the induction welded specimens is significantly higher indicating an uniform weld quality along the width of the specimen has not been obtained.

The scarfed parts perform equally well and the stepped lap joint has the best performance. Because the continuous scarfed parts are more difficult to manufacture and show no benefits during welding, a conventional scarf is considered a more efficient repair method. Although none of the parts meet the requirements set for a full recovery, the performance of the welded joints is promising as it is unlikely that a similar recovery can be obtained using adhesives, unless expensive surface treatments are applied.

The FEM analysis does not give an accurate representation of the tensile tests due to the progressive failure of the PPS matrix. To accurately predict the failure loads, cohesive zone modeling should be included in the model. Although the results do not predict the failure load accurately it can be concluded that PPS matrix failure is the likely cause of failure in the joined samples, initiating in the step at the surface of the samples. This corresponds to the failure seen in DIC during tensile testing. Additionally, the FEM indicate that a smaller angle for the scarf joint or a longer overlap for the stepped lap joint would increase failure strength.

# 6

# Conclusion and Recommendation

In the first section the conclusions regarding this thesis are stated. In the second section recommendation on how to expand this research are given.

## 6.1. Conclusion

Although the strength is not recovered up to the set requirements of within 10% of the pristine properties, induction welding has shown to be a promising method for TPC repairs. Three challenges are found during induction welding of CF/PPS. First, to weld the 30 $mm$ wide interface at once, a 65 $mm$ wide coil is needed. This wide coil needs a 70 $mm$ wide gap that needs to be bridged by support plates. Secondly, the support material needs to be stiff at high temperatures, unresponsive to the alternating magnetic field, provide heat isolation and withstand temperatures up to $400°C$. Finally, a significant number of voids was found in the induction welded specimens.

The cyanate ester support plates, although they should have been thicker to provide sufficient resistance against deflection caused by the welding pressure, would have met all requirements according to the manufacturers datasheet. During welding it became clear that the cyanate ester was affected superficially by the high temperatures, although the highest measured temperature, $389°C$, is below the degradation temperature of $420°C$. The voids in the induction welded specimens are likely caused by insufficient pressure during welding.

Measuring the temperature at the interface in between the parts has proven to be difficult without affecting the measured temperature, a good solution has not yet been found. It has also proven difficult to obtain an uniform temperature along the weld-line for the 130 $mm$ wide parts. The three different joint types all require a different welding program. Additionally the stepped lap joint is welded twice, the second run at an offset with respect to the first run, to completely join the joint interface.

Simple analytic approximations have been used to calculate the scarf angle of 4.7° and the stepped lap overlap of 37.8 $mm$. Using this angle the scarfed specimens recover about 44% of the pristine strength and the step lap specimen recovers about 59% of the pristine strength. All joint types are within 92-99% of the pristine stiffness. The induction welded specimens have a failure stress recovery of 34% and 46% for the scarf joint and stepped lap joint samples respectively. This results in an induction welded failure stress of about 73-77% of the press joined specimens. This lower failure stress is attributed to residual stresses due to local heating during induction welding and the initial curvature of 1 $mm$ due to deflection during welding.

DIC and FEM shows that the failure initiates in the PPS matrix in the first step of the scarf or stepped lap joint. FEM also suggests that a smaller angle for the scarf joint or a longer overlap for the stepped lap joint would increase failure strength.

## 6.2. Recommendations

- *Investigate impact of stepless scarf*
  The initial step in the scarf geometry initiates the failure in the tensile test specimens. Milling the CF/PPS to an infinitely thin edge could result in unpredictable behavior. However, the failure stress might still be higher than a scarf with steps at the surface.

- *Optimize repair method before involving induction*
  It is advised to first optimize the repair design before adapting this to induction welding. Research suggest that for a step-less scarf adding a thin layer of PPS between the parts results in a higher recovery strength. This film of PPS will significantly influence the temperatures during IW by restricting the flow between the parts. An over-ply also increases the failure strength for most joints, which would also change the welding process significantly.

- *Investigate possibility to weld the interface in multiple runs*
  If it is possible to weld the parts together one section at a time the coil can be made significantly smaller. This would reduce the distance that the support plates have to bridge. A shorter distance to be bridged allows for thinner support plates, reducing the coupling distance and heating time of the laminate.

- *Extend FEM model to include cohesive damage modeling*
  The DZM method has limited use for the complex failure behavior of the scarf joint. To better analyze the failure of the joint, a cohesive damage model should be implemented in the model.

- *Redesign the pressurization method*
  The method used to pressurize the parts could be the cause of the voids seen in the induction welded specimens. This method should be redesigned to only apply pressure to the section of the specimen which reaches temperatures above $T_m$. This will result in a thicker support plate at the top of the part and thus a larger coupling distance between the coil and the laminate.

# Bibliography

[1] T. J. Ahmed, D. Stavrov, H. E. N. Bersee, and A. Beukers, “Induction Welding of Thermoplastic Composites - An Overview,” *Composites Part A: Applied Science and Manufacturing*, vol. 37, no. 10, pp. 1638–1651, 2006.

[2] R. Goldstein, “Magnetic Flux Controllers in Induction Heating and Melting,” in *ASM Handbook*, vol. 4C, pp. 633–645, 2014.

[3] A. Yousefpour, M. Hojjati, and J. P. Immarigeon, “Fusion Bonding/Welding of Thermoplastic Composites,” *Journal of Thermoplastic Composite Materials*, vol. 17, no. 4, pp. 303–341, 2004.

[4] IITIAN, “Magnetic Flux Density or Magnetic Induction [https://www.askiitians.com/iit-jee-magnetism/magnetic-flux-density-magnetic-induction-magnetic-intensity/] Accessed on 17-03-2018.”

[5] D. Blond, B. Vieille, M. Gomina, and L. Taleb, “Correlation Between Physical Properties, Microstructure and Thermo-Mechanical Behavior of PPS-Based Composites Processed by Stamping,” *Journal of Reinforced Plastics and Composites*, vol. 33, no. 17, pp. 1656–1668, 2014.

[6] ASTM International, “Standard Test Method for Tensile Properties of Polymer Matrix Composite Materials,” 2008.

[7] J. Hale, “Boeing 787 from the Ground Up,” *Boeing Aero Magazin*, vol. 4, pp. 17–23, 2006.

[8] L. Ye, Y. Lu, Z. Su, and G. Meng, “Functionalized Composite Structures for new Generation Airframes: A Review,” *Composites Science and Technology*, vol. 65, no. 9 SPEC. ISS., pp. 1436–1446, 2005.

[9] C. Meola, S. Boccardi, and G. maria Carlomagno, “Composite Materials in the Aeronautical Industry,” in *Infrared Thermography in the Evaluation of Aerospace Composite Materials*, ch. 1, pp. 1–24, 2015.

[10] J. Diaz and L. Rubio, “Developments to Manufacture Structural Aeronautical Parts in Carbon Fibre Reinforced Thermoplastic Materials,” *Journal of Materials Processing Technology*, vol. 143-144, no. 1, pp. 342–346, 2003.

[11] C. Worrall and R. Wise, “Novel Induction Heating Technique for Joining of Carbon Fibre Composites,” in *SEICO 14*, 2014.

[12] I. F. Villegas, L. Moser, A. Yousefpour, P. Mitschang, and H. E. N. Bersee, “Process and Performance Evaluation of Ultrasonic , Induction and Resistance Welding of Advanced Thermoplastic Composites,” *Journal of Thermoplastic Composite Materials*, vol. 26, no. 8, pp. 1007–1024, 2012.

[13] C. Kassapoglou, K. Rangelov, and S. Rangelov, “Repair of Composites : Design Choices Leading to Lower Life-Cycle Cost,” *Applied Composite Materials*, pp. 1–19, 2016.

[14] C. K. Sunar and M. Kaden, “Economical Validation of a New Repair Concept for CF-Thermoplastics By Its Comparison With an Ongoing Repair Process (E.G. CF-Thermosets),” in *15TH European Conference on Composite Materials*, no. June, pp. 24–28, 2012.

[15] C. Ageorges, L. Ye, and M. Hou, “Advances in Fusion Bonding Techniques for Joining Thermoplastic Matrix Composites: A Review,” *Composites Part A: Applied Science and Manufacturing*, vol. 32, no. 6, pp. 839–857, 2001.

[16] Z. Xie, X. Li, and Q. Yan, “Scarf Repair of Composite Laminates,” in *MATEC Web of Conferences*, vol. 61, pp. 4–7, 2016.

[17] U. H. Ahn and G. S. Springer, “Repair of Composite Laminates,” Tech. Rep. December, 2000.

[18] J. Li, Y. Yan, T. Zhang, and Z. Liang, “Experimental Study of Adhesively Bonded CFRP Joints subjected to Tensile Loads,” *International Journal of Adhesion and Adhesives*, vol. 57, pp. 95–104, 2015.

[19] R. D. S. G. Campilho, M. F. S. F. de Moura, A. M. G. Pinto, J. J. L. Morais, and J. J. M. S. Domingues, “Modelling the Tensile Fracture Behaviour of CFRP Scarf Repairs,” *Composites Part B: Engineering*, vol. 40, no. 2, pp. 149–157, 2009.

[20] B. Whittingham, A. A. Baker, A. Harman, and D. Bitton, “Micrographic Studies on Adhesively Bonded Scarf Repairs to Thick Composite Aircraft Structure,” *Composites Part A: Applied Science and Manufacturing*, vol. 40, no. 9, pp. 1419–1432, 2009.

[21] C. H. Wang and A. J. Gunnion, “On the Design Methodology of Scarf Repairs to Composite Laminates,” *Composites Science and Technology*, vol. 68, no. 1, pp. 35–46, 2008.

[22] L. Tong, Q. Le, S. Q. Li, and J. J. Xiong, “Scarfing Repair Parameters Optimization for Composite Laminates,” *Materials Science Forum*, vol. 813, pp. 35–42, 2015.

[23] S. Neilson, A. Orifici, and C. Wang, “Investigation into Optimised Composite Scarf Repairs with Practical Constraints,” in *28th ICAS 2012*, vol. 3, pp. 1–6, 2012.

[24] T. D. Breitzman, E. V. Iarve, B. M. Cook, R. P. Lipton, and B. Rouge, “Optimal Design of a Composite Scarf Repair Patch Under Uniaxial Tension Load,” in *ASME 2009 International Mechanical Engineering Congress and Exposition*, pp. 1–10, 2009.

[25] S. B. Kumar, I. Sridhar, S. Sivashanker, S. O. Osiyemi, and A. Bag, “Tensile Failure of Adhesively Bonded CFRP Composite Scarf Joints,” *Materials Science and Engineering B: Solid-State Materials for Advanced Technology*, vol. 132, no. 1-2, pp. 113–120, 2006.

[26] V. H. Truong, J. S. Yoo, C. H. Kim, M. Y. Park, J. H. Choi, and J. H. Kweon, “Failure Load Prediction of Laminates Repaired with a Scarf-Bonded Patch using the Damage Zone Method,” *Advanced Composite Materials*, vol. 26, no. 2, pp. 115–133, 2017.

[27] T. D. Breitzman, E. V. Iarve, B. M. Cook, G. A. Schoeppner, and R. P. Lipton, “Optimization of a Composite Scarf Repair Patch under Tensile Loading,” *Composites Part A: Applied Science and Manufacturing*, vol. 40, no. 12, pp. 1921–1930, 2009.

[28] C. H. Wang and A. J. Gunnion, “Optimum Shapes of Scarf Repairs,” *Composites Part A: Applied Science and Manufacturing*, vol. 40, no. 9, pp. 1407–1418, 2009.

[29] A. B. Harman and C. H. Wang, “Improved Design Methods for Scarf Repairs to highly Strained Composite Aircraft Structure,” *Composite Structures*, vol. 75, no. 1-4, pp. 132–144, 2006.

[30] H. Bendemra, P. Compston, and P. J. Crothers, “Optimisation Study of Tapered Scarf and Stepped-Lap Joints in Composite Repair Patches,” *Composite Structures*, vol. 130, pp. 1–8, 2015.

[31] A. J. Gunnion and I. Herszberg, “Parametric Study of Scarf Joints in Composite Structures,” *Composite Structures*, vol. 75, no. 1-4, pp. 364–376, 2006.

[32] M. A. Caminero, S. Pavlopoulou, M. Lopez-Pedrosa, B. G. Nicolaisson, C. Pinna, and C. Soutis, “Analysis of Adhesively Bonded Repairs in Composites: Damage Detection and Prognosis,” *Composite Structures*, vol. 95, pp. 500–517, 2013.

[33] S. O. Olajide, E. Kandare, and A. Afaghi Khatibi, “Fatigue Life Uncertainty of Adhesively Bonded Composite Scarf Joints – An Airworthiness Perspective,” *The Journal of Adhesion*, vol. 93, no. 7, pp. 515–530, 2015.

[34] A. Baker, S. Dutton, and K. Donald, “Repair Technology,” *Composite Materials for Aircraft Structures*, pp. 369–402, 2004.

[35] C. H. Wang, V. Venugopal, and L. Peng, "Stepped Flush Repairs for Primary Composite Structures," *The Journal of Adhesion*, vol. 91, no. 1-2, pp. 95–112, 2014.

[36] L. J. Hart-Smith, "Analysis and Design of Advanced Composite Bonded Joints," tech. rep., NASA, 1974.

[37] A. Riccio, R. Ricchiuto, F. Di Caprio, A. Sellitto, and A. Raimondo, "Numerical Investigation of Constitutive Material Models on Bonded Joints in Scarf Repaired Composite Laminates," *Engineering Fracture Mechanics*, vol. 173, pp. 91–106, 2017.

[38] Y. Baig, X. Cheng, H. J. Hasham, M. Abbas, and W. A. Khan, "Failure Mechanisms of Scarf-Repaired Composite Laminates under Tensile Load," *Journal of the Brazilian Society of Mechanical Sciences and Engineering*, vol. 38, no. 7, pp. 2069–2075, 2016.

[39] R. M. Christensen, "A Comprehensive Theory of Yielding and Failure for Isotropic Materials," *Journal of Engineering Materials and Technology*, vol. 129, no. 2, p. 173, 2007.

[40] C. S. Ban, Y. H. Lee, J. H. Choi, and J. H. Kweon, "Strength Prediction of Adhesive Joints using the Modified Damage Zone Theory," *Composite Structures*, vol. 86, no. 1-3, pp. 96–100, 2008.

[41] C. Soutis, "Carbon Fiber Reinforced Plastics in Aircraft Construction," *Materials Science and Engineering A*, vol. 412, no. 1-2, pp. 171–176, 2005.

[42] F. H. Darwish, S. Hamoush, and K. Shivakumar, "Performance of Patch Repaired Composite Panels Under Fatigue Loads," *The Arabian Journal for Science and EngineeringScience*, vol. 31, no. 2, pp. 77–87, 2006.

[43] J. S. Yoo, V. H. Truong, M. Y. Park, J. H. Choi, and J. H. Kweon, "Parametric Study on Static and Fatigue Strength Recovery of Scarf Patch Repaired Composite Laminates," *Composite Structures*, vol. 140, pp. 417–432, 2016.

[44] M. J. Van Wijngaarden, "Welding Technologies for a Generic Carbon Fiber Reinforced Thermoplastic Assembly," in *25th Internation SAMPE Conference*, pp. 55–60, 2004.

[45] L. Ye, Z. R. Chen, M. Lu, and M. Hou, "De-Consolidation and Re-Consolidation in CF/PPS Thermoplastic Matrix Composites," *Composites Part A: Applied Science and Manufacturing*, vol. 36, no. 7, pp. 915–922, 2005.

[46] P. G. O'Shaughnessey, M. Dubé, and I. F. F. Villegas, "Modeling and Experimental Investigation of Induction Welding of Thermoplastic Composites and Comparison with other Welding Processes," *Journal of Composite Materials*, vol. 21, pp. 2895–2910, 2016.

[47] T. Bayerl, M. Duhovic, P. Mitschang, and D. Bhattacharyya, "The Heating of Polymer Composites by Electromagnetic Induction - A Review," *Composites Part A: Applied Science and Manufacturing*, vol. 57, no. 2014, pp. 27–40, 2013.

[48] S. Pappadà, A. Salomi, J. Montanaro, A. Passaro, A. Caruso, and A. Maffezzoli, "Fabrication of a Thermoplastic Matrix Composite Stiffened Panel by Induction Welding," *Aerospace Science and Technology*, vol. 43, pp. 314–320, 2015.

[49] P. Mitschang, R. Rudolf, and M. Neitzel, "Composite Materials Continuous Induction Welding Process, Modelling and Realisation," *Journal of Thermoplastic Composite Materials*, vol. 15, no. March, pp. 127–27, 2002.

[50] M. J. van Wijngaarden, "Implementation of Induction Welding for Thermoplastic Aerospace Structures," in *SEICO 09*, pp. 39–46, 2009.

[51] R. Rudolf, P. Mitschang, and M. Neitzel, "Induction Heating of Continuous Carbon-Fibre-Reinforced Thermoplastics," *Composites Part A: Applied Science and Manufacturing*, vol. 31, no. 11, pp. 1191–1202, 2000.

[52] S. Yarlagadda, H. J. Kim, J. W. Gillespie, N. Shevchenko, and B. K. Fink, "Heating Mechanisms in Induction Processing of Carbon Fiber Reinforced Thermoplastic Prepreg," in *65th SAMPE*, pp. 79–89, 2000.

[53] M. Duhovic, J. Hausmann, P. L. Eplattenier, and I. Caldichoury, "A Finite Element Investigation into the Continuous Induction Welding of Dissimilar Material Joints," in *10th European LS-DYNA Conference*, p. 11, 2015.

[54] A. P. da Costa, E. C. Botelho, M. L. Costa, N. E. Narita, and J. R. Tarpani, "A Review of Welding Technologies for Thermoplastic Composites in Aerospace Applications," *Journal of Aerospace Technology and Management*, vol. 4, no. 3, pp. 255–265, 2012.

[55] F. Lionetto, S. Pappadà, G. Buccoliero, and A. Maffezzoli, "Finite Element Modeling of Continuous Induction Welding of Thermoplastic Matrix Composites," *Materials & Design*, vol. 120, no. 120, pp. 212–221, 2017.

[56] F. Lundström, K. Frogner, O. Wiberg, T. Cedell, and M. Andersson, "Induction Geating of Carbon Fiber Composites: Investigation of Electrical and Thermal Properties," *International Journal of Adhesion and Electromagnetics and Mechanics*, vol. 53, pp. 21–30, 2017.

[57] S. Yarlagadda, H. J. Kim, J. W. Gillespie Jr, N. B. Shevchenko, and B. K. Fink, "A Study on the Induction Heating of Conductive Fiber Reinforced Composites," *Journal of Composite Materials*, vol. 36, no. 4, pp. 401–421, 2002.

[58] B. K. Fink, R. L. Mccullough, and J. W. Gillespie, "Induction Heating of Carbon-Fiber Composites: Experimental Verification of Models," Tech. Rep. June, 2000.

[59] B. K. Fink, R. L. McCullough, and J. W. Gillespie, "A Local Theory of Heating in Cross Ply Carbon Fiber Thermoplastic Composites by Magnetic Induction," *Polymer Engineering & Science*, vol. 32, no. 5, pp. 357–369, 1992.

[60] B. K. Fink, R. L. McCullough, and J. W. Gillespie, "A Model to Predict the Through-Thickness Distribution of Heat Generation in Cross-Ply Carbon-Fiber Composites subjected to Alternating Magnetic Fields," *Composites Science and Technology*, vol. 55, no. 2, pp. 119–130, 1995.

[61] B. K. Fink, R. L. Mccullough, and J. W. Gillespie, "Experimental Verification of Models for Induction Heating of Continuous-Carbon-Fiber Composites," *Polymer Composites*, vol. 17, no. 2, pp. 198–12, 1996.

[62] S. Zinn and S. L. Semiatin, "Coil Design and Fabrication: Basic Design and Modifications," in *Elements of Induction Heating*, no. June, pp. 32–41, 1988.

[63] S. Pappada, A. Salomi, J. Montanaro, R. Angiuli, A. Passaro, A. Caruso, and A. Maffezzoli, "Induction Welding of PPS-Carbon Composites: Modeling and Experimental Results," in *ICCM 19*, pp. 5481–5488, 2013.

[64] H. J. Kim, S. Yarlagadda, N. B. Shevchenko, B. K. Fink, and J. W. Gillespie, "Development of a Numerical Model to Predict In-Plane Heat Generation Patterns During Induction Processing of Carbon Fiber-Reinforced Prepreg Stacks," *Journal of Composite Materials*, vol. 37, no. 16, pp. 1461–23, 2003.

[65] R. Anderson, R. Adams, and B. Duggins, "Limitations of Thermocouples in Temperature Measurements," in *25th ISA Anaheim CA*, p. 33, 1979.

[66] J. L. Horton, T. G. Kollie, and L. G. Rubin, "Measurement of B versus H of Alumel from 25 to 180C," *Journal of Applied Physics*, vol. 48, no. 11, pp. 4666–4671, 1977.

[67] K. B. Katnam, L. F. M. Da Silva, and T. M. Young, "Bonded Repair of Composite Aircraft Structures: A Review of Scientific Challenges and Opportunities," *Progress in Aerospace Sciences*, vol. 61, pp. 26–42, 2013.

[68] K. Diamanti and C. Soutis, "Structural Health Monitoring Techniques for Aircraft Composite Structures," *Progress in Aerospace Sciences*, vol. 46, no. 8, pp. 342–352, 2010.

[69] S. Gholizadeh, "A Review of Non-Destructive Testing of Composite Materials," in *Procedia Structural Integrity*, vol. 1, pp. 50–57, Elsevier B.V., 2016.

[70] TenCate, "Product Datasheet TenCate Cetex TC1000 PPS resin system," 2014.

[71] Bearingworks, "PPS ( Polyphenylene Sulfide )."

[72] Lonza, "Primaset ™ Cyanate Ester Resins Leading Edge High Performance Thermoset Resins Product Manual," 2012.

[73] G. Montaudo, C. Puglisi, and F. Samperi, "Primary Thermal Degradation Processes Occurring in Poly(phenylenesulfide) Investigated by Direct Pyrolysis-Mass Spectrometry," *Journal of Polymer Science: Part A: Polymer Chemestry*, vol. 32, pp. 1807–1815, 1994.

[74] O. A. Peters and R. H. Still, "The Thermal Degradation of Poly(phenylene Sulphide) - Part 1," *Polymer Degradation and Stability*, vol. 42, pp. 41–48, 1993.

[75] D. Q. Chang, J. X. Liu, N. Mao, and B. Z. Chen, "Study on the Thermal Stability of Polyphenylene Sulfide Filter Media by Non-Isothermal Thermogravimetry," *Advanced Materials Research*, vol. 663, pp. 988–992, 2013.

[76] D. Tanabe, K. Nishiyabu, T. Kurashiki, E. F. Joining, S. C. Fiber, and H. Element, "Electro Fusion Joining of Carbon Fiber Reinforced Thermoplastic Composites Using Carbon Fiber Heating Element," no. June, pp. 22–26, 2014.

[77] I. De Baere, S. Jacques, W. Van Paepegem, and J. Degrieck, "Study of the Mode I and Mode II Interlaminar Behaviour of a Carbon Fabric Reinforced Thermoplastic," *Polymer Testing*, vol. 31, no. 2, pp. 322–332, 2012.

[78] D. Xu, B. Liu, G. Zhang, S. Long, X. Wang, and J. Yang, "Effect of Air Plasma Treatment on Interfacial Shear Strength of Carbon Fiber-Reinforced Polyphenylene Sulfide," *High Performance Polymers*, vol. 28, no. 4, pp. 411–424, 2016.

[79] H. M. S. Iqbal, S. Bhowmik, and R. Benedictus, "Surface Modification of High Performance Polymers by Atmospheric Pressure Plasma and Failure Mechanism of Adhesive Bonded Joints," *International Journal of Adhesion and Adhesives*, vol. 30, no. 6, pp. 418–424, 2010.

[80] S. Genna, C. Leone, N. Ucciardello, and M. Giuliani, "Increasing Adhesive Bonding of Carbon Fiber Reinforced Thermoplastic Matrix by Laser Surface Treatment," 2017.

[81] P. Davies, W. J. Cantwell, P. Y. Jar, P. E. Bourban, V. Zysman, and H. H. Kausch, "Joining and Repair of a Carbon Fibre-Reinforced Thermoplastic," *Composites*, vol. 22, no. 6, pp. 425–431, 1991.

[82] I. F. Villegas and G. Palardy, "Ultrasonic Welding of CF/PPS Composites with Integrated Triangular Energy Directors: Melting, Flow and Weld Strength Development," *Composite Interfaces*, vol. 24, no. 5, pp. 515–528, 2017.

# A

# Joint Geometry Overview

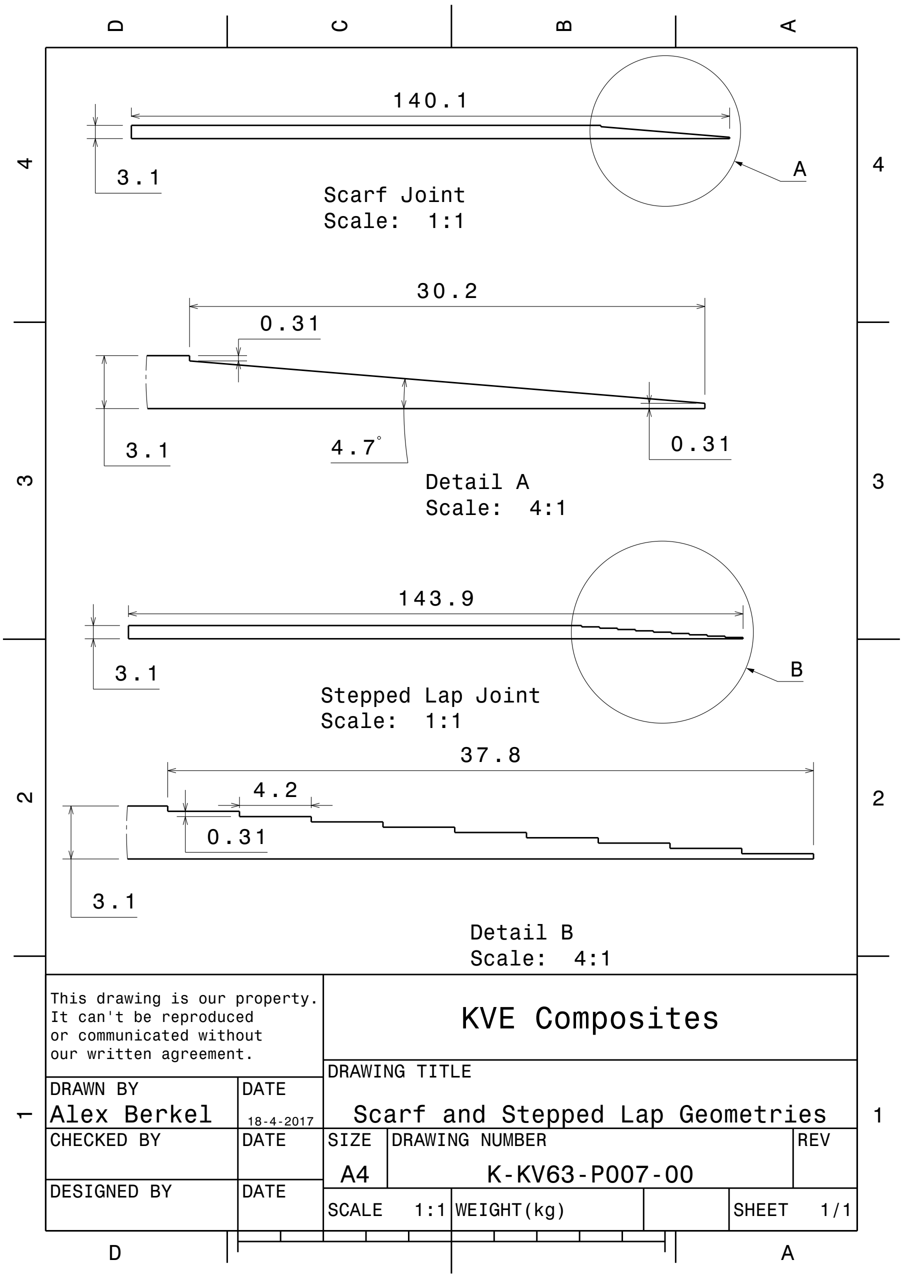

# B

# ANSYS Induction Heating Model

An ANSYS mechanical APDL model used to simulate induction heating in CF reinforced plastics is available at KVE Composites. This model contains the laminate, coil, surrounding air, and heat-sinks if applicable. First the Joule heating inside the laminate is calculated when a alternating current is applied to the coil. This heating is taken as input for a transient thermal analysis to predict the heating of the laminate. The method used is a full FEM/FEM analysis, as opposed to a BEM/FEM analysis which calculates the effect of the electro magnetic field on the boundary of the laminate consequently the model cannot easily simulate moving coils. Two different models are created in APDL, one pristine laminate used to see the behavior of the coil and a fully modeled scarf joint.

## B.1. Validation of the Scarf Joint

The scarf model that is simulated in ANSYS APDL contains two additional effects that may result in unrealistic results. The area of interest, the scarf interface, is essentially an edge and could induce an edge effect. It is unknown whether the model realistically simulates the edge effect. The second effect is the result of the unknown contact resistance between the two parts. If the contact between the parts is perfect and the resistance between the two parts is negligible the two parts will behave as an uncut panel. This will also mean that the edge effect will cease to exist on the interface. Alternatively if the contact resistance between the two parts is very high there will be no flow between the two parts and the heating will be very depended on the edge effect.

Two different models are simulated and compared to the measurements. The first model simulates an uncut pristine laminate and the second model consists of two CNC milled parts with a 0.1 $mm$ thin layer of PPS inbetween to restrict the flow of electricity between the parts. Both models have a 3 $mm$ thick layer of silicon on the top and bottom of the laminate, in addition a 4.35 $mm$ thick GF/Epoxy plate is placed on top of the laminate and a 5.35 $mm$ thick GF/Epoxy plate is placed underneath the laminate. These GF plates support the parts when pressure is applied and the silicon acts as a heat shield to prevent deformations of the GF/Epoxy plates. The coil is placed 0.5 $mm$ above the top support plate, resulting in a total height above the surface of the laminate of 7.85 $mm$. This geometry is shown in Figure B.1 for the CNC milled model.

A static measurement is performed on two conventional CNC milled scarfed parts at an amperage of 200 $A$ for 10 seconds. Five thermocouples are placed on the laminate, located as shown in Figure B.2. The results of this simulation are listed in Table B.1. It can be seen that both the CNC model and the pristine model do not approach the measured values. As concluded in Section 4.3 there is a flow of electricity between the parts that is greater than if the parts were isolated and smaller than the flow of electricity in a pristine specimen. In this model the flow of electricity between the parts is restricted by a thin layer of PPS in between the parts. Creating a new model for CNC milled specimen and determining amount of electricity that flows between the parts is considered beyond the scope of this thesis and it is decided to determine the coil parameters without the use of a scarfed FEM model to predict the heating of the laminate.

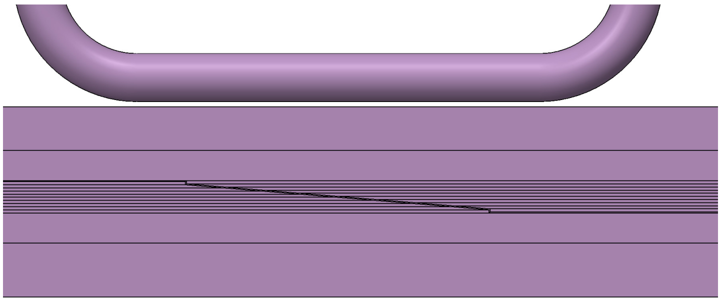

Figure B.1: The laminate as modeled in Ansys APDL with a thin layer of PPS in between the parts. Adjacent to the laminate are the silicon layers, adjoining the GF/epoxy support plates.

Table B.1: Validation of the scarf joint

| Property | Measured | ANSYS CNC | ANSYS pristine | |
|---|---|---|---|---|
| $Tc_1$ | 79.9 | 32.7 | 28.5 | $^{\circ}C$ |
| $Tc_2$ | 59.4 | 38.7 | 61.7 | $^{\circ}C$ |
| $Tc_3$ | 50.3 | 28.2 | 28.7 | $^{\circ}C$ |
| $Tc_4$ | 67.1 | 39.2 | 61.0 | $^{\circ}C$ |
| $Tc_5$ | 91.4 | 35.8 | 56.3 | $^{\circ}C$ |

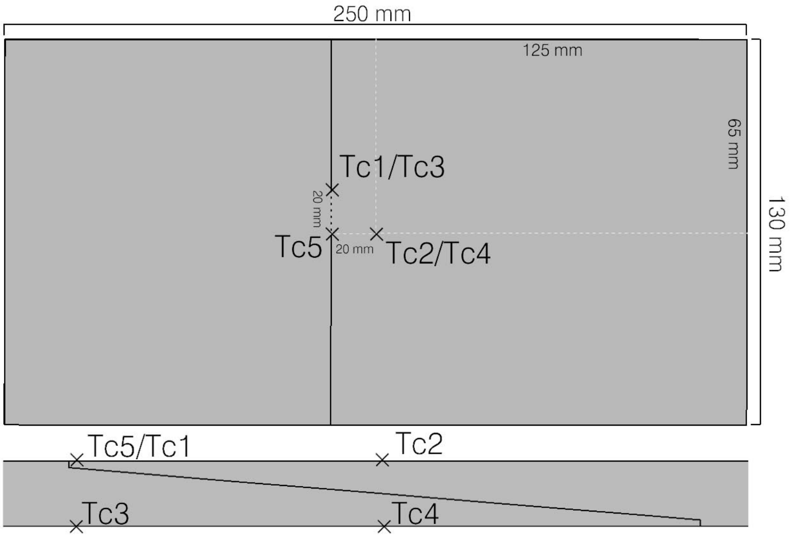

Figure B.2: Thermocouple locations for the static validation

## B.2. Coil Angle

A validated model using a pristine laminate is used to investigated the behavior of a coil placed at different angles with respect to the surface of the laminate. Though the scarfed specimens will likely react different, this model gives an indication on what heating pattern to expect. The results of a varying coil angle with respect to the surface of the laminate are shown in Figures B.3 to B.5. The simulations are run at the same amperage and frequency with a varying weld duration to obtain a maximum temperature of about 300$^{\circ}C$. It can be seen that a increased angle with respect to the surface of the laminate does not change the size of the area that is heated, but does increase time needed to reach a temperature of around 300 $^{\circ}C$.

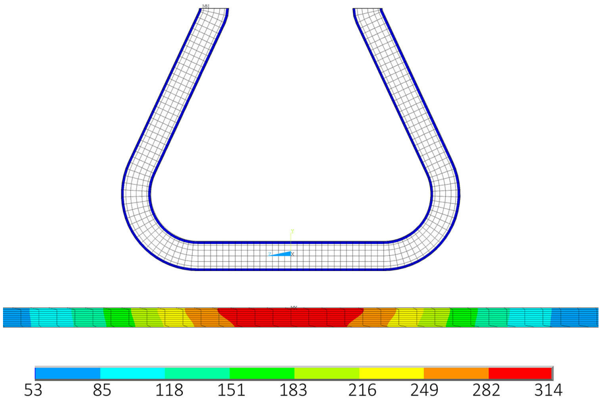

Figure B.3: Heating a 0 degree coil at 300$A$ 350 $kHz$ and 50 $s$

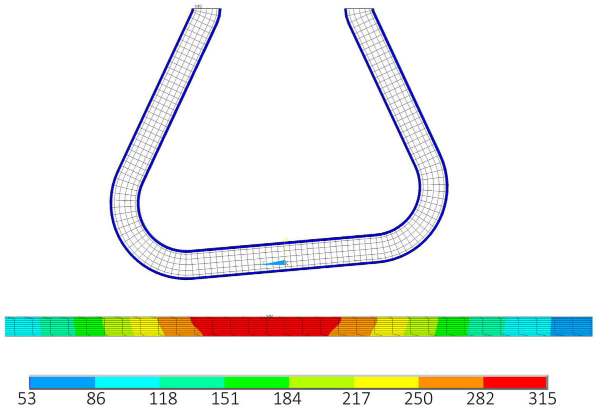

Figure B.4: Heating a 5 degree coil at 300$A$ 350 $kHz$ and 70 $s$

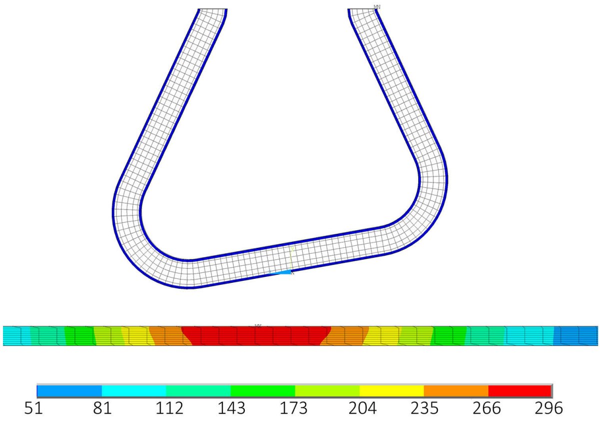

Figure B.5: Heating a 10 degree coil at 300$A$ 350 $kHz$ and 80 $s$

# C

# Coil Dimensions

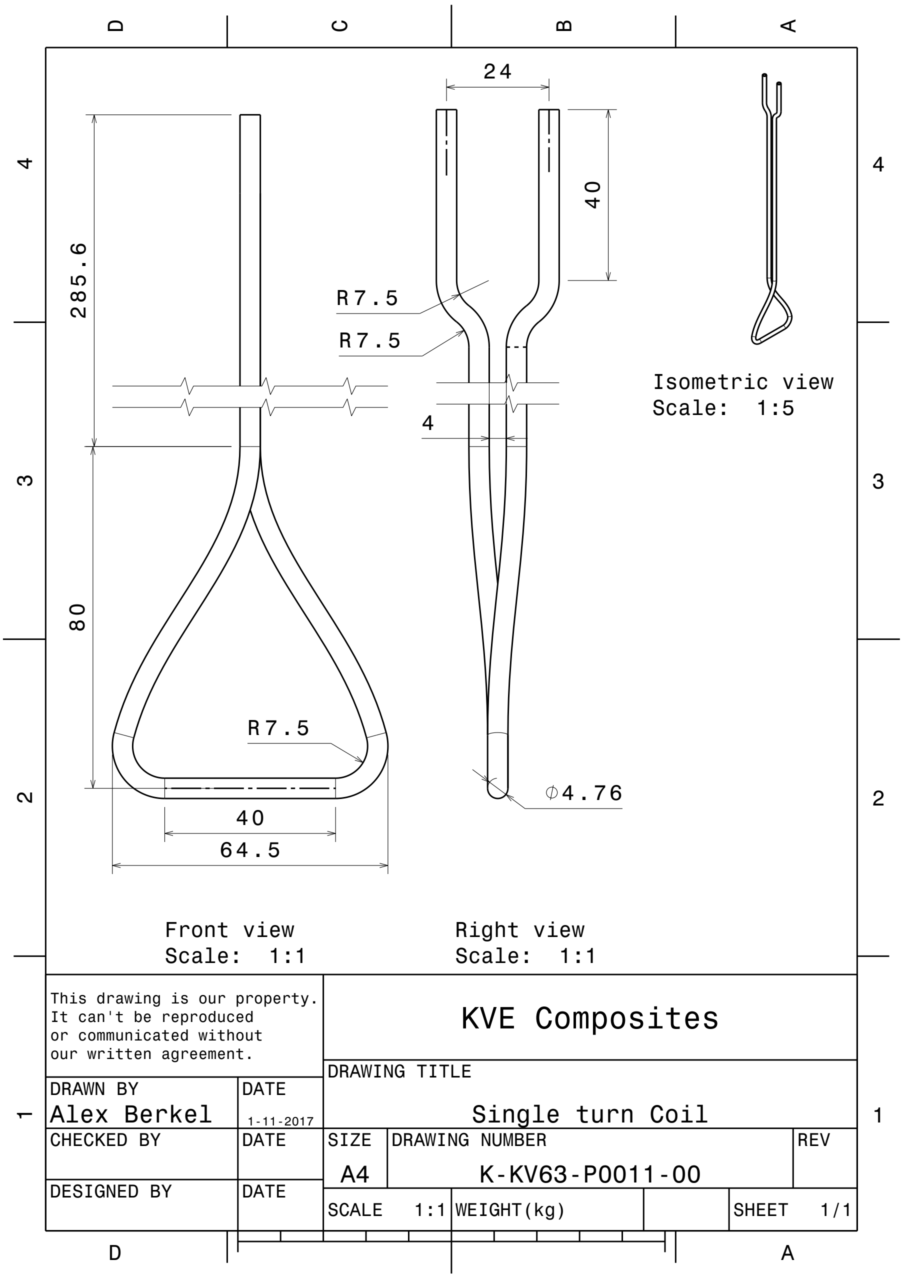

This drawing is our property.
It can't be reproduced
or communicated without
our written agreement.

KVE Composites

DRAWING TITLE
Single turn Coil

DRAWN BY: Alex Berkel
DATE: 1-11-2017
CHECKED BY
DATE
DESIGNED BY
DATE
SIZE: A4
DRAWING NUMBER: K-KV63-P0011-00
REV
SCALE 1:1
WEIGHT(kg)
SHEET 1/1

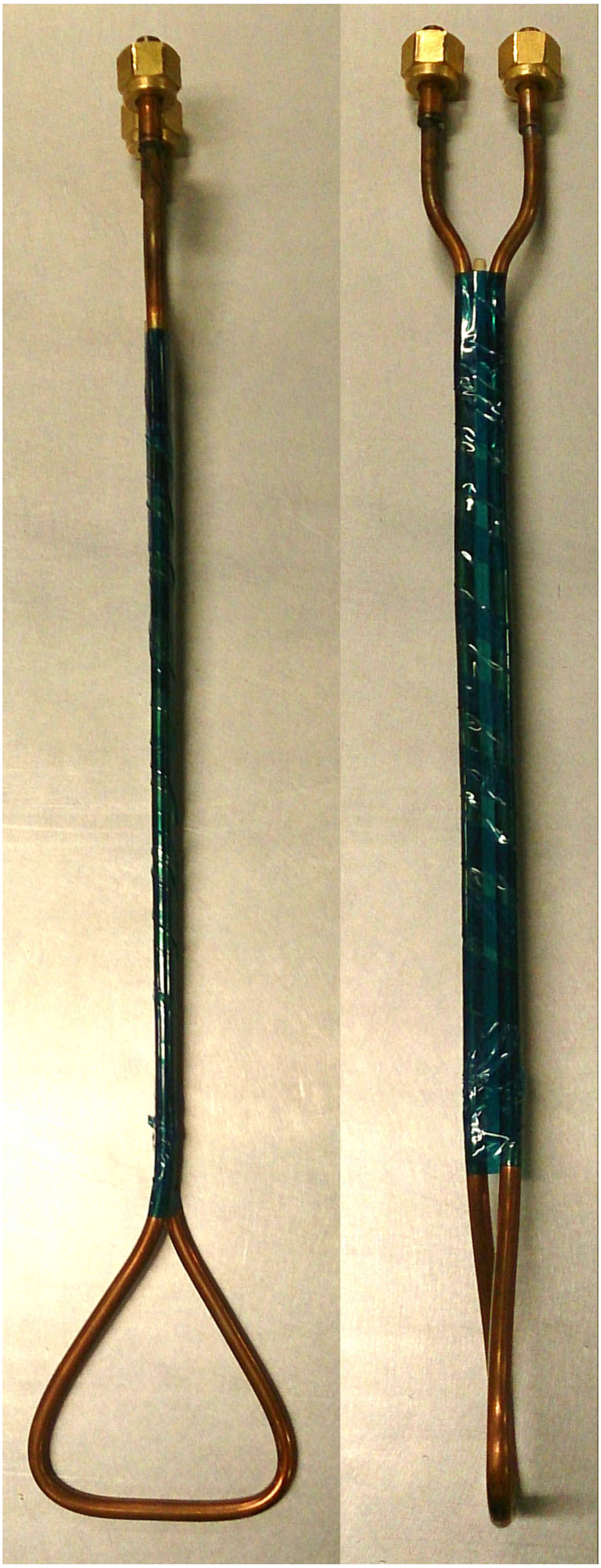

Figure C.1: A picture of the produced coil

# D

# Influence of the Thickness on Strength

The continuous scarf and press joined parts have a lower thickness than the panels consolidated by TenCate due to squeeze-flow. To quantify the influence of the lower thickness, a 250 by 130 $mm$ section of the supplied panels is placed in the Joos Press at the TU Delft and pressed at 320°$C$ and 10 $bar$. Due to a limited amount of available material, the 90° direction of the fibers is placed along the length of the test samples. As it is a woven material and a simple lay-up, $[(0/90)_5]_s$, the failure strength should only be 3 $MPa$ lower than the samples with the 0° direction aligning with the lengthwise direction of the tensile test samples.

Three tensile test specimens are cut from the thin part and marked $T90-T1$, $T90-T2$, and $T90-T3$. Three normal specimens are cut from the original panel which is 3.1 $mm$ thick, these specimens are marked $N90-T1$, $N90-T2$, $N90-T3$. All six specimens are tested according to ASTM D3039, their dimensions and the test results are listed in Table D.1. The failure mode is listed in the table using a three letter abbreviation, the explanation for these abbreviation is given in Figure D.1. The stiffnesses are calculated using the stresses at 0.2% and 0.5% strain.

As confirmed using a z-test the failure stresses of the normal thickness laminate are significantly different from the failure stresses of the thinner laminate. The thinner laminate, being 9.4% thinner than the normal laminate, has a $\sigma_{max}$ which is 13% higher. To be able to compare the different samples, the stress and stiffness is normalized using the thickness of the $N90$ samples. This $\frac{t}{t_{ref}}$ ratio is also shown in Table D.1 as are the normalized stress and stiffness.

It can be seen that the values, once normalized, are similar. The significant similarity is shown using a z-test resulting in probabilities of 66% for the stress and 51% for the stiffness. As such all stresses and stiffness used to compare the specimens will be normalized using the thickness.

Table D.1: Dimensions of the six specimens

| ID | $w_0$ | $t_0$ | $F_{max}$ | $\sigma_{max}$ | $\varepsilon_{F_{max}}$ | $E$ | $\frac{t}{t_{ref}}$ | $\sigma_{max\,norm}$ | $E_{norm}$ | Failure |
|---|---|---|---|---|---|---|---|---|---|---|
| | $[mm]$ | $[mm]$ | $[N]$ | $[MPa]$ | $[-]$ | $[GPa]$ | $[-]$ | $[MPa]$ | $[GPa]$ | |
| $N90-T1$ | 25,44 | 3.15 | 65339 | 815 | 0.0161 | 55.34 | 1 | 815 | 55.34 | LIB |
| $N90-T2$ | 25,46 | 3.15 | 62325 | 777 | 0.0144 | 55.63 | 1 | 777 | 55.63 | SIB |
| $N90-T3$ | 25,46 | 3.15 | 58015 | 723 | 0.0132 | 55.49 | 1 | 723 | 55.49 | LAB |
| $T90-T1$ | 25,54 | 2.85 | 64817 | 892 | 0.0150 | 61.31 | 0.90 | 806 | 55.18 | LWM |
| $T90-T2$ | 25,49 | 2.81 | 61687 | 860 | 0.0140 | 62.34 | 0.89 | 768 | 55.48 | AWM |
| $T90-T3$ | 25,49 | 2.80 | 62288 | 873 | 0.0144 | 62.45 | 0.89 | 776 | 55.58 | LWM |

Table D.2: Weibull distribution for the thin and thick specimens

| | $t_0$ | | $F_{max}$ | | $\sigma_{max\,norm}$ | | $E_{norm}$ | |
|---|---|---|---|---|---|---|---|---|
| | $N90$ | $T90$ | $N90$ | $T90$ | $N90$ | $T90$ | $N90$ | $T90$ |
| | $[mm]$ | $[mm]$ | $[N]$ | $[N]$ | $MPa$ | $MPa$ | $[GPa]$ | $[GPa]$ |
| $\bar{x}$ | 3.15 | 2.82 | 61893 | 62931 | 772 | 783 | 55.49 | 55.41 |
| $s$ | 0 | 0.03 | 368 | 166 | 46 | 20 | 0.15 | 0.21 |
| $COV$ | 0% | 0.94% | 5.95% | 2.64% | 5.99% | 2.56% | 0.26% | 0.38% |

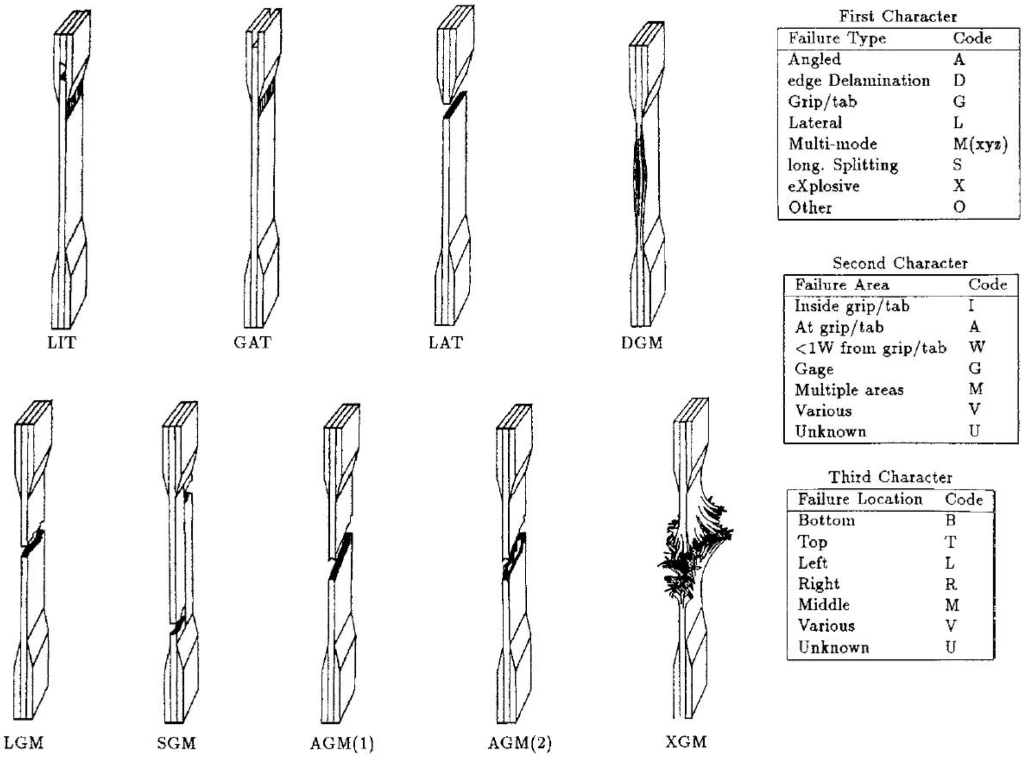

First Character

| Failure Type | Code |
|---|---|
| Angled | A |
| edge Delamination | D |
| Grip/tab | G |
| Lateral | L |
| Multi-mode | M(xyz) |
| long. Splitting | S |
| eXplosive | X |
| Other | O |

Second Character

| Failure Area | Code |
|---|---|
| Inside grip/tab | I |
| At grip/tab | A |
| <1W from grip/tab | W |
| Gage | G |
| Multiple areas | M |
| Various | V |
| Unknown | U |

Third Character

| Failure Location | Code |
|---|---|
| Bottom | B |
| Top | T |
| Left | L |
| Right | R |
| Middle | M |
| Various | V |
| Unknown | U |

Figure D.1: Failure mode identification as given in the ASTM D3039 regulations [6]

# E

# Interface Temperature Results

The results of the experiments regarding the interface temperature are listed in this appendix. In Table E.1 the results of the preliminary interface test with three thermocouples placed along the top surface are shown. For the first experiment the parts are placed in the pressure frame and pressurized without anything in between the two parts. For the second experiment the interface in between the parts is isolate with polyimide tape. It can be seen that both the temperatures and the temperature distribution along the top surface is different.

Following this preliminary experiment, grooves are milled in the scarfed parts in which thermocouples are placed. Doing so ensures propper contact between the two parts while a temperature measure of the interface is still possible. To investigate the impact on the temperatures four termocouples are placed on the top and bottom surface and at least three experimens are performed with and without the grooved parts. A statistical z-test is used determine whether the resulting temperatures can be considered the same. This z-test gives an probability and if the probability is higher tan 5% the results are considered the same. As can be seen in Table E.2 at least three out of four thermocouples placed on the surfaces of the specimens result in a significantly different temperature.

Table E.1: Comparison between temperatures measured for an isolated and non-isolated interface

| | No interface isolation | Interface isolated |
|---|---:|---:|
| $TC_1$ | 108°$C$ | 86°$C$ |
| $TC_2$ | 140°$C$ | 176°$C$ |
| $TC_3$ | 183°$C$ | 97°$C$ |

Table E.2: Probability of the interface measurements being an extreme value of the non-interface measurements tests

| | $TC_{tip\ top}$ | $TC_{mid\ top}$ | $TC_{mid\ bot}$ | $TC_{tip\ bot}$ |
|---|---:|---:|---:|---:|
| CVI | 80.8% | 0% | 0% | 0% |
| STI | 0% | 0% | 52.4% | 0% |
| CTI | 0% | 0% | 0.4% | 0% |

# F

# C-scan

## F.1. Press Joined

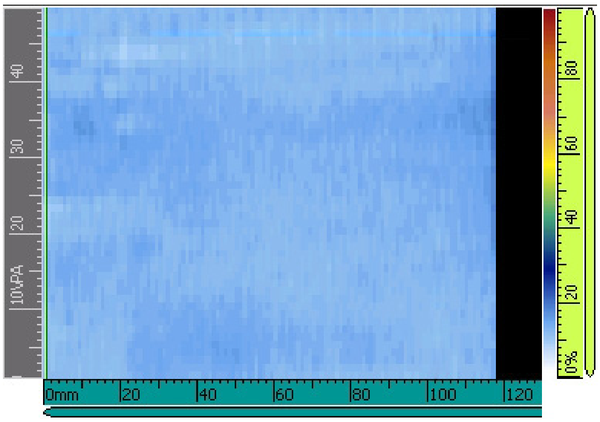

Figure F.1: Return percentages for the A gate for the CVP specimen

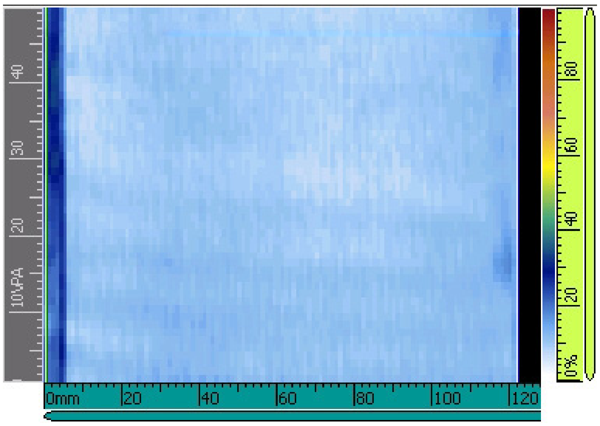

Figure F.2: Return percentages for the A gate for the CTP specimen

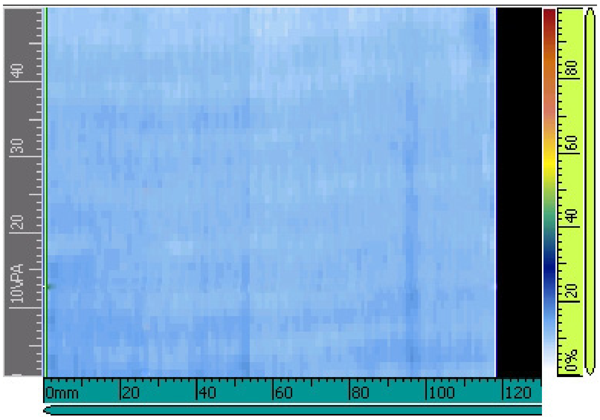

Figure F.3: Return percentages for the A gate for the STP specimen

## F.2. Induction Welded

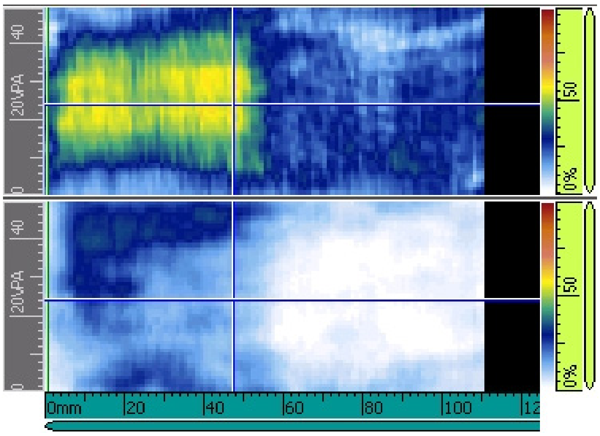

Figure F.4: Return percentages for the A gate (top) and B gate (bottom) for the CVI specimen

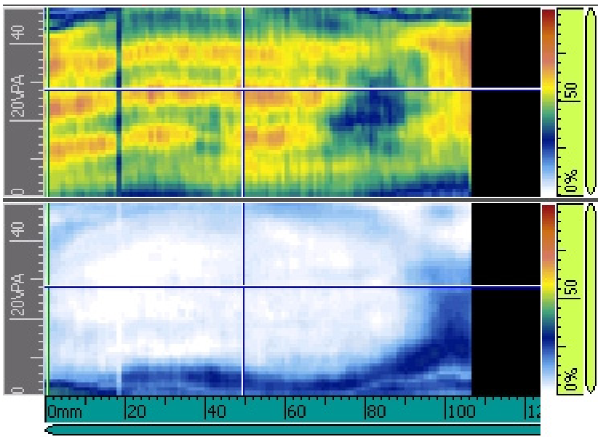

Figure F.5: Return percentages for the A gate (top) and B gate (bottom) for the CTI specimen

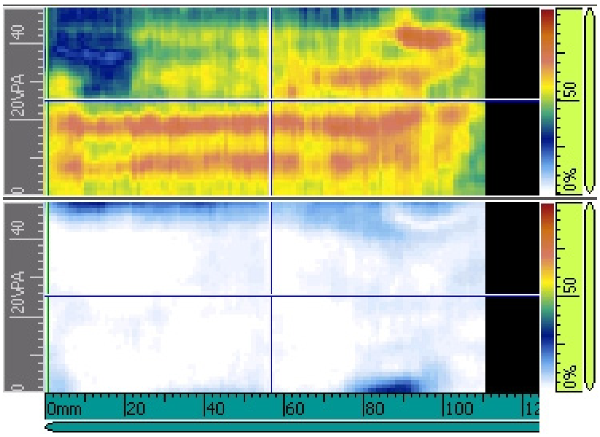

Figure F.6: Return percentages for the A gate (top) and B gate (bottom) for the STI specimen

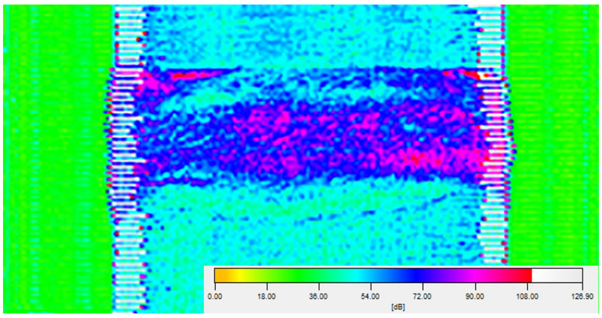

Figure F.7: Through transmitted signal for the transmission C-scan of the STI specimen

# G

# Micrography

## G.1. Continuous Scarf Specimens

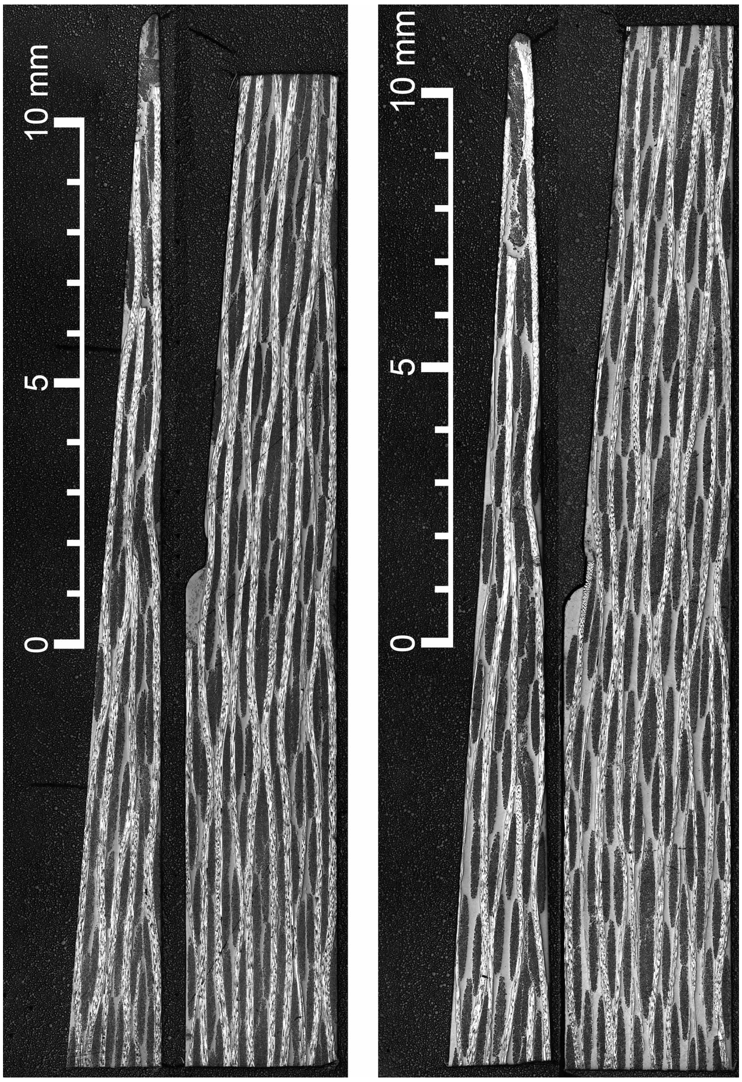

Figure G.1: Micrography of the CTI-2 (left) and CTP-2 (right) samples

## G.2. Press Joined

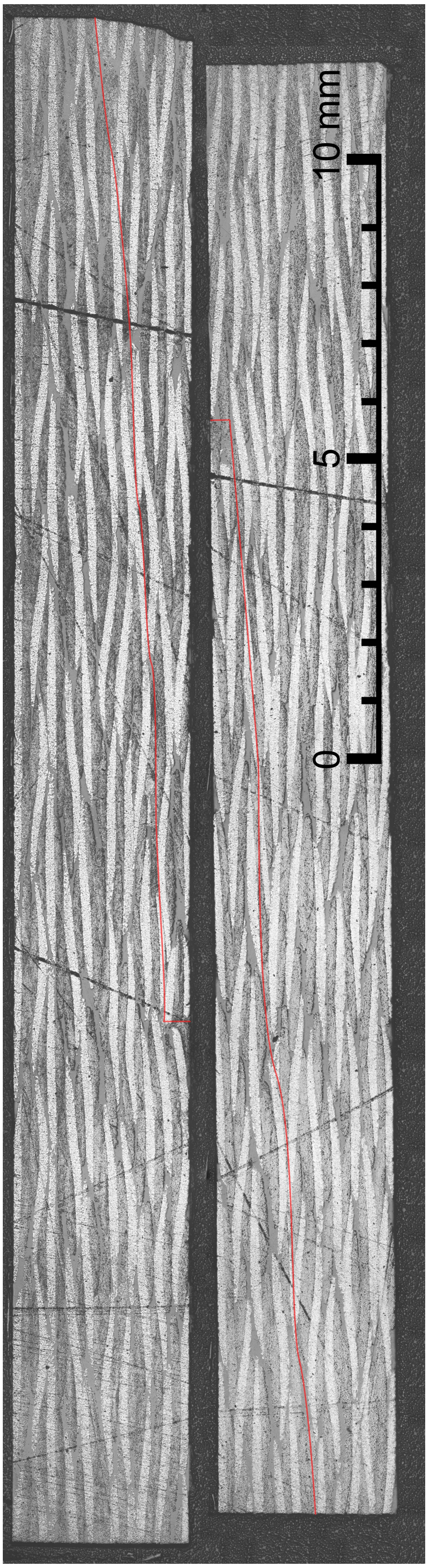

Figure G.2: Micrography of the CVP specimen, interface indicated by the red line

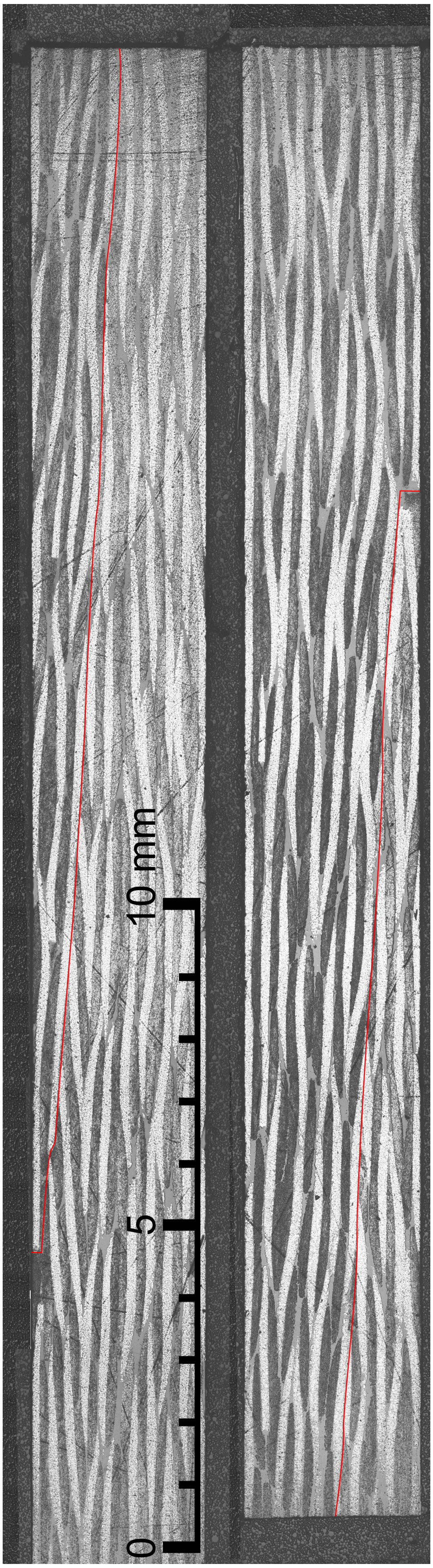

Figure G.3: Micrography of the CTP specimen, interface indicated by the red line

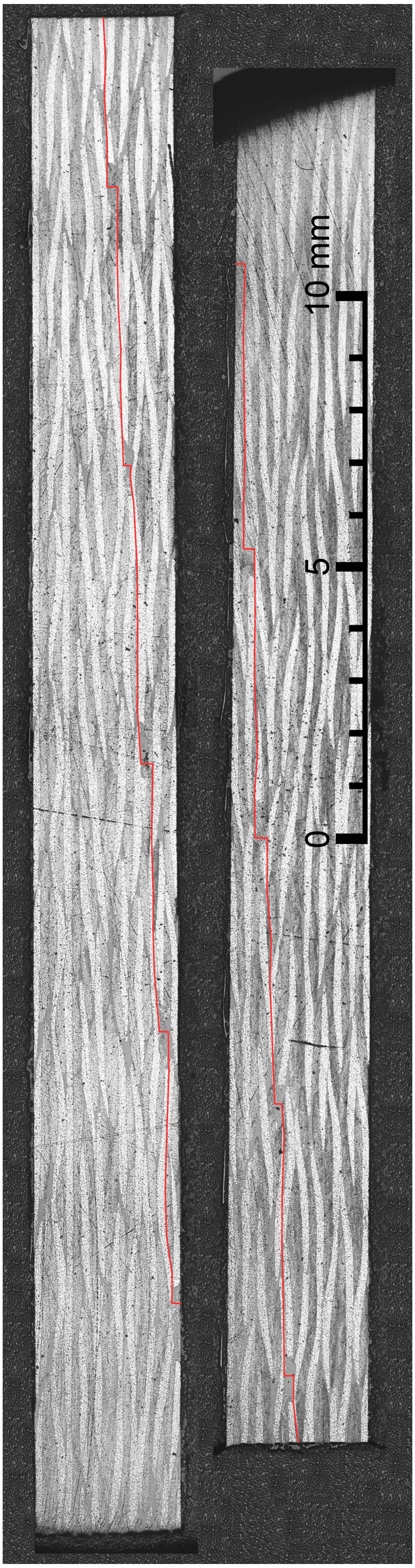

Figure G.4: Micrography of the STP specimen, interface indicated by the red line

## G.3. Induction Welded Specimens

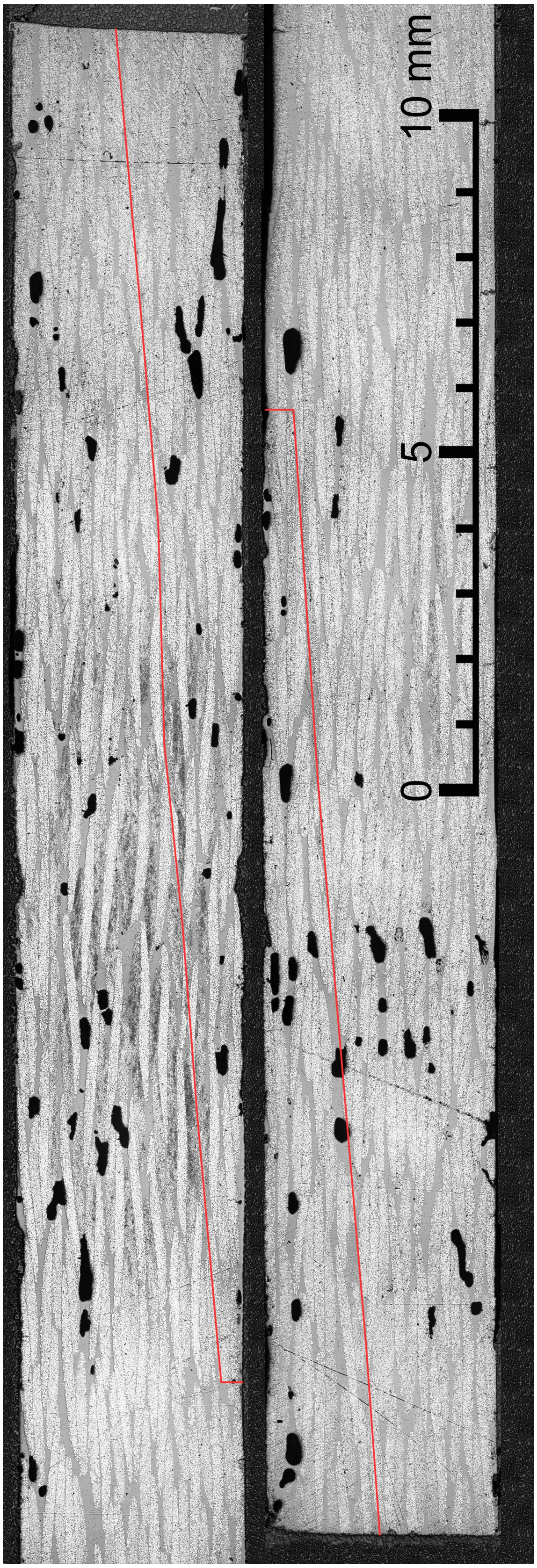

Figure G.5: Micrography of the CVI-M1 sample, interface indicated by the red line

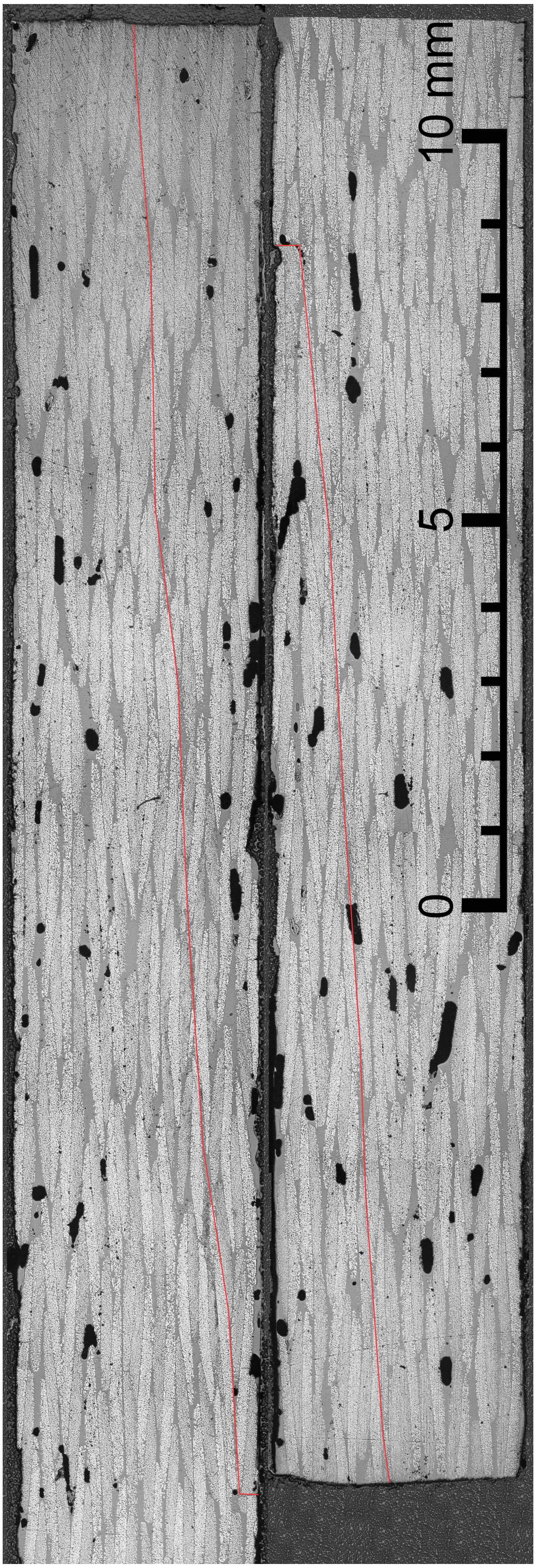

Figure G.6: Micrography of the CVI-M2 sample, interface indicated by the red line

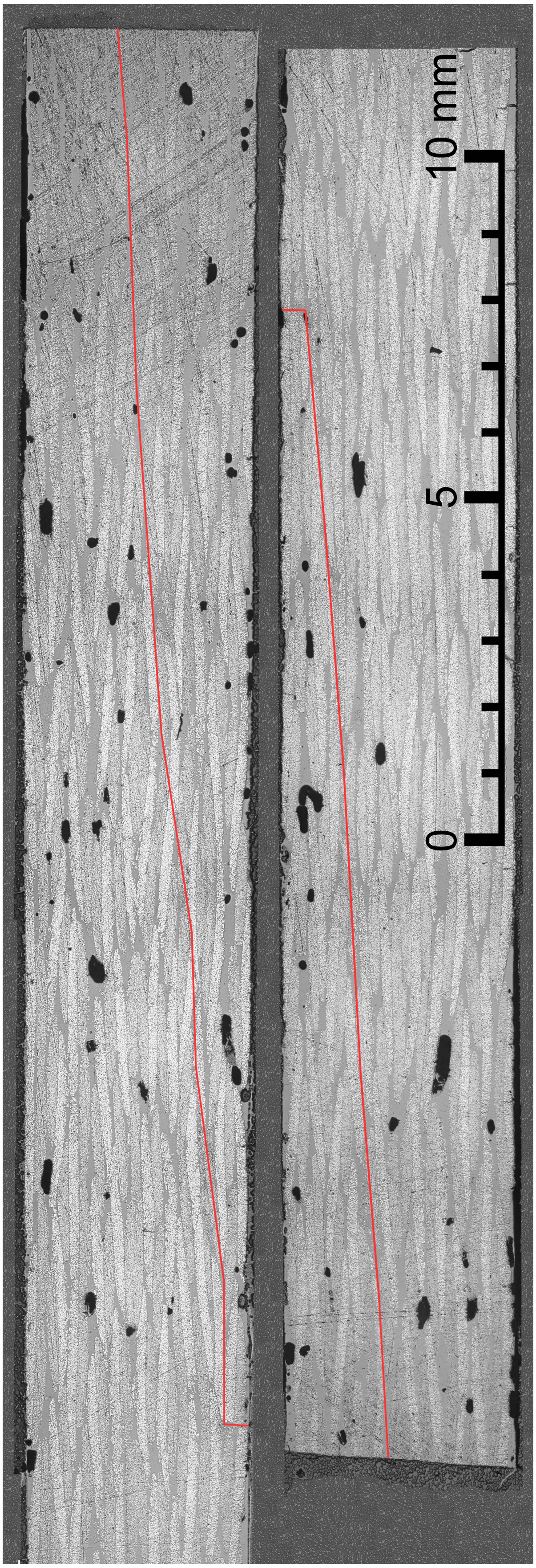

Figure G.7: Micrography of the CVI-M3 sample, interface indicated by the red line

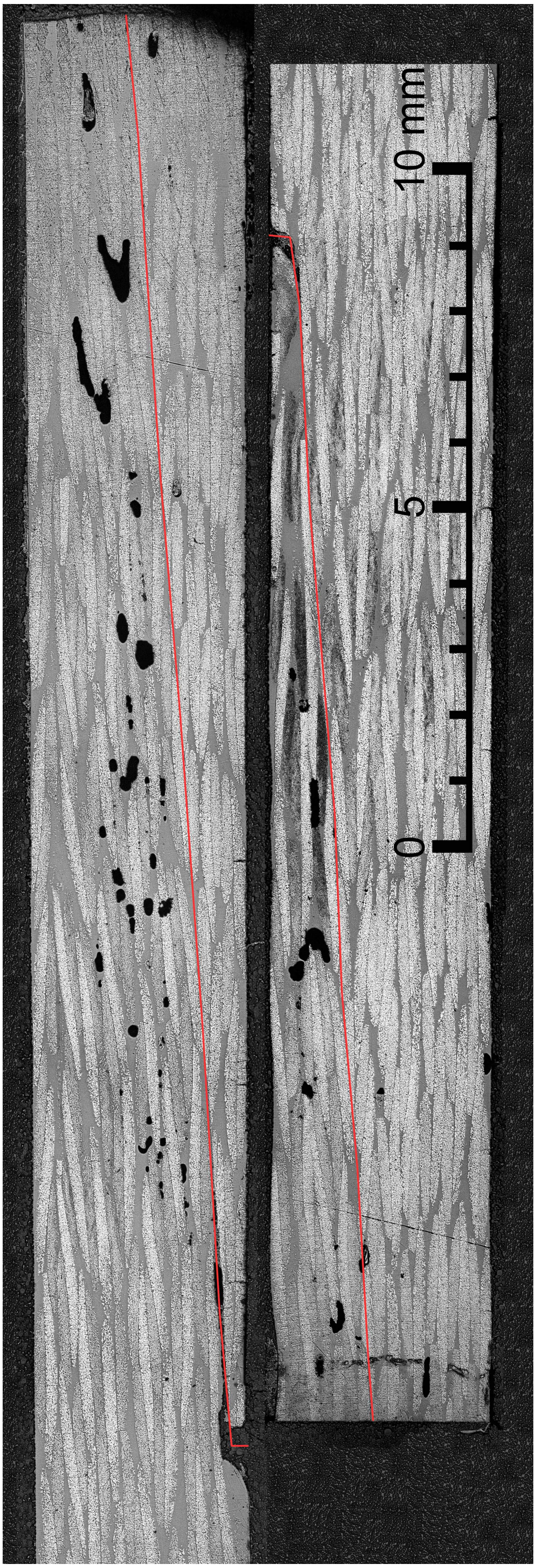

Figure G.8: Micrography of the CTI-M1 sample, interface indicated by the red line

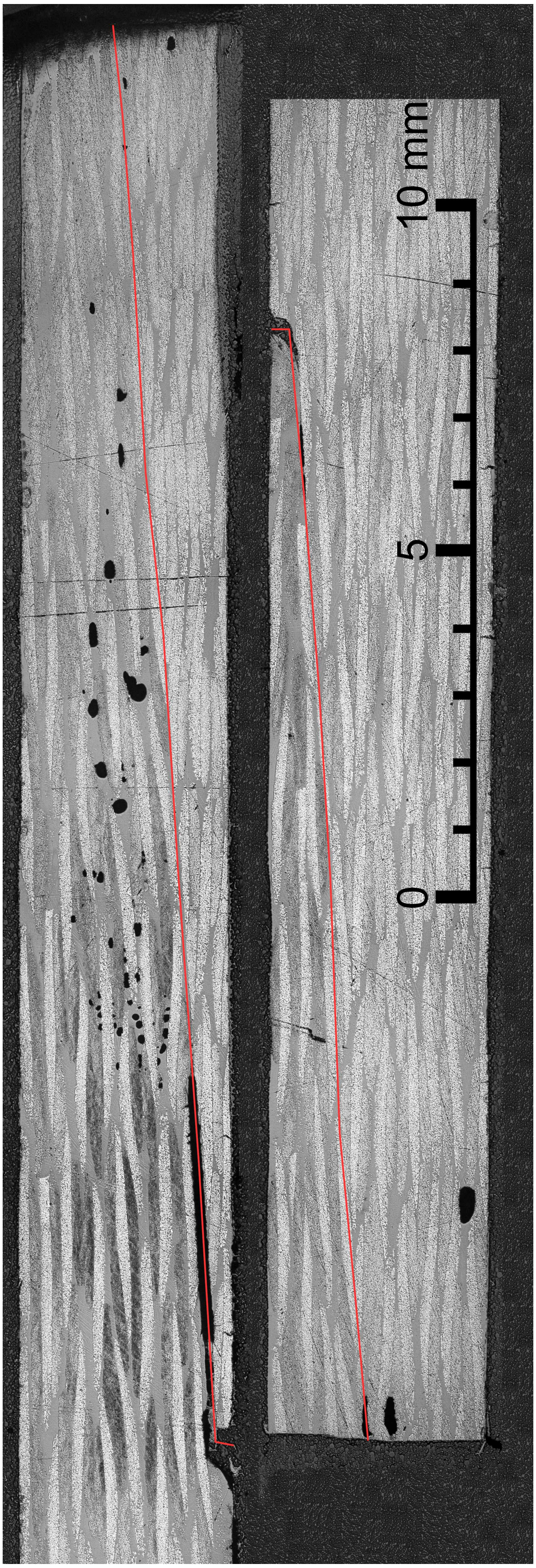

Figure G.9: Micrography of the CTI-M2 sample, interface indicated by the red line

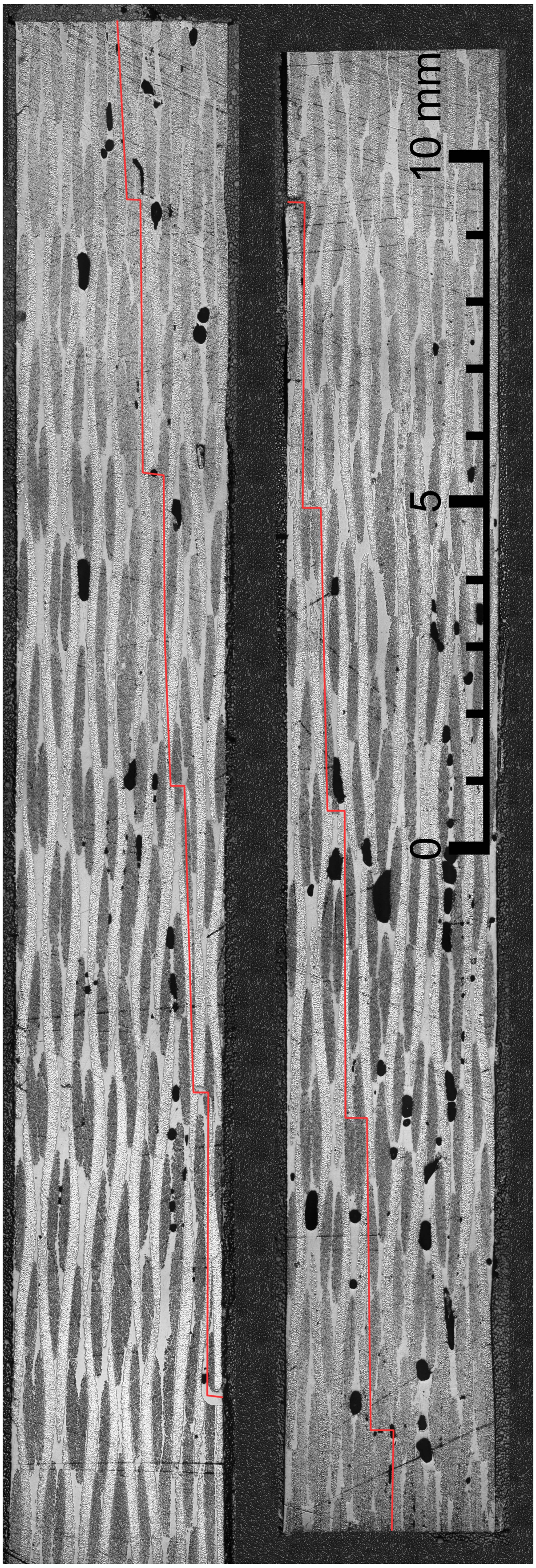

Figure G.10: Micrography of the STI-M1 sample, interface indicated by the red line

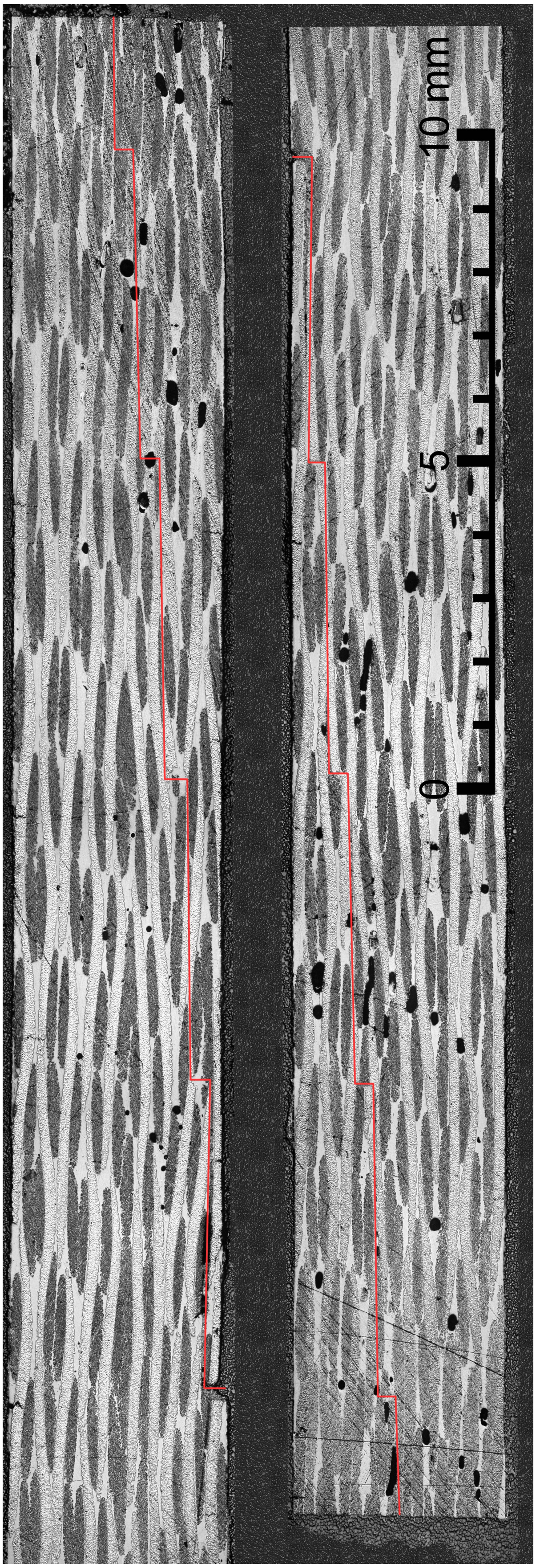

Figure G.11: Micrography of the STI-M2 sample, interface indicated by the red line

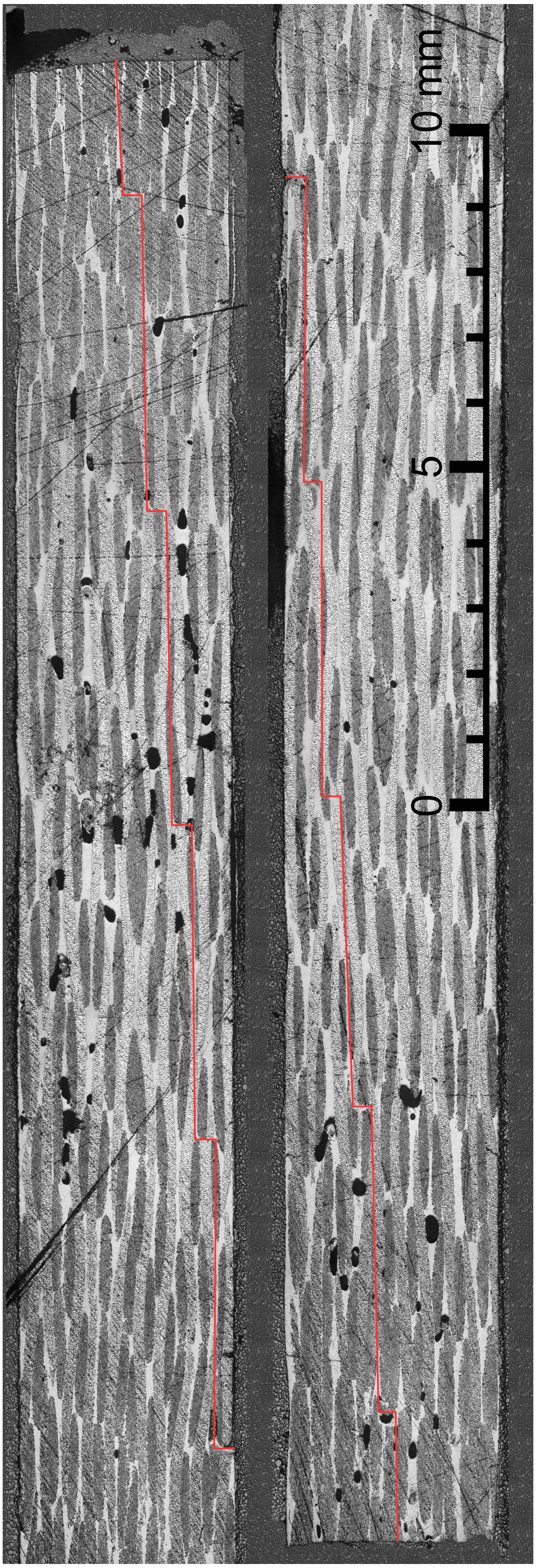

Figure G.12: Micrography of the STI-M3 sample, interface indicated by the red line

# H

# Extensometer Values

The stiffness measured by the extensometer for the welded samples is significantly lower than the pristine stiffness, as can be seen in Table H.1. This is lower than expected and does not agree with FEM which shows a near pristine stiffness. To verify the extensometer readings the stiffness is calculated using the DIC measurements. At 10% and 80% of the failure load the strain is determined by taking the average deflection of two areas on the opposite side of the scarf joint. These two areas are indicated in Figure H.1. As DIC is not performed on the pristine samples a DIC stiffness cannot be obtained for these samples.

Instead of verifying the low stiffnesses measured by the extensometer, the DIC measurements result in an average welded samples stiffness of 53.2 $GPa$. As the FEM and the DIC measurements agree, one could conclude that the extensometer readings are faulty. However, the pristine samples, tested at the same setup, day, and same settings have extensometer readings that deviate less than 1% from the theoretical measurements.

As final check the displacement from the clamps of the tensile testing bank are extracted. These displacements are not calibrated and cannot be used for absolute values. They can be used to compare the relative stiffness between the pristine and welded samples. As can be seen in Table H.1, the clamp displacement indicates that the stiffness of the welded samples should be about 95% of the pristine samples.

The average stiffness of the DIC measurements is 96% of the average pristine extensometer stiffness. Therefore, it is concluded that the extensometer readings for the welded samples are faulty. Consequently, the DIC stiffness will be used for the welded samples and the extensometer stiffness are used for the pristine samples.

Table H.1: Average stiffness of the samples

| | Extensometer | | DIC measurements | | Clamp displacement | | |
|---|---|---|---|---|---|---|---|
| | Welded | Pristine | Welded | Pristine | Welded | Pristine | |
| $E_{avg}$ | 26.7 | 55.5 | 53.2 | - | 33.8 | 35.4 | $[GPa]$ |
| $COV$ | 1.03 | 1.12 | 2.42 | - | 1.31 | 1.24 | [%] |

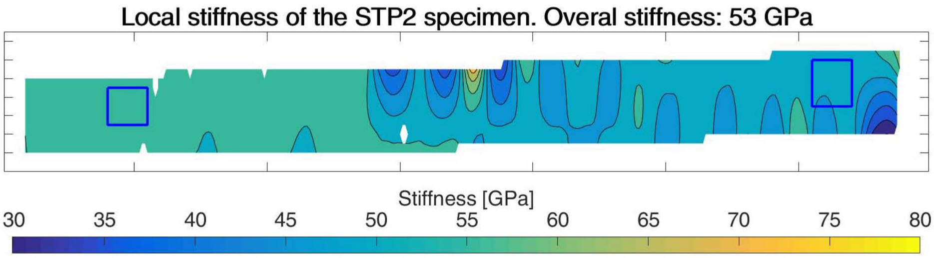

Figure H.1: Local stiffness of the STP-T2 sample at 80% of the failure load

# I

# Tensile Testing of the Pristine Specimen

The results of the tensile test are shown in Table I.1, the failure modes in the last column are given in Figure I.2.The stiffnesses are calculated using the stresses at 0.2% and 0.5% strain. The average values, standard deviation and coefficient of variation (COV) are given in Table I.2. It can be seen that the stiffness is very consistent, having a COV of only 3.3%, whereas the maximum force, stress and strain have a COV of about 12.4-13.3%. It should be noted that three out of four samples fail at the grip suggesting tabs or lower gripping pressure is needed to tensile test these samples, it is expected that the COV of the normalized stress and strain will decrease significantly if tabs are used during tensile testing.

A t-test is used to determine whether the given material strength and stiffness could be within the measured interval. Both the stiffness and maximum strength pass the test with a probability of about 23%. Due to the large number of grip failures and two deviating failure stresses the pristine $\sigma_{max}$ of 757 $MPa$ as stated in the material data sheet is used as reference for the relative joint strength.

Table I.1: Dimensions of the pristine samples

| ID | $w_0$ | $t_0$ | $F_{max}$ | $\frac{t}{t_{ref}}$ | $\sigma_{max\,norm}$ | $\varepsilon_{F_{max}}$ | $E_{norm\,zwick}$ | Failure |
|---|---|---|---|---|---|---|---|---|
| | $[mm]$ | $[mm]$ | $[N]$ | $[-]$ | $[MPa]$ | $[-]$ | $[GPa]$ | |
| $PR-T1$ | 25,46 | 3,11 | 49609 | 1 | 627 | 0.0115 | 52.93 | LAB |
| $PR-T2$ | 25,44 | 3,10 | 62328 | 1 | 788 | 0.0144 | 54.57 | LAB |
| $PR-T3$ | 25,48 | 3,11 | 58718 | 1 | 742 | 0.0136 | 56.84 | XGM |
| $PR-T4$ | 25,46 | 3,11 | 48482 | 1 | 613 | 0.0109 | 56.41 | LAB |

Table I.2: Weibull distribution for the pristine samples

| | $t_0$ | $F_{max}$ | $\sigma_{max\,norm}$ | $\varepsilon_{F_{max}}$ | $E_{norm\,zwick}$ |
|---|---|---|---|---|---|
| | $[mm]$ | $[N]$ | $[MPa]$ | $[-]$ | $[GPa]$ |
| $\bar{x}_{PR}$ | 3.11 | 54784 | 692.5 | 0.0126 | 55.19 |
| $s_{PR}$ | 0.01 | 680 | 86 | 0.0017 | 1.80 |
| $COV_{PR}$ | 0.16% | 12.42% | 12.42% | 13.34% | 3.26% |

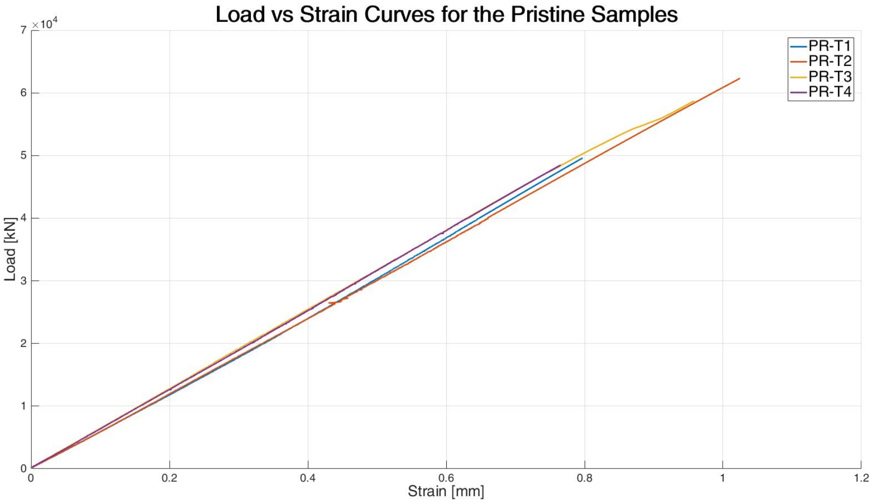

Figure I.1: Load vs strain curves for the pristine tensile tested samples

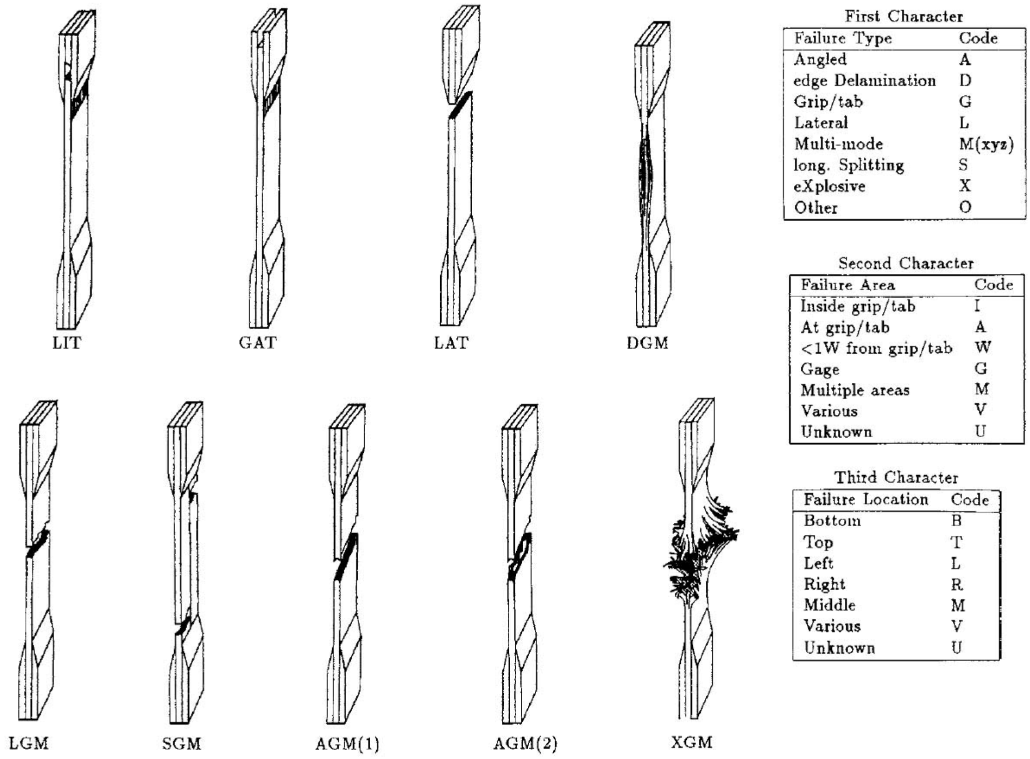

First Character

| Failure Type | Code |
|---|---|
| Angled | A |
| edge Delamination | D |
| Grip/tab | G |
| Lateral | L |
| Multi-mode | M(xyz) |
| long. Splitting | S |
| eXplosive | X |
| Other | O |

Second Character

| Failure Area | Code |
|---|---|
| Inside grip/tab | I |
| At grip/tab | A |
| <1W from grip/tab | W |
| Gage | G |
| Multiple areas | M |
| Various | V |
| Unknown | U |

Third Character

| Failure Location | Code |
|---|---|
| Bottom | B |
| Top | T |
| Left | L |
| Right | R |
| Middle | M |
| Various | V |
| Unknown | U |

Figure I.2: Failure mode identification as given in the ASTM D3039 regulations [6]